DAMAGE EVOLUTION IN AA2099 AND AA6061 ALUMINUM ALLOYS UNDER QUASI-STATIC AND DYNAMIC MECHANICAL LOADING

A Thesis Submitted to the College of

Graduate Studies and Research

In Partial Fulfillment of the Requirements

For the Degree of Master of Science

In the Department of Mechanical Engineering

University of Saskatchewan

Saskatoon

By

ADEROPO OMORINU ADESOLA

© Copyright Aderopo Omorinu Adesola, September, 2011. All rights reserved.

PERMISSION TO USE

In presenting this thesis in partial fulfillment of the requirements for a Postgraduate degree from the University of Saskatchewan, I agree that the Libraries of this University may make it freely available for inspection. I further agree that permission for copying of this thesis in any manner, in whole or in part, for scholarly purposes may be granted by the professor who supervised my thesis work, Prof. Akindele Odeshi, or, in his absence, by the Head of the Department or the Dean of the College in which my thesis work was done. It is understood that any copying or publication or use of this thesis or parts thereof for financial gain shall not be allowed without my written permission. It is also understood that due recognition shall be given to me and to the University of Saskatchewan in any scholarly use which may be made of any material in my thesis.

Requests for permission to copy or to make other uses of materials in this thesis in whole or part should be addressed to:

Head of the Department of Mechanical Engineering

University of Saskatchewan

Saskatoon, Saskatchewan S7N 5A9

Canada.

ABSTRACT

In this research, the behavior of AA2099 and AA6061 aluminum alloys under quasi-static and dynamic mechanical loading conditions was examined. The effects of temper condition on the dynamic response of both alloys were investigated as well as the microstructural evolution associated with the formation of adiabatic shear bands in these alloys. Cylindrical specimens of the alloys were solutionized at 540 ºC for 2 h, water quenched, cold worked (T8) and then followed by natural aging, one-step artificial aging or two-step artificial aging to produce different temper conditions. Quasi-static compression, microhardness, direct impact and dynamic torsion tests were thereafter conducted on the aged specimens.

Microhardness and quasi-static compression test results showed that strain hardening prior to precipitation hardening increased deformation resistance in AA2099 alloy, but it made no difference in the deformation resistance of precipitation-hardened AA6061 alloy. The two-step aged AA2099 alloy showed higher deformation resistance compared to the one-step aged or naturally aged alloy. Although AA2099 alloy showed superior mechanical properties under quasi-static loading, the reverse was observed under dynamic mechanical loading at high strain rates. Both direct impact and dynamic torsion test results showed that AA2099 and AA6061 failed by adiabatic shear band formation at high strain rates. Under dynamic shock loading conditions, strain hardening prior to precipitation hardening reduced the deformation resistance of AA2099 alloy but increased that of AA6061. The higher strength of the naturally aged AA2099 compared to the one-step aged alloy and the higher strength observed in one-step aged than in the two-step aged alloy indicated that precipitation of second phase particles promoted adiabatic shear banding in AA2099 alloy.

The results of optical and scanning electron microscopy showed that depending on the temper condition and strain rates, both deformed and transformed shear bands formed in

the two alloys under dynamic shock loading. While dissolution of second-phase particles occurred inside the shear bands formed in AA2099, very fine equi-axed grains of average size of 620 nm were observed inside the transformed bands of AA6061 alloy. Intense localized thermal softening led to the dissolution of the reinforcing second-phase particles, causing reduction in the deformation resistance and promoting shear strain localization in AA2099 alloy. Investigation of the transformed band in AA6061-T6 alloy using synchrotron light radiation at the Canadian Light Source showed the presence of less silicon inside the transformed band than in the region adjacent to the shear band.

ACKNOWLEDGMENTS

I would like to express my heartfelt gratitude and thanks to my advisor, Professor Akindele Odeshi for giving me the opportunity to pursue my graduate studies under his supervision. I am grateful to Professor Odeshi for enriching me with the knowledge of materials science and engineering through his teaching during my graduate days. This thesis is made possible through his valuable guidance, support and understanding over the experimental, moral and theoretical challenges that came my way during the program. I would like to thank my advisory committee members, Professor Ikechukwuka Oguocha and Professor Chris Zhang for their time, support and valuable advice in the course of my graduate studies. My appreciation and gratitude go to the college of graduate studies and research and the department of mechanical engineering for student funding and research enabling environment. My appreciation also go to Prof. Bassim for permission to use his high strain rate equipment, Mrs. Kelley Neale for her words of encouragement, assistance and counsels, Mr. Rob Peace, Mr. Hans and Mr. J. P. Burak for their time, support and technical expertise in conducting the research experiments.

This journey to acquire knowledge and education has been a possibility through the help of God and the supports of my late father, Mr. Ayinde Adesola, my mother, Mrs. Olujoke Adesola, my fiancee, Ijeoma Maduchor, and friends, Tolulope Sajobi, Abimbola Sajobi, Bolaji Adeniji and Adeteju Bababunmi. Their constant motivation, love and encouragement gave me the strength and enthusiasm to complete this research. I could not have achieved this feat without their unconditional love and support.

DEDICATION

This thesis is dedicated to

The Ancient of Days

for

the courage, strength, wisdom and power to complete this thesis

and

My suitable helper, Ijeoma Favour Maduchor...

Truly, he that finds a wife finds a good thing and obtains favor from the Lord...

TABLE OF CONTENTS

LIST OF TABLES

LIST OF FIGURES

ABBREVIATIONS

AA	Aluminum association.
ASBs	Adiabatic shear band.
OM	Optical Microscopy.
SEM	Scanning Electron Microscopy.
AISI	American Iron and Steel Institute.
γ_{LOC}	Strain within the shear band.
w	Width of the shear band.
T	Temperature reached inside the shear band.
T_0	Room temperature.
C_v	Heat capacity.
Wp	Specific work of deformation.
σ	Applied stress.
ε	Applied strain.
SFE	Stacking fault energy.
SIBM	Strain Induced Grain Boundary Migration.
LAGBs	Low angle grain boundaries.
HAGBs	High angle grain boundaries.
ALCOA	Aluminum Company of America.
F	Load.
HV	Vickers hardness.
GP Zones	Guinier-Preston zones
GPB Zones	Guinier-Preston-Bagaryatsky zones.
σ_t	True stress.
ε_t	True strain.
L_i	initial length.

L_f	final length.
L_b	Length of striking projectile.
C_b	Longitudinal wave velocity of transmitting bar.
E	Elastic modulus.
ρ	Density.
γ_I	Incident wave signal.
γ_R	Reflected wave signal.
γ_T	Transmitted wave signal.
r_s	Mean radius of the thin-walled specimen.
r_b	Radius of the input bar in torsion split Hopkinson bar equipment.
L_s	Gauge length of the torsion specimen.
τ_s	Shear stress
T_s	Applied torque in the specimen.
t_s	Wall thickness of the torsion specimen.
G	Shear modulus of the material.
θ	Angle of twist in rad.
D_b	Diameter of the input bar in torsion split Hopkinson bar equipment.
La	Length of the loaded arm of the shaft in torsion split Hopkinson bar equipment.

1. INTRODUCTION

1.1 Overview

AA2099 is a commercial aluminum-lithium alloy belonging to the Al-Li-Mg-Cu-Zr alloy system. It is used extensively for aerospace applications owing to its low density, high specific modulus, and excellent fatigue, cryogenic and toughness properties. It also exhibits other desirable properties such as superior machinability, formability and surface finish. As a result of its excellent mechanical properties, AA2099 aluminum alloy can find very useful applications such as in statically and dynamically loaded fuselage structures, lower wing stringers, and stiffness dominated designs [1]. The high specific strength of AA2099 aluminum alloy makes it the preferred material over other alloys in the AA 2000, 6000, and 7000 series for high performance aerospace applications. Lithium as an alloying element significantly alters the mechanical properties and density of traditional aluminum alloys developed for the same purpose. The introduction of 1% lithium to aluminum decreases the specific weight of aluminum alloys by 3% and simultaneously raises the modulus of elasticity by 6% compared to other aluminum alloys [2,3]. Similarly, AA6061 aluminum alloy is a multipurpose Al-Mg-Si-Cu alloy and is the most widely used in the AA6000 series of aluminum alloys. Due to its medium to high strength, good fracture toughness and excellent corrosion resistance, it finds useful applications in automotive parts such as wheels and panels [4-8].

1.2 Motivation

The AA2099 aluminum alloy has been adequately studied under quasi-static loading conditions. Since component made from AA2099 can also be exposed to dynamic impact loading in service, it is important to understand the damage evolution in this alloy under dynamic mechanical loading at high strain rates. A typical example of impact damage is the case of bird strikes on wing and fuselage structures of aircraft. An example of birds capable of causing serious damage to aircraft is the Canadian goose which weighs up to 10 kg. Although few human deaths have been associated with bird strikes, there has however been considerable economic cost in terms of aircraft downtime per year. These wing and fuselage structures of aircraft can suffer huge damage during the collision with a bird during take-off or landing. Another example of impact damage is the massive damage to overhead panels, wheels and aluminum alloy engine blocks in automobiles during collision. There has been some previous work on dynamic impact response of Aluminum 6061-T6 alloy. However, the effects of temper condition on damage evolution in the alloy have not been fully investigated.

Materials deformation and failure behaviour under massive and rapid loading conditions typical of high strain rate is different from deformation under quasi-static loading. For example, during massive deformation of a metal under impact loading by a projectile, nearly 90% of the kinetic energy of the projectile is converted to heat [9]. This heat is retained along some paths, causing localized adiabatic heating along these paths. At such high strain rates, which can be in excess of 10^3 s^{-1}, shear strain localization characterizes the plastic deformation process. Deformation then becomes localized along narrow paths known as adiabatic shear bands (ASBs). These bands act as precursors to catastrophic failure of materials at high strain rates by promoting initiation of cracks and providing crack propagation paths. Due to the risk associated with impact damage, there is the need to study the damage response of both AA2099 and AA6061 aluminum alloys when subjected to dynamic mechanical loading.

1.3 Research Objectives

The main objectives of this research were:

1. To investigate the mechanical behaviour of AA2099 and AA6061 alloys under quasi-static and high strain-rate loading.
2. To investigate the effects of temper conditions on shear strain localization and the occurrence of adiabatic shear bands in the alloys at high strain rates.
3. To investigate the microstructural evolution associated with the formation of adiabatic shear bands as influenced by temper conditions.

1.4 Methodology

To achieve the stated research objectives, cylindrical samples machined from as-received samples of AA2099-T8 and AA6061-T6 aluminum alloys were subjected to various heat treatment processes to create different temper conditions. The temper conditions developed in AA2099 were T4, T61, T62, T81 and T82. The '1' in T61 and T81 tempers indicates the temper condition realized through one-step artificial aging process. The '2' in T62 and T82 tempers indicate the temper condition realized through two-step artificial aging process. The study of age hardening in aluminum-lithium alloys showed that better mechanical properties were achieved when a two-step aging process was used [10,11]. The temper conditions developed in AA6061 were T4 and T8. The as-received temper condition for AA2099 is T8 while the as-received temper condition for AA6061 alloys is T6. Both AA2099 and AA6061 alloy specimens in these temper conditions were then subjected to microhardness test, quasi-static compression test, direct impact test and dynamic torsion test. The microstructures of the alloys before and after impact were investigated using optical microscopy (OM) and scanning electron microscopy (SEM).

1.5 Thesis Arrangement

Chapter two of this thesis contains a brief literature review on deformation of materials, the causes of strain localization in engineering materials and the failure of materials due to adiabatic shear band formation. Chapter three discusses the materials, equipment and experimental methods. Chapter four presents and discusses the results from the mechanical test and the microstructural evaluations conducted in chapter three. In chapter five, the conclusions drawn from the analysis of obtained results and recommendations for future work are outlined.

2. LITERATURE REVIEW

This chapter provides a brief summary of deformation of engineering materials at low and high strain rates, the formation and types of adiabatic shear bands, the occurrence of adiabatic shear bands in aluminum alloys, steels and other non-ferrous materials. Factors affecting shear band formation, mechanisms leading to adiabatic shear band formation as well as adiabatic shear failure will also be briefly reviewed.

2.1 Deformation of Materials

Ductile materials under mechanical loading conditions undergo elastic and permanent (plastic) deformation before failure. During elastic deformation, deformation is uniform and recoverable when the load is removed. When the elastic limit is exceeded, the deformation becomes permanent (plastic) and it is not recoverable when the load is removed. In the first stage of plastic deformation, the metal strain hardens due to dislocation interactions until a point of maximum stress is reached. The second stage of plastic deformation however depends on the type of applied mechanical load, which may be fatigue, creep, impact, quasi-static tensile or compressive loading. Plastic deformation under quasi-static loading (strain rates ranging between 10^{-5} to 10^{-1}/s) occurs by slip and twinning mechanisms and failure are usually preceded by necking (for tensile loading) and buckling (for compression loading). Mechanisms of plastic deformation at elevated temperature (creep) include diffusion creep, dislocation creep, dislocation glide and grain boundary sliding depending on the exposure temperature and applied stress. Cyclic softening or cyclic hardening leading to formation of dislocation cell structures are known to be associated with fatigue loading. This study focuses on plastic deformation under dynamic shock loading such as ballistic impact, which is a very complex phenomenon that is dependent on several materials and loading variables.

Deformation and failure of metallic alloys under dynamic shock loading (high strain rates) will be the focus of this literature review.

2.2 Deformation at High Strain Rates

Deformation of metals under dynamic shock loading usually occurs at strain rates above 10^3/s and are known to be characterized by shear strain localizations. An example of this is massive deformation of a material impacted by a high velocity projectile. In this case, only about 10% of the striking projectile's kinetic energy is used in deforming the material while the rest is converted into thermal energy [9]. Because this thermal energy is not conducted away along some narrow regions, localized adiabatic heating can occur in these narrow regions thereby creating thermo-mechanical instability which cause shear strain localization. This was first identified by Zener and Hollomon as the primary cause of shear strain localization [12]. This shear strain localization occurs when strength loss from work softening along these bands becomes greater than the strength increase due to work hardening [13]. During work softening, dislocations realign and annihilate each other thereby allowing a continuous deformation of the material [14]. The microstructural changes involved in work softening can either be dynamic recovery or dynamic recrystallization. Intensive localized thermal softening causes stress collapse and shear strain localization along narrow paths. These paths of extreme shear strain localization are known as adiabatic shear bands (ASBs).

Deformed bands and transformed bands are the two known types of adiabatic shear bands. Deformed bands are commonly observed in non-ferrous alloys such as copper, titanium and aluminum alloys [15-17] and contain distorted grains while transformed bands are common in hardened steels [18-21] and they contain very fine equi-axed grains. The transformed bands are also called white etching bands due to their white appearance when viewed under an optical microscope. Apart from steels, transformed bands have also been observed in some aluminum alloys such as weldalite, 7075, and 8090 [22-24]. Adiabatic shear bands are however not only observed in metals but in also in polymers [25], ceramics [26] and composites [27-29]. These adiabatic shear bands act as precursors to catastrophic failure of materials at high strain rates by promoting

initiation of cracks and providing crack propagation paths. The failure that is preceded and caused by the occurrence of adiabatic shear band is termed adiabatic shear failure. Microstructure of adiabatic shear bands range from highly elongated grains in deformed bands, to equi-axed subgrains possessing a high degree of misorientation or very fine recrystallized grains in transformed bands [30]. Several mechanisms such as phase transformation, dynamic recrystallization, grain elongation and fragmentation, dislocation re-distribution and patterning have been suggested to explain the ultra-fine grain structure of transformed bands [31-34].

2.3 Adiabatic Shear Bands in Aluminum Alloys

Several aluminum alloys have been observed to experience adiabatic shear failure at high strain rates with both deformed and white etching bands reported in these alloys [15,17,22-24]. High purity aluminum alloy when cold rolled clearly shows an adiabatic shear band consisting of parallel streaks which appear transverse and wavy along the rolling direction [35]. The same wavy structure is observed in the shear band of high purity aluminum-lithium alloy such as 1460T [36]. The shear band formed in 2090 aluminum alloy is observed to contain heavily elongated grains and forming coarse particles along grain boundaries [15,37]. In 2024 aluminum alloy, low rolling strain generates shear bands confined within grains and high rolling strain generates shear band traversing more than one grain were observed [38]. Transformed band in weldalite has been observed to contain very fine equi-axed grains with average grain size of 0.2 μm. [22,37]. In AA3004 aluminum alloy, shear band are observed to contain elongated cells in the shear direction [39]. A study on shear band formation in AA5182 and AA5754 both reveal heavily distorted grain structure [40-44]. Heavily distorted grains structure are also observed in the shear band formed in AA6061 aluminum alloy [17,27,45]. In AA7039 aluminum alloy, a heavily deformed matrix reveals the presence of shear band containing highly elongated grain structure [46]. In AA7075 aluminum alloy, shear bands are observed to contain highly distorted and fine equi-axed grains [23,47]. In AA8090 aluminum alloy, very fine equi-axed grains have been observed in the microstructure of the transformed shear bands [24].

When alumina particles are added to reinforce AA6061-T6 aluminum alloy [27], the reinforcing alumina particles tend to be closely packed inside the observed shear band. The deformation only occurred within the aluminum matrix, leaving the alumina particle unfragmented. When TiB_2 is added to reinforce aluminum [28], a special type of shear band observed as melted aluminum band was observed. This melted aluminum band is seen to be much narrower than a typical deformed band. This melted aluminum matrix is observed to surround the reinforcing TiB_2 particles. In AA2124 alloy reinforced with SiC_w whiskers [48], shear band was observed at whisker content of about 7%. The whisker tends to align with the direction of deformation. Increasing the whisker content to about 20% reduces the tendency of adiabatic shear band formation. Love *et al.* [49] observed adiabatic shear band formation in particle reinforced aluminum matrix composites and reported that its propagation is not affected by debonding between the matrix and particles. In general, it can be concluded that deformed bands in aluminum alloys contain heavily distorted grain structure while transformed bands contains very fine equi-axed grain structure. As a result of these very fine equi-axed grains, adiabatic shear bands tend to possess higher hardness compared to the surrounding matrix. They act as the precursor for failure at high strain rates.

2.4 Adiabatic Shear Bands in Other Materials

Non-ferrous alloys other than aluminum alloys have also shown the occurrence of adiabatic shear failure at high strain rates. Deformed band containing grains with high degree of reorientation was reported in pure copper [16]. In Ti-3Al-5Mo-4.5V titanium alloy [50], transformed band was observed and it contained refined and elongated grains along the shear direction. Shear bands formed in Ta-10 W tantalum alloy [51] were reported to contain highly elongated dislocation cells along the direction of shear stress. In polymers such as polyurethane foam [25], polycarbonate and polymethylmethacrylate [14], localized adiabatic heating associated with shear ductile failure occurred thereby leading to adiabatic shear failure.

In steels, both deformed and transformed bands have been observed in numerous studies. Deformed bands usually appear as distorted grain while transformed bands

usually appear as fine equi-axed structure. A study by Meyers *et al.* [52] on low carbon steels showed the formation of deformed bands in AISI 1018 steel and transformed bands in AISI 8620 steel. The structure of the deformed band in AISI 1018 steel appears lamellae. The darker region of the deformed band contains highly deformed pearlite and the lighter regions deformed ferrite. The transformed band observed in AISI 8620 is reported common to martensitic and bainitic steels. The shear band nucleates in regions where martensitic lamellae align themselves along the flow direction. A study on JIS SS400 steel reveal a shear band containing highly elongated narrow subgrains extending along the shear direction [53]. Investigation of the transformed band in armoured steel by Derep [54] reveals the presence of ferrites, iron carbides and martensites with sizes below 300 nm inside the transformed band. The study of transformed band by Sunwoo *et al.* [55] reveal diffuse shear band formation in both as-received and heat treated AerMet-100 alloy. The transformed band in the hard as-received sample originally containing martensitic structure with randomly spherical inclusions reveal a shear band with a width of 1 μm. The soft heat treated sample containing martensite and carbides reveal a diffuse shear band with width ranging from 1.5 – 5 μm. No phase transformation was reported in this alloy. Such types of diffuse shear bands have also been observed in soft and hard AISI 4340 steel [56]. Report by Roessig *et al.* [17] on adiabatic shear localization in 1018 steel reveal deformed band with a width of 200 μm. A similar width of deformed band was mentioned by Giovaniola *et al.* [57]. Marchand and Duffy [58] deduced a relationship between the width of the shear band (w) and the strain within the shear band γ_{LOC} in HY 100 steel as follows:

$$\gamma_{LOC} = aw^{b} \quad \text{.....(2.0)}$$

where a and b are constants. In HY-100 steel, *a* is 125.8 and *b* is -0.867.

2.5 Factors Affecting Adiabatic Shear Band Formation

The temperature reached inside a shear band during impact loading is estimated using the equation below [31].

$$T = T_0 + 0.9 \, {W_p}/{\rho C_v} \quad \text{.....(2.1)}$$

Where T_o is the room temperature, C_v is heat capacity and W_p is specific work of deformation [31] and is given by the area under the stress-strain curve. Thus,

$$W_p = \int \sigma . d\varepsilon \quad \text{.....(2.2)}$$

From equation 2.2, increase in both applied stress and strain rate increases the specific work of deformation. An increase in specific work of deformation leads to an increase in temperature and hence the tendency for adiabatic shear band formation. It has been observed that there exists a critical strain and strain rate value for adiabatic shear band to occur [24,31]. From Equation 2.1, increase in density and heat capacity also reduces the tendency for adiabatic shear band formation. Other factors affecting shear band formation are conductivity, geometry, surface friction, microstructure, defects, strain hardening coefficient, confining hydrostatic pressure, strength level [59].

In geometrical imperfections such as notch, high temperatures that are likely to develop around the notch and accelerate the formation of adiabatic shear band [59]. These shear bands are observed to initiate first at the notch tip [60-62] after which crack initiates at the shear band initiation site and then propagates along the shear band to failure. The elastic energy generated at the tip of the shear band as a result of stress collapse contributes to the crack propagation process [62]. Zhou *et al.* [61] reported the failure mode transition from ductile shear banding to brittle cracking at an intermediate impact velocity of 45 m s^{-1} in C-300 steel. When the velocity increased above 45 m s^{-1}, the C-300 steel experienced ductile shear failure but when it was below 45 m s^{-1}, brittle failure occurred. Li *et al.* [63] studied the influence of specimen geometry on the sensitivity of shear localization. He investigated three models of truncated-conic specimens with different ratios of the height to the diameter upon impact. In model 1 with 10 mm height, 5 mm upper cone diameter and 7 mm lower cone diameter, deformation was localized at the top right corner of the cone but no adiabatic shear band

was observed. In model 2 with 4 mm height, 8 mm upper cone diameter and 10 mm lower cone diameter, shear band was observed. In model 3 with 2 mm height, 8 mm upper cone diameter and 10 mm lower cone diameter, shear band was observed. This means reducing height and increasing diameter of the cone increases the tendency to form adiabatic shear band. Increasing the coefficient of friction between the upper surface of the specimen and the impacting surface from 0.02 to 0.10, a distinct shear band appears at the right hand corner in model 1 while the shear band in model 3 disappears. This change in friction coefficient however does not affect model 2. To determine the tendency of brittle materials to form adiabatic shear bands, the material must be enclosed in a ring to prevent early failure. The hydrostatic pressure generated when a cylindrical brittle sample is enclosed in a ring before impact has been observed to postpone the onset of adiabatic shear band formation thereby delaying its propagation and slowing down the failure mechanism [59]. The effect of impurity or reinforcement in alloys has already been discussed earlier.

2.6 Adiabatic Shear Band Initiation Mechanisms

The possible shear band initiation mechanisms (Fig 2.1) observed in single phase homogeneous materials [42,64] are (a) grain size inhomogeneity, (b) geometrical softening, (c) Peirce-Asaro-Needleman textural localization [65,66] and/or (d) dislocation pile up release [67]. Due to varying distribution of grain sizes in an alloy, a low yield stress (σ_1) is generated in a large sized grains compared to a smaller sized grains (σ_2). Such grains with large sizes tend to deform preferentially and then possibly act as an initiation site for adiabatic shear band [42,64] (Fig 2.1a). Geometrical softening [64] can occur as a result of grain rotation leading to localised softening and initiation of shear bands (Fig 2.1b). When the schmid factor increases in a grain with plastic deformation, localised deformation of the grain can result in extended strain-localised band through cooperative plastic deformation of grains (Fig 2.1c). This was earlier reported by Pierce *et al.* [65]. When dislocation pile-up suddenly forcefully cuts through a grain boundary, an increase in temperature as well as plastic deformation can occur. The softening effect of the temperature rise and the plastic deformation can help initiate shear bands (Fig 2.1d).

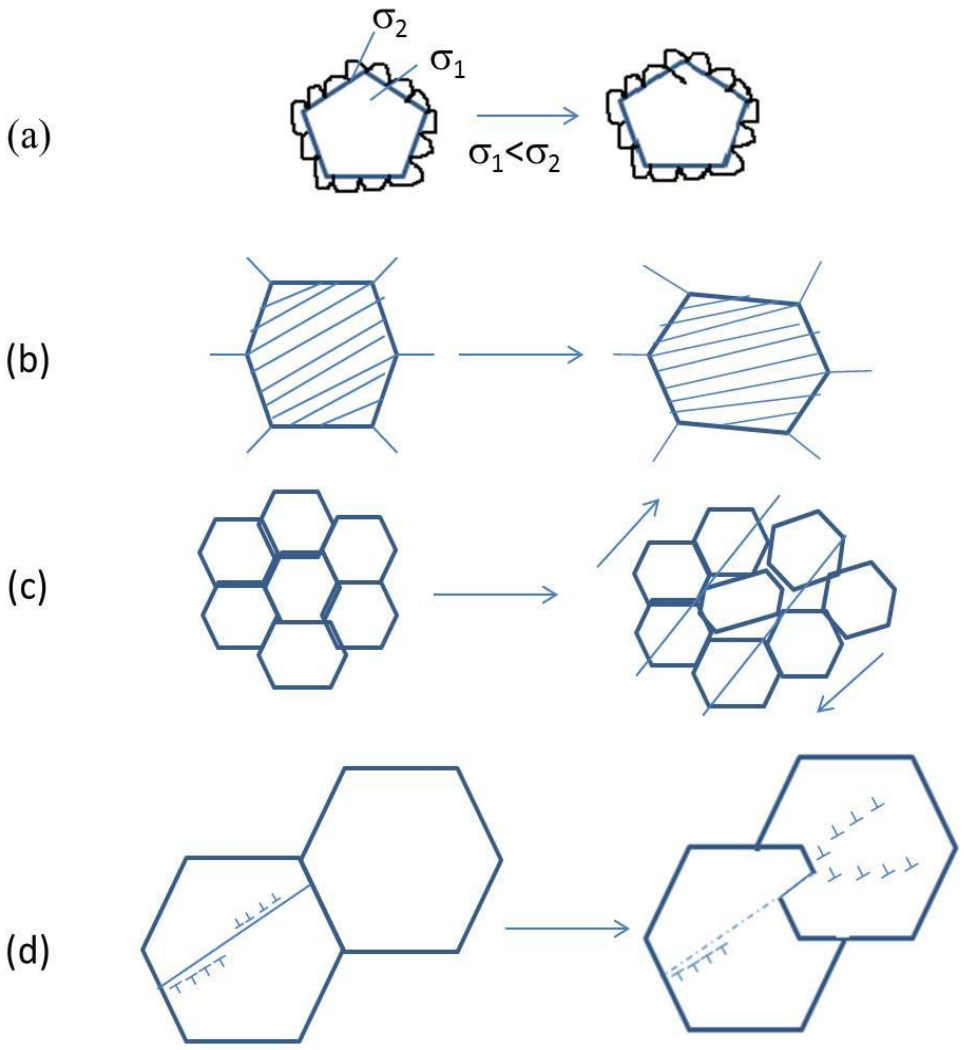

Figure 2.1. Possible shear band initiation mechanisms in single-phase homogeneous materials. (a) grain-size inhomogeneity, (b) geometrical softening, (c) Peirce-Asaro-Needleman textural localization and (d) dislocation pile-up release [adapted from references 42 and 64].

2.7 Mechanisms of Adiabatic Shear Band Formation

Several theories have been suggested to explain the mechanism of formation and propagation of adiabatic shear bands in structural materials. These include; phase transformation, dynamic recrystallization, grain elongation and fragmentation, dislocation re-distribution and patterning [31-34].

2.7.1 Phase Transformation

It has been suggested that temperature rise that may cause austenitic transformation can occur inside transformed bands in steels. The austenite formed inside the shear band is proposed to be rapidly quenched by the materials adjacent to the shear band forming untempered martensite [31,68-70]. The white colour of the transformed band in steel has been attributed to this phase transformation. Such phase transformation is not observed in deformed band. Some researchers [18,71,72] have apparently disagreed with the suggested austenite-to-martensite transformation taking place during the formation of white etching ASBs observed in steels. Lesuer *et al*. [18] observed the presence of pearlite, ferrite and cementite in transformed band formed in ultra-high carbon steel containing 1.3% carbon. This observation is contrary to the already proposed austenite-to-martensite transformation. A maximum temperature of about 600ºC was observed when measuring the temperature distribution inside the transformed bands of HY-100 steel [71] and AISI 4340 steel [72]. Since this temperature is less than the austenitizing temperature in both HY-100 steel (922 ºC) and AISI 4340 steel (830 ºC), the transformation to austenite phase can be questioned. Without this transformation, no martensite can be formed. Baofa *et al*. [13] reported that during shear band formation, a large austenite may remain in the bulk matrix but none is present inside the shear band. This has however been proven wrong in some studies. The presence of untransformed austenite was observed in some adiabatic shear band by Chou *et al*. [73], which was reported to be a consequence of a reverse martensitic transformation reaction during localized adiabatic heating [70,73].

As discussed earlier that adiabatic shear bands provide crack initiation sites and crack propagation path, steel with already formed adiabatic shear bands will fail catastrophically upon subsequent loading. Post-impact heat treatment such as annealing of 4340 steel by Odeshi *et al*. [19] was observed to reverse the microstructural changes which occurred inside adiabatic shear bands. The white etching bands changed and appeared similar to the bulk material when viewed under an optical microscope. The location previously occupied by white etching band and the bulk material had similar hardness values.

2.7.2 Grain Elongation and Fragmentation

This is one of the mechanisms that have been put forward by some researchers [20,34] to explain the fine equi-axed grains inside transformed band in steel and is schematically presented in Figure 2.2. The process of grain elongation and fragmentation (Fig 2.2) first involves the elongation and alignment of grains parallel to the direction of deformation. The elongated grains are continuously deformed in the shear flow direction. The elongated grains subsequently become partitioned by transverse cell walls through dislocation movement under high hydrostatic pressure and shear stress leading to the formation of equi-axed cellular structures [20,34]. This mechanism is attributed to the fragmentation of lamellae and densely packed cementite along shear direction observed by Chen *et al.* [34].

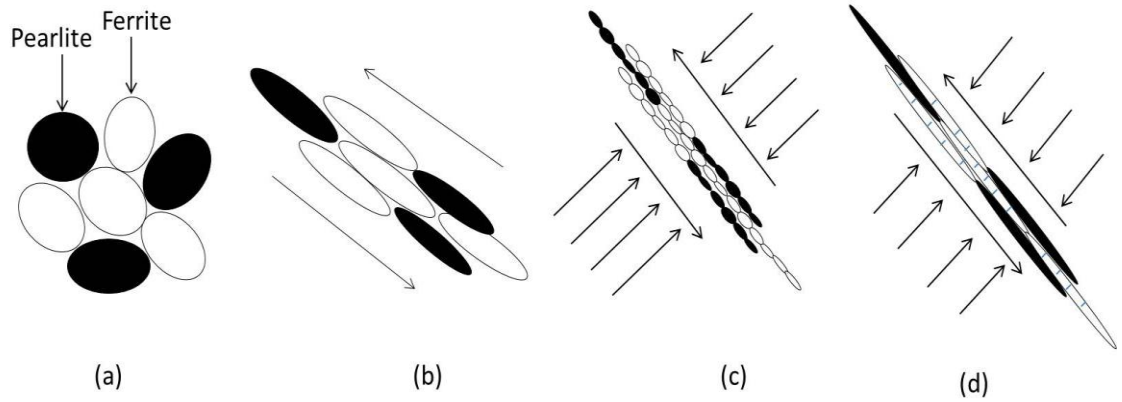

Figure 2.2. Typical schematic illustration of grain elongation and fragmentation mechanism (a) original pearlitic structure, (b) Reorientation and elongation of cementite in shear direction, (c) Cell walls formed on the elongated grains by dislocation movement under high hydrostatic pressure and shear stress, (d) Fragmentation of lamellae and densely packed spheroidization of the cementite in shear direction [adapted from reference 34].

2.7.3 Dynamic Recovery and Dynamic Recrystallization

Recovery

Recovery is the earliest onset of re-arrangement of dislocation within the cold worked material at elevated temperature, where some restoration of the original structure and some physical properties may occur through annihilation and spatial re-arrangement of dislocations. It is called recovery because it describes the processes that lead to the recovery of mechanical properties on heating a deformed metal. The two main types of recovery mechanisms are static recovery and dynamic recovery. Static recovery is a type of recovery that is reliant on the heating of an existing deformed microstructure. Dynamic recovery is a type of recovery that occurs during deformation, particularly at elevated temperatures. After recovery, grains keep their original shapes meaning that the decrease in internal energy is not as a result of any change in grain boundary areas.

Dynamic recovery (DRV)

During the initial stages of deformation, an increase in flow stress occurs as dislocations interact and multiply. But, as the dislocation density increases, the driving force for recovery and rate of recovery increases. A microstructure of low angle boundaries and sub-grains develops. At a certain strain, the rates of work hardening and recovery reach a dynamic equilibrium. The dislocation density remains constant and steady state flow stress is obtained. Some sub-grain growth occurs. Within the subgrains, the processes of work hardening and recovery lead to continuous formation of low angle boundaries and to a constant density of unbound or "free" dislocations within the sub-grains. During deformation at strain rates larger than approximately 1 s^{-1}, the heat generated by the work of deformation cannot be removed from the specimen and the temperature of the specimen rises during deformation [74,75].

In dynamic recovery mechanism, dislocations first begin to tangle leading to the formation of dislocation cells. These dislocation cells then begin to undergo dislocation annihilation via two mechanisms. The first mechanism being the annihilation of dislocations with opposite sign but having equivalent Burgers vector and the second

mechanism is Polygonisation. Polygonisation is the re-arrangement of dislocations either by glide and climbs (edge dislocations) or cross slip (screw dislocations). Such polygonization is also found as a function of time in static recovery (SRV) but at a much lower, declining rate as driven by substructure stress fields whereas dynamic recovery (DRV) is driven by constant applied stress or strain rate [76]. After annihilation, the formation of subgrains and its subsequent growth occurs. For the subgrains to migrate, atomic diffusions are needed. This readily occurs in regions where the crystal structure of the metal is disturbed. Hence, as sub-grain mobility increases, misorientation also increases. The sub-grains tend to also rotate by grain boundary diffusional processes until adjacent grains are of similar rotation. The two sub-grains coalesce to form a large grain with little boundary migration. The driving force for the grain rotation process is the reduction in the total gain boundary area and grain boundary energy. After sub-grain coalescence, the growth process begins through the process of sub-grain coarsening. The sub-grain coarsening helps to reduce the stored energy of the recovered sub-structure by reduction in total sub-grain boundary energy. During coarsening, small sub-grains will be consumed by larger ones and the overall sub-grain size will increase. Subgrain coarsening is a thermally activated process and requires both glide and climb of dislocations. This process is accelerated by increasing temperature. The driving force for sub-grain growth arises from the energy stored in the sub-grain structure [77 – 80].

Recrystallization

In contrast to recovery (static or dynamic), which occurs uniformly throughout the microstructure, recrystallization involves the nucleation and growth of strain free grains in certain areas of the material, which grow to consume the deformed or recovered microstructure. It entails how a heavily deformed microstructure transforms into one with new, strain and dislocation free grains. Recrystallization can be divided into static and dynamic recrystallization. In static recrystallization, the microstructure develops subsequent to deformation but in dynamic recrystallization, the recrystallized microstructure develops simultaneously with deformation. Static recrystallization process is divided into two stages; First stage is the nucleation of new strain free grains

and the second stage is grain growth during which new grains replace the deformed metal.

Dynamic recrystallization (DRX)

In dynamic recrystallization, new grains containing lower dislocation density are formed along initial grain boundaries. Derby *et al.* [81] broadly classifies the mechanism into either migrational or rotational type of dynamic recrystallization. Bailey and Hirsch [82] proposed a recrystallization mechanism called strain induced boundary migration (SIBM). Here, recrystallization tends to occur due to differences in dislocation density across an existing high-angle grain boundary particularly in a cold worked metal. The strain energy difference as a result of the driving force causes a portion of the high angle grain boundary to migrate into the subgrain with the higher dislocation density. As the high-angle boundary cuts across the deformed structure, dislocations are eliminated thereby producing strain-free nucleus which will continue to grow through grain-boundary migration. Due to the temperature rise inside shear band and the short time associated with it, the migrational mechanism alone cannot occur either in deformation or cooling and cannot be used to the formation of the recrystallized structure [26]. Therefore, there is the need to find alternative explanations. Another recrystallization mechanism involving subgrain coalescence was suggested [83,84]. Unlike in SIBM, subgrains are formed. These subgrains rotate to form creating larger subgrains through the process of eliminating the unfavorable energetic low-angle boundaries. Larger misorientations between other subgrains are also generated due to the subgrain rotation. Such misorientations lead to the formation of high-angle grain boundaries and hence, the formation of new recrystallized grains [85]. Meyers *et al.* [26,86] proposed a mechanism for rotational dynamic recrystallization. He explained, in details, the formation of the subgrains from dislocations. He explained that homogeneously distributed dislocations rearrange themselves into elongated dislocation cells (Fig 2.3b). These elongated dislocation cells become patterned to form elongated subgrains as deformation increases (Fig 2.3c). As deformation increases, these subgrains then break up into equi-axed micrograins (Fig 2.3d) due to minimization of interfacial energy [26,86]. Finally, the recrystallized microstructure is formed. Fine equi-axed

grains of about 0.05 – 2μm sizes has been reported formed in shear band of titanium [87].

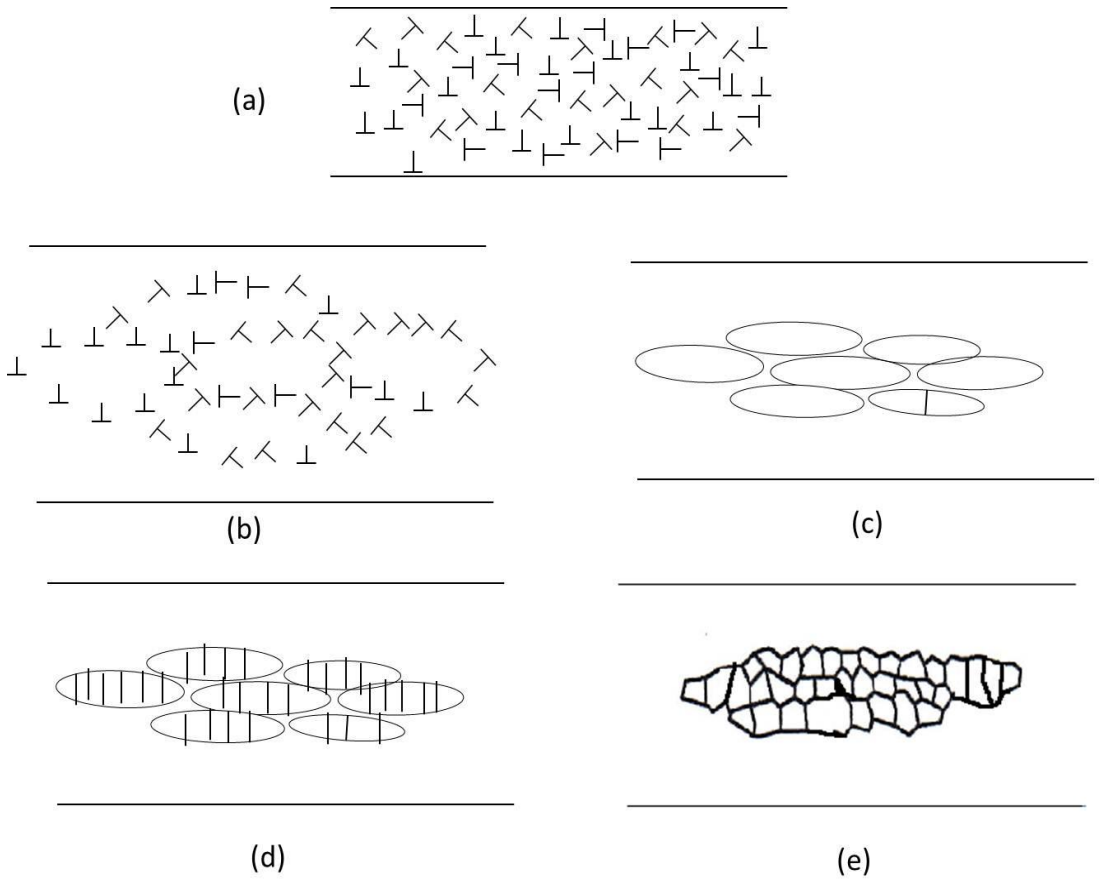

Figure 2.3. Typical schematic illustration of dynamic recovery and dynamic recrystallization mechanism. (a) Randomly distributed dislocations; (b) formation of elongated dislocation cells; (c) formation of elongated subgrains; (d) Initial break-up of elongated subgrains; (e) Recrystallized microstructure [adapted from references 26 and 86].

As discussed in section 2.7.3, it is a known fact that during dynamic recrystallization, the recrystallized microstructure develops simultaneously with deformation. This indicates that the consequence of dynamic shear localization is dynamic recrystallization. This point has been questioned by Rittel *et al.* [12]. In his study of the response of Ti6Al4V alloy to adiabatic shear failure, he observed a strange behaviour. During the test, he loaded some samples to failure in well-defined stress concentration

area while he loaded the rest up to half the strain to failure. In the partially loaded samples, the stress-strain curve was in the strain-hardening region where the effect of temperature is quite small. It was discovered that both the fully loaded and partially loaded samples show qualitatively similar microstructures. The presence of very small dynamically recrystallized grains with low dislocation density which is evidence of dynamic recrystallization was observed. The presence of these grains means that dynamic recrystallization can form even before strain localization starts. Hence, he concluded that dynamic shear localization is actually the consequence of dynamic recrystallization [12].

2.7.4 Progressive Subgrain Misorientation (PriSM) Recrystallization

Hines *et al.* [30,51,88] recently studied the recrystallization mechanism in copper at high strain rates. He observed that the classical recrystallization mechanisms are far too slow to account for the observed recrystallization inside transformed shear bands. This means the kinetics of classical recrystallization models cannot account for the microstructural evolution taking place inside shear band at high strain rate under temperature and strict time conditions. In order to account for the microstructural evolution taking place inside the shear band, a new model of recrystallization mechanism called progressive subgrain misorientation (PriSM) recrystallization (Fig 2.4) was proposed by Hines *et al.* [30]. This model is schematically presented in Figure 2.4 and is based on mechanically-assisted subgrain rotation that is kinetically feasible in the stringent time and temperature profile of an adiabatic shear band in certain metals. It is however different from the rotational recrystallization in the sense that it allows for the formation of recrystallized grains at high strain rates and it requires sufficient heat and time for boundary refinement to occur [30].

The size of subgrains in a typical recrystallized microstructure is observed to have an inverse proportionality with the applied stress during deformation [30,51,89-91]. As strain or strain rate increase, the subgrain size continues to reduce in size until a critical subgrain size is reached. At this point, further increase in strain or strain rate will no longer affect the subgrain size. Hence, the inverse relationship between the applied

stress and subgrain size no longer exist. Because these subgrains can no longer reduce in size, they begin to rotate in order to accommodate further deformation thereby causing the formation of highly misoriented equi-axed region inside the shear band. Since no dislocations are added to the grain boundaries during cooling at the end of the deformation process, the boundaries begin to refine themselves by the reduction of the excess dislocation dipoles through dislocation annihilation by dislocation climb [30,51]. The presence of sufficient time during cooling for the occurrence of boundary refinement will lead to the development of faceted high-angle boundaries thereby and causing the recrystallization of grains [30].

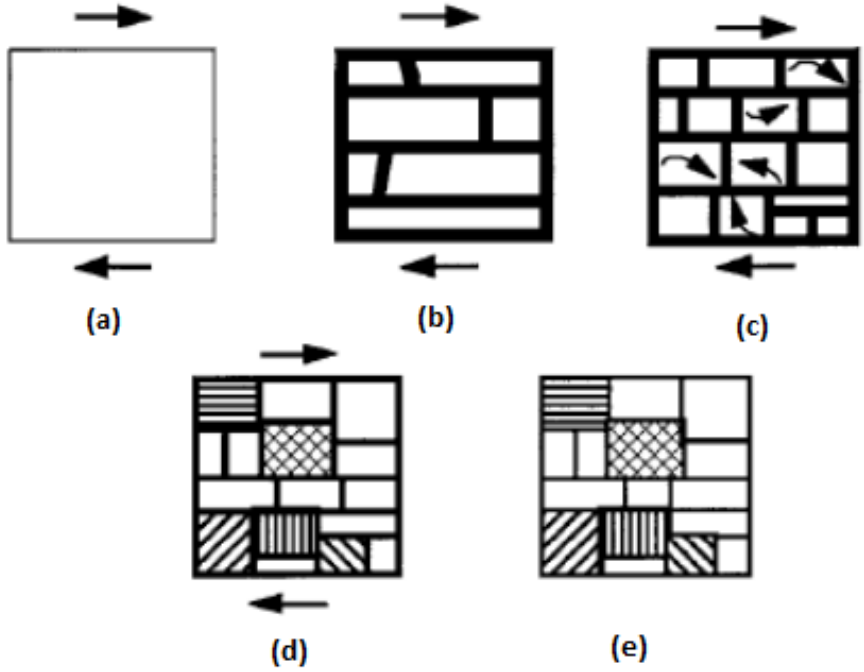

Figure 2.4. Typical schematic illustration diagram of recrystallized grain evolution in an adiabatic shear band showing (a) The starting single crystal, (b) The formation of elongated subgrains, (c) Rotation of equi-axed subgrains, (d) High-angle misorientations between some subgrains, and (e) Boundary refinement during cooling [adapted from 30].

2.8 Adiabatic Shear Failure

In section 2.6, initiation of adiabatic shear bands during high strain rate deformation of a material is reported to be influenced by inhomogeneity in the material. Adiabatic shear bands can serve as precursors and preferential sites for failure, which can occur by ductile void nucleation, growth and coalescence which develop into crack that lead to fragmentation along the shear band. Thermal softening during localized adiabatic heating causes sudden drop in flow stress within the shear band region. As a result of the stress gradient which develops between the bulk matrix and the shear band, tensile stress is generated which open up voids in the shear bands [92,93]. The distribution of potential weak points as well as the sizes and shapes of these weak points can greatly affect the formation of voids [94]. Cracks are initiated once the critical shear strain has been exceeded. Such fracture points are observed to be microvoids nucleated at weak points such as notch in the shear-zone microstructure, or sections of the shear surfaces which have undergone significant thermal softening with respect to the adjacent matrix [94]. The extent of damage resulting from the stress gradient however depends on the - magnitude of tensile stress across the shear band [95]. Three scenarios for damage evolution inside shear band are proposed by Timothy *et al*. [94]. When the space between microvoids are wide inside the shear band, the microvoids grow under combined tensile and shear stresses acting on the shear band but do not coalesce (Fig 2.5a). The microvoids can be circular or elliptical in shape. When the space between the microvoids is at the critical void separation or slightly below it, the forces acting on the surfaces of the microvoids causes them to coalesce (Fig 2.5b). However, when the space between the microvoids is so small, the thermal softening causes a rapid coalescence of the microvoids (Fig 2.5c) [94]. The process of crack coalescence leading to crack formation involves; the formation of pores in ASB generated by tensile stress, the coalescence of pores to form pore clusters along the ASB, the formation of extremely fine micro-cracks parallel to ASB, the interconnection and growth of micro-cracks, and finally the propagation of the crack and subsequent failure.

In this chapter, the mechanism of deformation and failure of engineering materials at high strain rates is reviewed. At high strain rates, deformation process is controlled by

competing processes of strain hardening and thermal softening. When thermal softening dominates, strain localization occurs and adiabatic shear bands (ASBs) are formed. These ASBs are categorized into deformed and transformed bands. The study of adiabatic shear bands in aluminum alloys reveal distorted grain structure in deformed bands while those of transformed bands show fine equi-axed structure. Factors such as temperature rise inside the shear band, applied stress and critical strain and strain rates have been observed to affect the formation of these shear bands. Initiation mechanism such as grain size inhomogeneity helps govern the initiation of shear bands. The mechanisms of adiabatic shear bands such as phase transformation, grain elongation and fragmentation, dynamic recovery and dynamic recrystallization are discussed. The modes of failure of these shear bands were also reviewed.

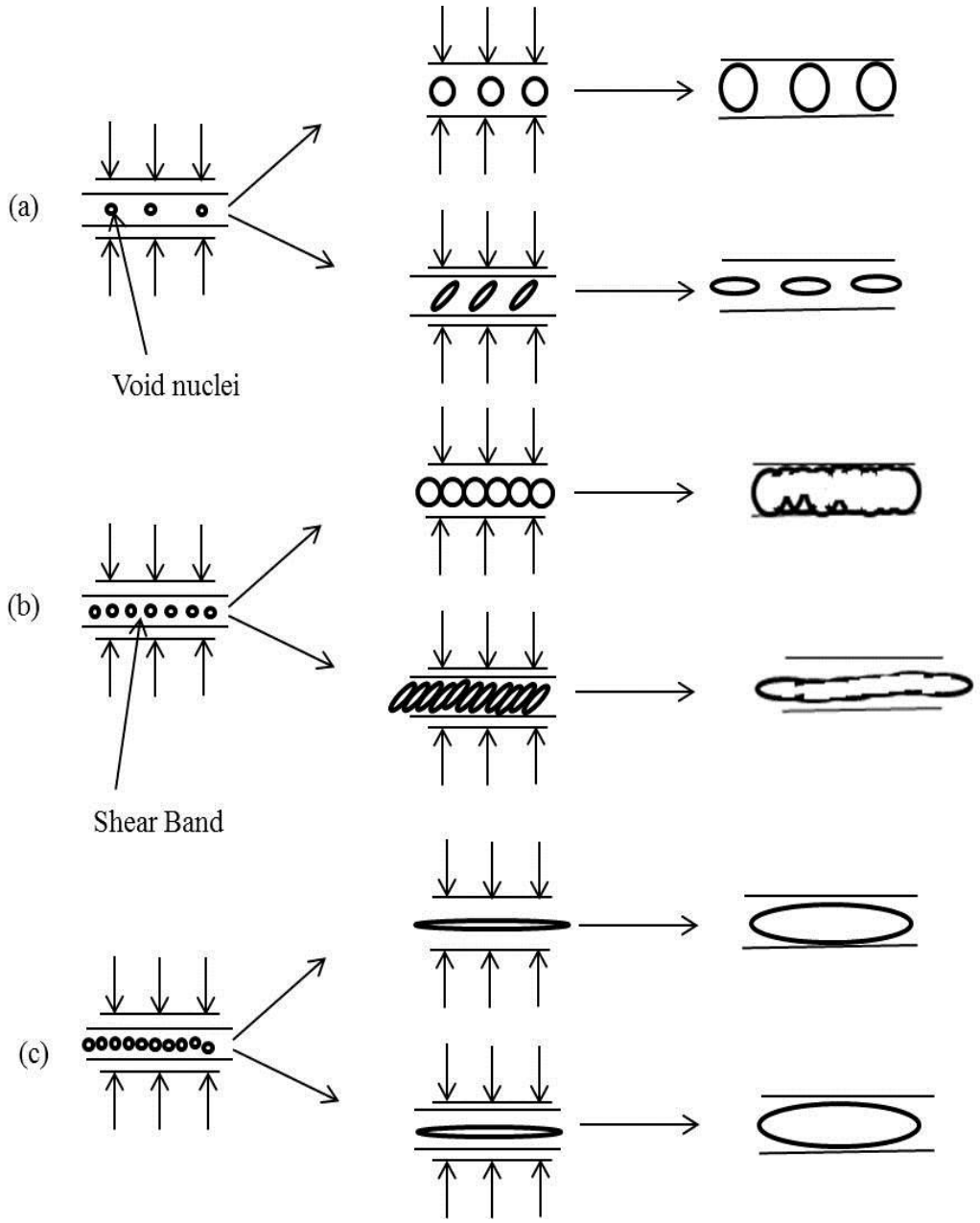

Figure 2.5. Processes leading to adiabatic shear failure in shear band with (a) wide void separation; (b) Critical void separation; (c) Very small void separation [adapted from 94].

3. MATERIALS AND METHODS

This chapter briefly discusses the materials used in this research, the heat treatment procedure as well as the hardness, quasi-static compression, direct impact and dynamic torsion test procedures. Microstructural analysis using optical microscope, scanning electron microscope and X-ray photoemission electron microscopy (X-PEEM) with near edge X-ray absorption fine structure (NEXAFS) spectroscopy will also be discussed.

3.1 Materials

The two materials investigated in this research study were AA2099 and AA6061 aluminum alloys. The elemental compositions of the alloys from ALCOA product data sheet are given in Table 3.1. The AA2099 alloy was received in T8 temper condition while the AA6061 alloy was received in T6 temper condition. The major alloying elements in 6061 are Cu, Mg and Si while the AA2099 contains Cu, Mg and Li as the principal alloying elements. AA2099 aluminum alloy contains more copper addition than AA6061 but no silicon. However, AA6061 aluminum alloy contains no lithium. Specimens used for the dynamic impact test were cylindrical specimen 10.5 mm in length and 9.5 mm in diameter while specimens for the high strain rate torsion test were thin-walled tubes 0.4 mm thick with a gage length of 3.82 mm. Figure 3.1 shows a schematic representation of the geometry of the test specimens.

Table 3.1. Elemental composition of the investigated AA2099 and AA6061 aluminum alloys.

Sample	Elemental composition (%)								
	Al	Li	Cu	Mg	Si	Zn	Mn	Zr	Cr
AA2099	> 95	1.6-2.0	2.4-3.0	0.1-0.5	-	0.4-1.0	0.1-0.5	0.05-0.12	-
AA6061	> 95	-	0.15-0.4	0.8-1.2	0.4-0.8	< 0.25	< 0.15	-	0.04-0.35

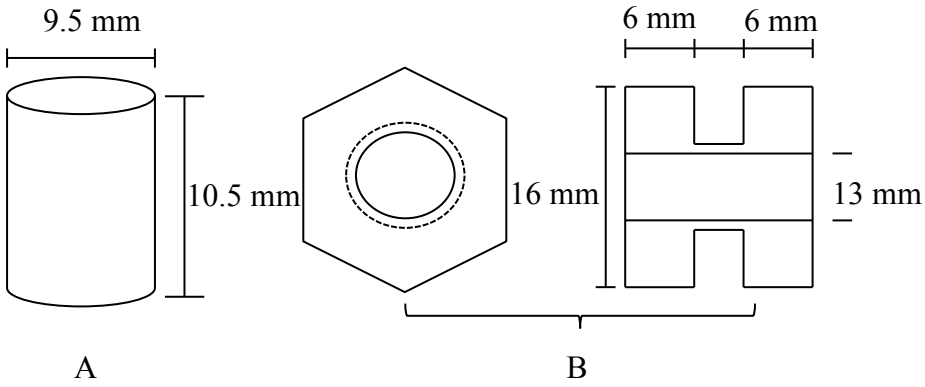

Figure 3.1. Geometry of test specimen for (a) Direct impact test (b) Dynamic torsion test.

3.2 Heat Treatment Procedure

AA2099 and AA6061 aluminum alloys are heat treatable aluminum alloys. They were heat treated to different temper conditions as shown in Table 3.2. AA2099 aluminum alloy belongs to the Al-Li-Cu-Mg alloy system which is strengthened due to the formation of precipitates such as δ′ (Al_3Li), T_1 (Al_2CuLi), S (Al_2LiMg), whereas AA6061 aluminum alloy belongs to the Al-Mg-Si-Cu alloy system which are strengthened by the formation of Mg_2Si precipitate [96]. The as-received AA2099-T8 aluminum alloy was produced through a two-step artificial aging process while the as-received AA6061-T6 aluminum alloy was produced through a single step artificial aging heat treatment process. Variation in the behaviour of alloys subjected to

multi-stage aging is common as it depends on factors such as alloy composition, pre-aging temperature and time, final aging temperature [97]. The study of age hardening of Al-Li alloys [10,11] reveals that better mechanical properties are achieved using a two-step aging process in these alloys. The most common of the multi-step aging used in aluminum-lithium alloys is two-step aging. Therefore, this heat treatment process was considered in designing the heat treatment procedure for the AA2099 aluminum alloy in this research study. AA6061 aluminum alloy was however subjected to a single step artificial aging process. The heat treatment carried out involves solution heat treatment at 540 °C for 2 hours followed by quenching in water to ambient condition. Precipitation heat treatment was carried out under natural or artificial aging conditions. The entire heat treatments for both alloys were carried out using the Thermo Scientific Lindberg Blue M furnace located in room 2C26, Engineering building, University of Saskatchewan. The aging treatment procedures for the test specimen of the investigated alloys are as described in Tables 3.3 and 3.4. The temperature-time curves for the heat treatment procedure for both alloys are presented in figures 3.2 and 3.3.

Table 3.2. Heat treatment design for 2099 and 6061 aluminum alloys.

Solution Heat Treatment °C (h)	Natural Aging 22 °C (h)	Cold work, 30 kN Force (%)	Precipitation Hardening Step 1 °C (h)	Precipitation Hardening Step 2 °C (h)	Temper Condition
AA2099 Aluminum Alloy					
As-received Condition: Aging temperature and degree of cold work unknown					T8
540 (2)	Natural	-	-	-	T4
540 (2)	48	-	120 (12)	-	T61*
540(2)	48	-	120 (12)	160 (24)	T62*
540 (2)	48	9.5	120 (12)	-	T81*
540 (2)	48	9.5	120 (12)	160 (24)	T82*
AA6061 Aluminum Alloy					
As-received Condition: Aging temperature and degree of cold work unknown					T6
540 (2)	Natural	-	-	-	T4
540 (2)	48	17	-	160 (18)	T8

1 = one-step aging, 2* = two-step aging*

Table 3.3. Temper designations for AA6061 aluminum alloy.

Temper Designation	Condition
T4	Solution heat treated and naturally aged to a substantial stable condition.
T6	As received condition (one-step artificially aged).
T8	Solution heat treated, naturally aged for 48 h, 17% cold worked in compression and artificially aged at 160 °C for 18 h.

Table 3.4. Temper designations for AA2099 aluminum alloy.

Temper Designation	Condition
T4	Solution heat treated and naturally aged to a substantial stable condition.
T61	Solution heat treated, naturally aged for 48 h and single step artificially aged at 120 °C for 12 h.
T62	Solution heat treated, naturally aged for 48 h, first step artificially aged at 120 °C for 12 h and second step artificially aged at 160 °C for 18 h.
T81	Solution heat treated, naturally aged for 48 hours, 9.5% cold worked in compression, single step artificially aged at 120 °C for 12 h.
T82	Solution heat treated, naturally aged for 48 h, 9.5% cold worked in compression, first step artificially aged at 120 °C for 12 h and second step artificially aged at 160 °C for 18 h.
T8	As received condition (two-step artificially aged).

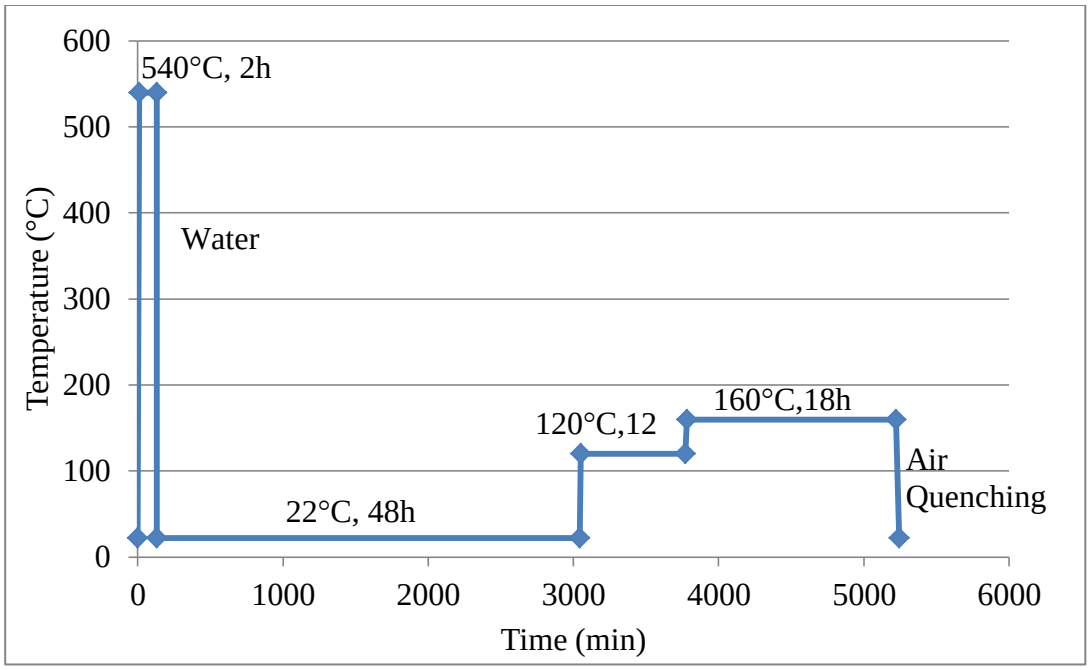

Figure 3.2. Temperature – Time graph for heat treatment of AA2099 alloy.

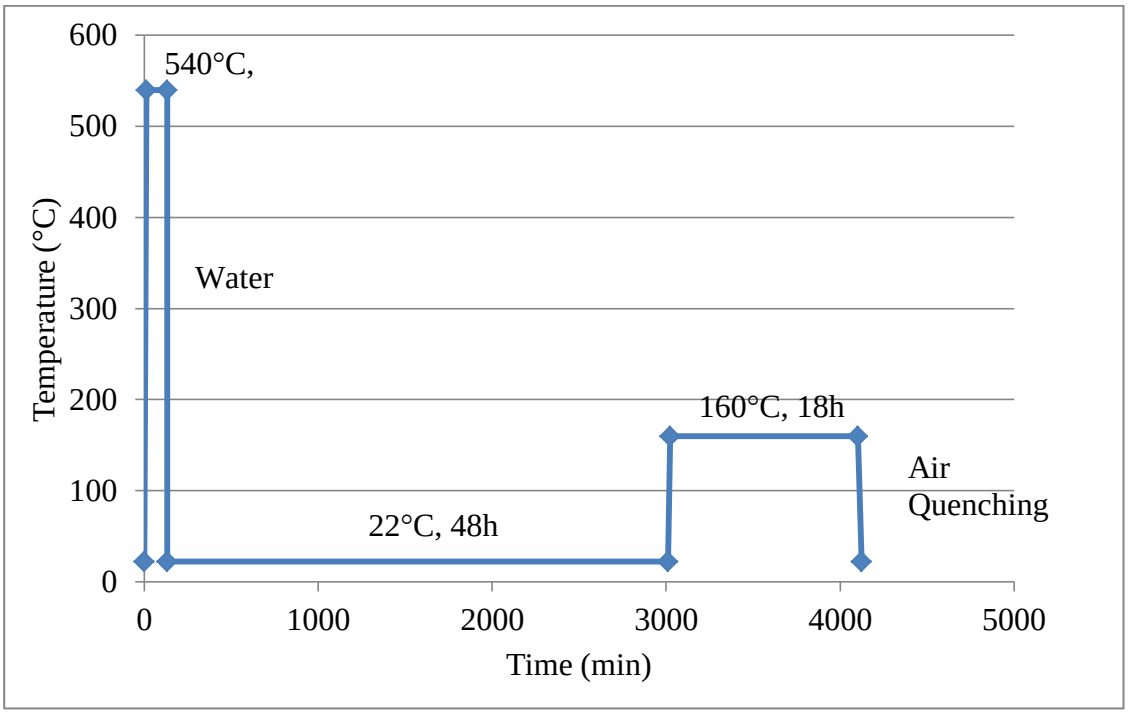

Figure 3.3. Temperature – Time graph for heat treatment of AA6061 alloy.

3.3 Quasi-static Tests

The mechanical behaviour of the alloys under quasi-static loading was determined using hardness and compression tests. Microhardness tests were carried out on the alloys under various temper conditions using Mitutoyo Micro Vickers hardness testing machine MVK-H1 located in room 2C25, Engineering Building, University of Saskatchewan, Canada. Ten (10) hardness measurements were carried along each specimen and averaged. The standard error associated with hardness measurement for each alloy temper conditions is determined.

The vickers hardness test method consists of indenting the aluminum alloys with a diamond indenter, in the form of a right pyramid with a square base and at an angle of 136 degrees between opposite faces subjected to a load of 200 gf for 10 seconds. The two diagonals of the indentation left in the surface of the alloy after removal of the load as shown in Figure 3.4 are measured using a fitted microscope with micrometer screw gauge and their average calculated. The area of the sloping surface of the indentation is calculated. The vickers hardness is the quotient obtained by dividing the load by the square mm area of indentation as shown in equation 3.1 [98].

$$HV = \frac{2Fsin\frac{136^\circ}{2}}{d^2} = 1.854\frac{F}{d^2} \quad \text{.....(3.1)}$$

where F= Load (kgf),

d = Arithmetic mean of the two diagonals, d_1 and d_2 in mm and, HV is Vickers hardness.

Mechanical behaviour of the alloys under quasi-static compression loading was investigated using a Instron R5500 mechanical testing machine located in room 1B89, Engineering Building, University of Saskatchewan, Canada. This test was carried out using a 100 kN compressive force at ambient condition at a strain rate of 0.0032 s^{-1}. Engineering strains were calculated based on the height reductions of the alloy specimens after compression test.

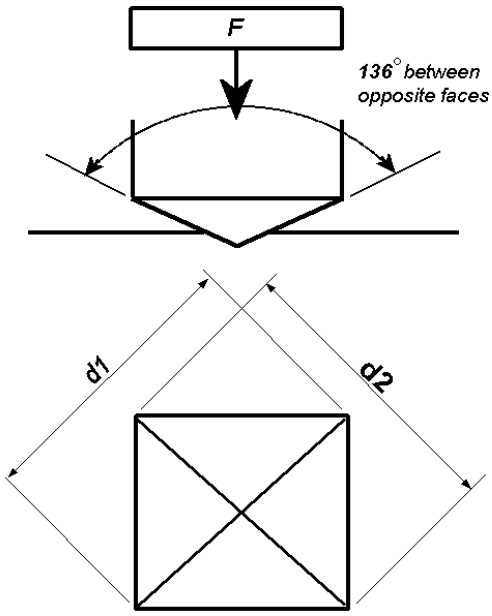

Figure 3.4. Schematic representation of vickers hardness measurement.

3.4 Dynamic Mechanical Tests

3.4.1 Direct Impact Test

High strain rate compression tests were conducted on both AA2099 and AA6061 aluminum alloys using a direct impact Hopkinson pressure bar shown in Figure 3.5. The tests were conducted at the high strain rate testing laboratory, Department of Mechanical and Manufacturing Engineering, University of Manitoba, Canada. The cylindrical test specimens were impacted using a 1.905 kg quench-hardened AISI 4340 steel bar projectile at momentum varying between 26 and 44 kg m s^{-1}. The projectile travels through the light gun barrel and strikes the test specimen attached to the output bar of the Hopkinson bar system. The output bar is also made from quench-hardened AISI 4340 steel with the same cross-sectional area as the striking projectile. The elastic waves generated when the specimen is impacted travels through the output bar and is captured by strain gage attached to it. These provide the strain signals which are conditioned, amplified and captured by the data acquisition system connected to the bar. The data acquisition system consists of strain pulse conditioner/amplifier and a mixed signal

digital oscilloscope. Dynamic stress-strain curves are generated from the captured strain signals.

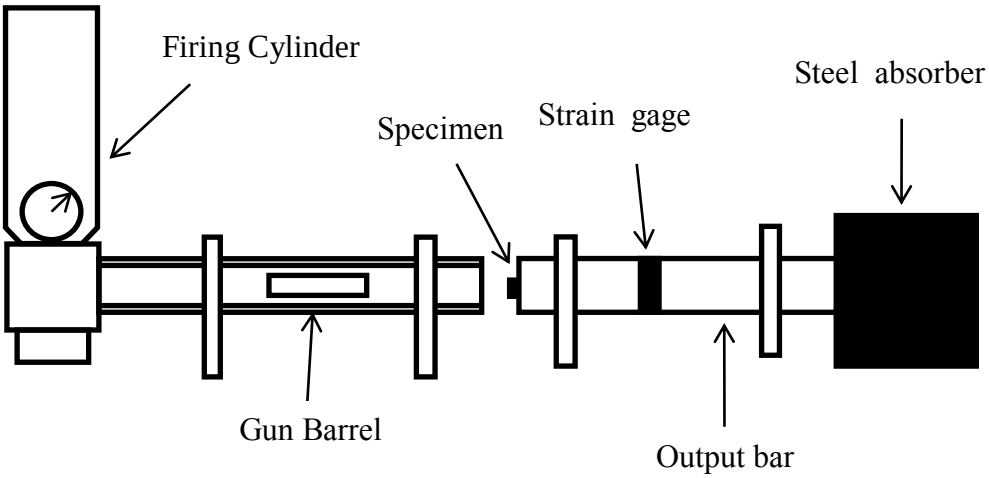

Figure 3.5. Schematic diagram of a direct impact Hopkinson pressure bar equipment

The data acquired by the data acquisition system (oscilloscope) is in form of voltage and time. The captured elastic wave data in volt are converted to load value using a conversion factor obtained from an initial calibration of the equipment. Typical voltage – time graph generated in a direct impact test is given in Figure 3.6. The calibration process involves subjecting the output bar to compressive load in steps of 100 kg load. During this process, the strain gauge on the output bar is connected to the data acquisition system to generate a voltage corresponding to each applied load. After the successive application of incremental loads, a linear plot of load (N) vs. voltage (v) is made as shown in Figure 3.7. The slope of the linear plot being 21796 N/volt is used to calculate the load corresponding to the voltage recorded by the data acquisition system. The load – voltage calibration graph is shown in Figure 3.7 and the load – voltage relationship is given by equation 3.2.

$$Load\ (N) = 21796\ \left(\frac{N}{volts}\right) * Voltage\ (volts) \quad \text{.....(3.2)}$$

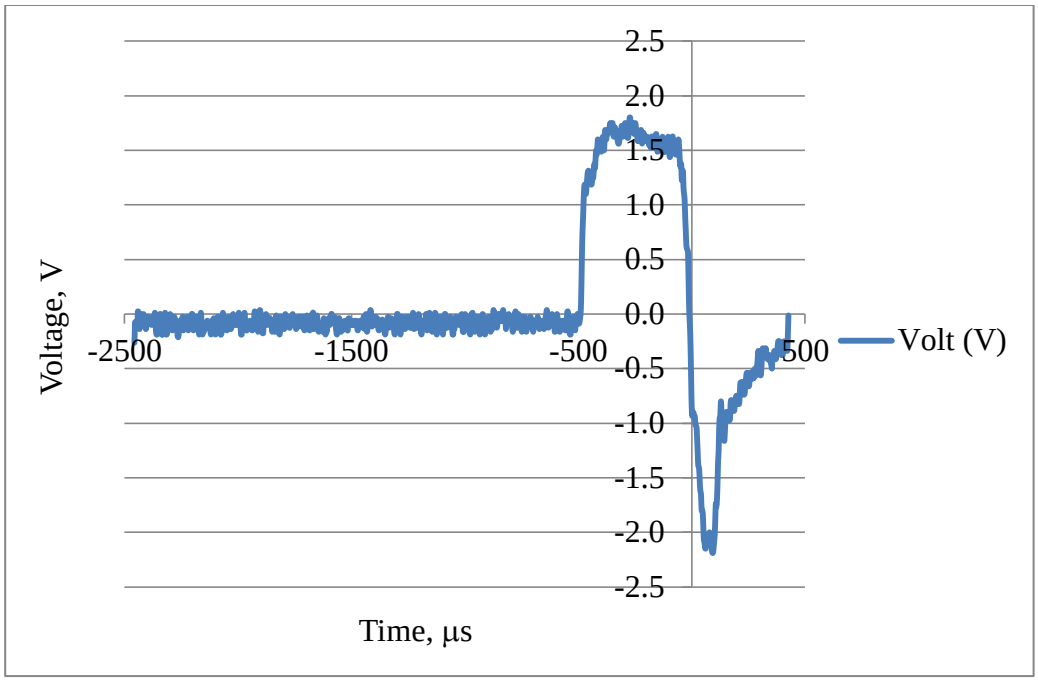

Figure 3.6. Typical voltage – time graph in direct impact test.

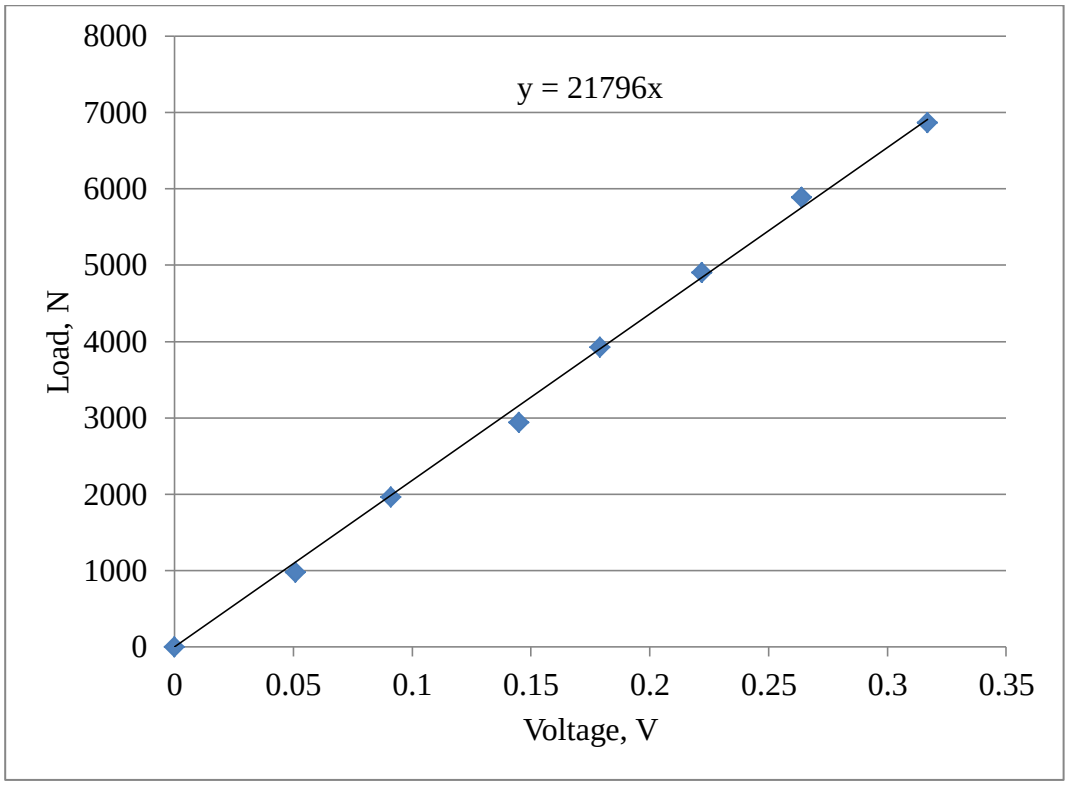

Figure 3.7. Load – Voltage calibration curve for direct impact test.

Assuming constant volume and a linear variation of displacement with time and constant strain rate, the true stress (σ) and true strain (ε) at time *t* are given by equation 3.3 [99];

$$\varepsilon_{(t)} = LN\frac{L_i}{L_i-(L_i-L_f)(t/t_f)} \quad \text{.....(3.3)}$$

$$\sigma_{(t)} = (\frac{F_{(t)}}{A_i})(\frac{L_i-(L_i-L_f)\left(t/t_f\right)}{L_i}) \quad \text{.....(3.4)}$$

where F_t is load at a given time, A_i is initial Area, and L_i and L_f are the initial and final lengths respectively.

At a constant strain rate, the maximum strain that can be achieved in a specimen is directly proportional to the length of the striking projectile. This is expressed by equation 3.5 [9].

$$\varepsilon = 2\dot{\varepsilon}\frac{L_b}{C_b} \quad \text{.....(3.5)}$$

where L_b is the length of the striking projectile (223 mm) and ε is engineering strain calculated based on change in length of specimen. C_b is the longitudinal wave velocity in the transmitting bar and it is calculated from the elastic modulus and density of the 4340 steel [9].

$$C_b = \sqrt{\frac{E}{\rho}} \quad \text{.....(3.6)}$$

where young's modulus E for AISI 4340 steel is given as 205 GPa and density ρ is given as 7850 kg m^{-3}. C_b, when calculated, is approximately 5110 m s^{-1}. Equation 3.5 was used in determining the strain rates for each impacted specimen.

3.4.2 Dynamic Torsion Test

High strain rate torsion tests were conducted on both AA2099 and AA6061 aluminum alloys using a Torsional Split Hopkinson Bar (TSHB) schematically shown in Figure 3.8, located at the high strain rate testing laboratory, Department of Mechanical and Manufacturing Engineering, University of Manitoba, Canada. Thin-walled tubes 0.4 mm thick were subjected to dynamic torsional loading at different strain rates. The torque needed to rapidly load the specimen are generated and stored in the loading end of the input bar. The stored torque is determined by the angle of twist of the loading arm. When the loading arm is released, an elastic wave is generated which travels rapidly through the input bar and is recorded as incident wave by the strain gage attached to the input bar. On reaching the specimens, fraction of the elastic waves is utilized in deforming the specimen and is transmitted through the specimen on to the output bar as transmitted wave, captured by the strain gage attached to the output bar. The remaining fraction of the elastic wave that reaches the specimen is reflected back as a reflected wave, which is captured by the strain gage attached to the input bar. These three waves provide the strain signals which are conditioned, amplified and recorded by the data acquisition system connected to the bar. The data acquisition system consists of a strain pulse conditioner/amplifier and a mixed signal digital oscilloscope. Dynamic stress-strain curves are generated from the captured strain wave signals. Both input and output bars are made from AA6061 aluminum alloy and have a length of 1.829 m each and a diameter of 25.4 mm.

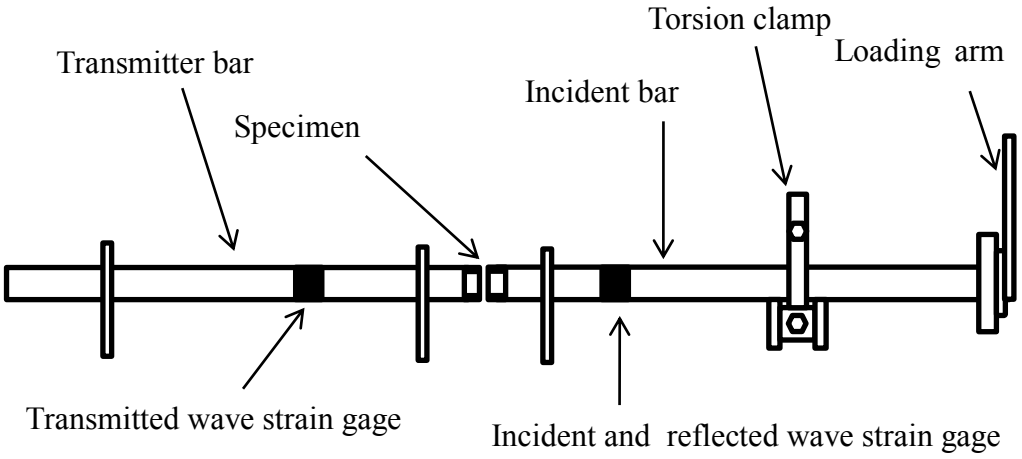

Figure 3.8. Schematic diagram of a torsional split Hopkinson bar equipment.

The data acquired by the data acquisition system (oscilloscope) are in form of voltage and time. Two sets of voltage data are generated (volt-1 and volt-2). Volt-1 data account for both incident and reflected wave signals while volt-2 data account for the transmitted wave signal data. The captured elastic wave data in volt are converted to shear strain values using two conversion factors obtained from an initial calibration of the equipment. A typical voltage vs time graph obtained from the torsion test is given in Figure 3.9.

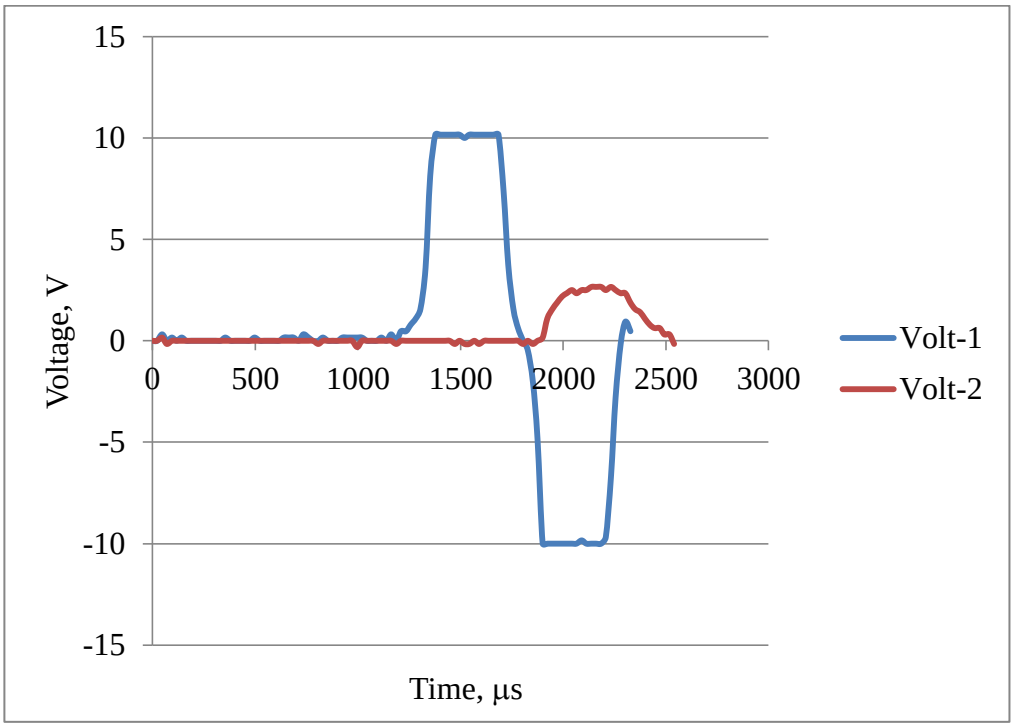

Figure 3.9. Typical voltage – time graph in torsional split Hopkinson bar test.

The bar was calibrated by clamping the end of the out bar and preventing rotation of this end. Calibration was used to obtain the factor for conversion of voltage from the oscilloscope to shear strain. Torque was applied at incremental values of angle of twist of 1 ° at the loading end of the input bar. The voltage measurement by the strain gages on the input and output bar are recorded against the correspondence value of shear strain at the location of the strain gages. The shear strain produced for each angle of twist can be calculated as a function of the combined length of the input and output bars of the torsional split Hopkinson pressure bar as follows.

$$\gamma_s = \frac{\theta D_b}{2L} \quad \text{.....(3.7)}$$

where θ is angle of twist (rad), D_b is diameter of bar and L is the combined length of both input and output bar. The shear strains calculated from the above equation at each angle of twist is plotted against the voltages recorded by the data acquisition system for input and output bar as shown in Figures 3.10 and 3.11. The slope of the line gives the relationship between the recorded voltage and the corresponding shear strain at the location of the strain gages. Using the slopes of the lines incident strain signal (γ_I), reflected strain signal (γ_R) and the transmitted strain signal (γ_T) can be calculated as shown in equations 3.8 – 3.10.

$$\gamma_I = 0.000117012\ (Volts^{-1}) * Incident\ wave\ signal\ (Volts) \quad \text{.....(3.8)}$$

$$\gamma_R = 0.000117012\ (Volts^{-1}) * Reflected\ wave\ signal\ (Volts) \quad \text{.....(3.9)}$$

$$\gamma_T = 0.000117144\ (Volts^{-1}) * Transmitted\ wave\ signal\ (Volts) \quad \text{.....(3.10)}$$

where γ_I, γ_R, γ_T are incident signal, reflected signal and transmitted signal, respectively.

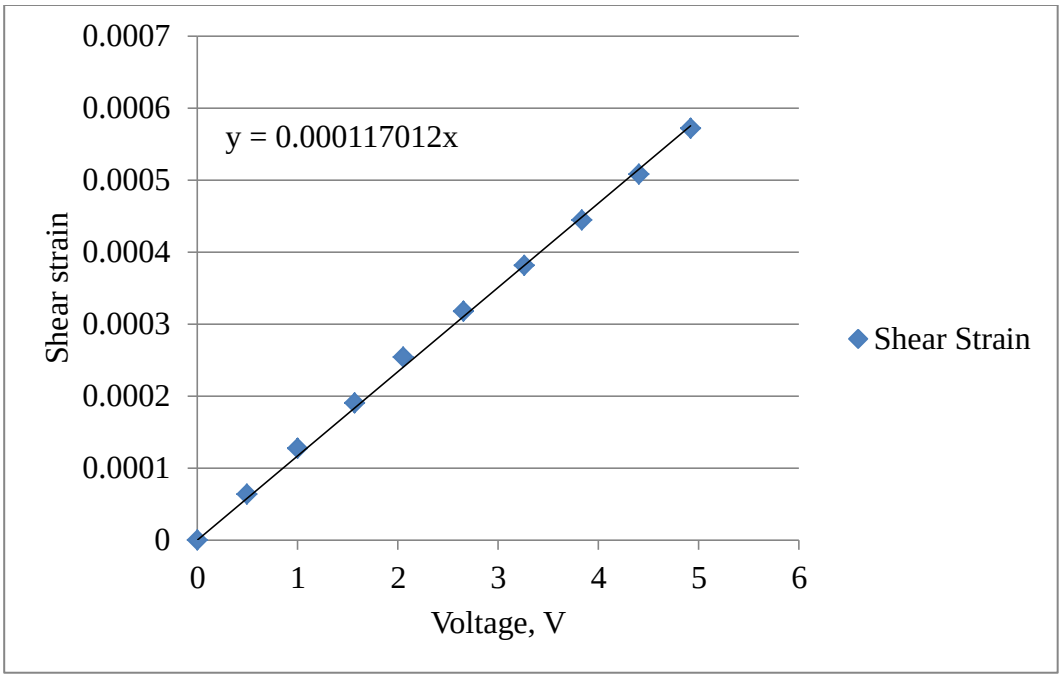

Figure 3.10. Shear strain vs. voltage plot obtained for input bar during equipment calibration of torsional split Hopkinson bar.

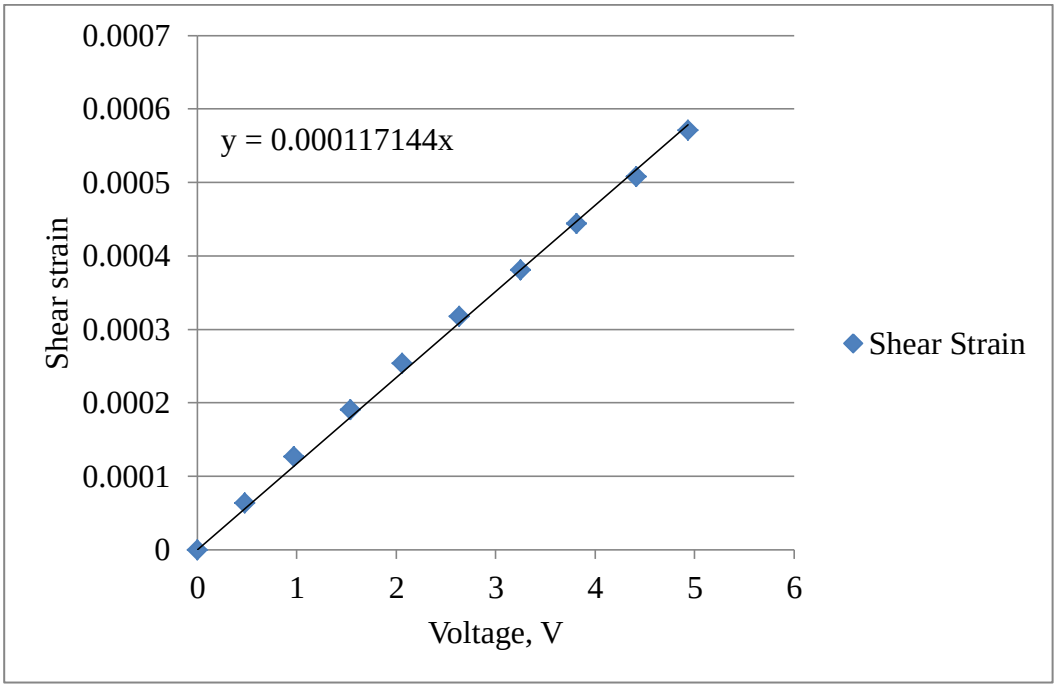

Figure 3.11. Shear strain vs. voltage plot obtained for output bar during equipment calibration of torsional split Hopkinson bar.

When one strain gauge is employed to capture both incident and reflected wave signals on the input bar, the strain rate and strain in the specimen are expressed as a function of only the reflected strain signal as shown in equations 3.11 and 3.12 [8].

$$\dot{\gamma}_s\,(t) = \frac{r_s}{L_s}\frac{2C}{r_b}[-\gamma_R(t)] \quad \text{.....(3.11)}$$

$$\dot{\gamma}_s = \frac{r_s}{L_s}\frac{2C}{r_b}\sum[\gamma_R(t)]\Delta t \quad \text{.....(3.12)}$$

where r_s is the mean radius of the thin-walled specimen, r_b is the radius of the bar, L_s is gauge length of the specimen, C is wave propagation velocity of the bar and Δt is difference between succeeding time and previous time. The negative sign is added to nullify the negative direction of the reflected wave as a function of time.

The shear stress, τ_s in the specimen is determined as a function of the amount of torque in the specimen, T_s and wall thickness t_s. For a thin-walled specimen, the shear stress is expressed in Eqn 3.13 [100].

$$\tau_s = \frac{T_s}{2\pi r_s^2 t_s} \quad \text{.....(3.13)}$$

where t_s is the wall thickness of the thin-walled specimen.

Assuming uniform stress throughout the specimen, the torque generated at each end of the specimen becomes the same. This means that the torque in the specimen is the same as the torque of the signal transmitted to the output bar. The shear stress in the specimen at any given time t expressed as a function of strain gauge on the output bar as shown in equation 3.14 [100].

$$\tau_s(t) = \frac{Gr_b^3}{4r_s^2 t_s}\gamma_T \quad \text{.....(3.14)}$$

where G is the shear modulus of the material.

The torque generated in the loading arm of the bar was calculated using Eqn 3.15 [100].

$$T_s = \frac{\theta G \pi D_b^4}{32 L_a} \quad \text{.....(3.15)}$$

where θ is angle of twist in rad, G is the shear modulus, D_b is the diameter of the bar and L_a is the length of the loaded arm of the shaft (430 mm).

3.5 Microstructural Analysis

Detailed microscopic examination of both AA2099 and 6061 aluminum alloy samples in their various temper conditions before and after impact was carried out. The samples were first mounted in acrylic and cured. After mounting, the samples were polished to remove all the slip lines due to cutting and then reveal a mirror surface. 120 Grit SiC paper was first used to grind the surface of the specimen and clean water was used in washing away the residue. Polishing cloth used were 9 micron MD Allegro cloth, 3 micron MD Mol cloth, 1 micron MD Nap cloth and 0.5 micron Ops cloth. Polishing solutions used with the corresponding polishing clothes were 9 micron MD Allegro solution, 3 micron MD Mol solution, 1 micron MD Nap solution and 0.5 micron Ops solution. The obtained mirror surface was etched using a solution containing 100 ml Methanol, 100 ml HNO_3, 100 ml HCl and 4 drops of HF. This etchant was used to etch both un-impacted and impacted alloy specimens. The duration of etching for AA2099 aluminum alloy specimens was 60 seconds while that of AA6061 aluminum alloy specimens was 40 seconds.

Optical microscopic examination of the etched specimens was carried out using a Nikon 100 MA Eclipse inverted optical microscope located in room 2C25, Engineering building, University of Saskatchewan, Canada. Attached to the microscope is a computer with an image processing software, *Pax-it!*, for image analysis. Optical micrographs were taken using this microscope at X50, X100, X500 and X1000 magnifications. Scanning electron microscopic examination of the specimen was carried out using JOEL JSM-6010LV scanning electron microscope (SEM) located in room 2C25, Engineering building, University of Saskatchewan, Canada. Backscattered and

secondary electron imaging techniques were used during the imaging at magnifications ranging from X50 to X25000. Acceleration voltage used range between 15 kV and 20 kV. X-ray photoemission electron microscopy (X-PEEM) with near edge X-ray absorption fine structure (NEXAFS) spectroscopy at the soft x-ray spectromicroscopy (SM) beamline, the Canadian Light Source, Saskatoon, Canada was used to analyse the chemistry of the microstructure inside and adjacent to the shear bands in the AA6061-T6 alloy to reveal variation (if any) in elemental composition or phase change inside the shear bands.

4. RESULTS AND DISCUSSION

In this chapter, the results of the mechanical tests and microstructural investigations outlined in chapter three are presented and discussed. The first part of this chapter focusses on the results of hardness and quasi-static compression tests on AA2099 and AA6061 aluminum alloys in the various investigated temper condition stated in chapter three and on the sequence of precipitation reactions in both alloys. The second part discusses the results of the responses of both alloys to high-strain rate loading, both in compression and in torsion as influenced by temper condition and strain rates. The third part focuses on the results of microstructural investigation of the alloys before and after high strain-rate loading to determine the damage evolution during dynamic shock loading.

4.1 Quasi-static Mechanical Test

4.1.1 Hardness Test

Figure 4.1 shows the results of the hardness tests carried out on both AA2099 and AA6061 aluminum alloy for various temper conditions. The same hardness value recorded for both T4 and T81 temper conditions of AA2099 alloy indicate that the first step precipitation hardening lasting 12 h did not have any noticeable effect on the hardness. However, the second step precipitation hardening produced a noticeable effect on hardness with the effect being more significant for the alloy in T82 temper condition. Comparable hardness values are also observed between T82 and T8 temper conditions of AA2099 alloy. The T8 is the as-received temper condition for AA2099, which was also subjected to a two-step artificial aging by the producer (Alcoa Inc.). Its hardness is only slightly lower than that of the T82 temper condition that was produced in course of this study at the University of Saskatchewan. The higher hardness recorded in AA2099-T82 compared to AA2099-T62 is attributed to a pronounced effect of

dislocation generated by cold work on precipitation hardening of the alloy. This will be discussed in detail in section 4.1.3.

From the results of the hardness test carried out on various temper conditions of AA6061 aluminum alloy, the T4 temper showed the lowest hardness value. Both T6 and T8 tempers showed comparable hardness values in AA6061 alloy. This means the effect cold work had was little on precipitation hardening of AA6061 alloy. This explains why AA6061 aluminum alloy is always produced in the T6 temper condition since an additional effort of cold working prior to age-hardening does not produce any significant effect on the precipitation hardening process. It is evident from Figure 4.1 that higher hardness values are achieved in the AA2099 aluminum alloys compared to those of AA6061 for all temper conditions. For example, AA6061-T4 showed much lower hardness compared to that of AA2099-T4. However, AA2099 in T4 temper condition has hardness value that is comparable to precipitation and strain hardened AA6061-T8 alloy. A high hardness value is an indication of higher resistance to localised deformation. This means AA2099 aluminum alloy has a higher resistance to localised plastic deformation than AA6061 alloy. The reason for the higher hardness in AA2099 will be discussed in relation to other mechanical properties in subsequent sections.

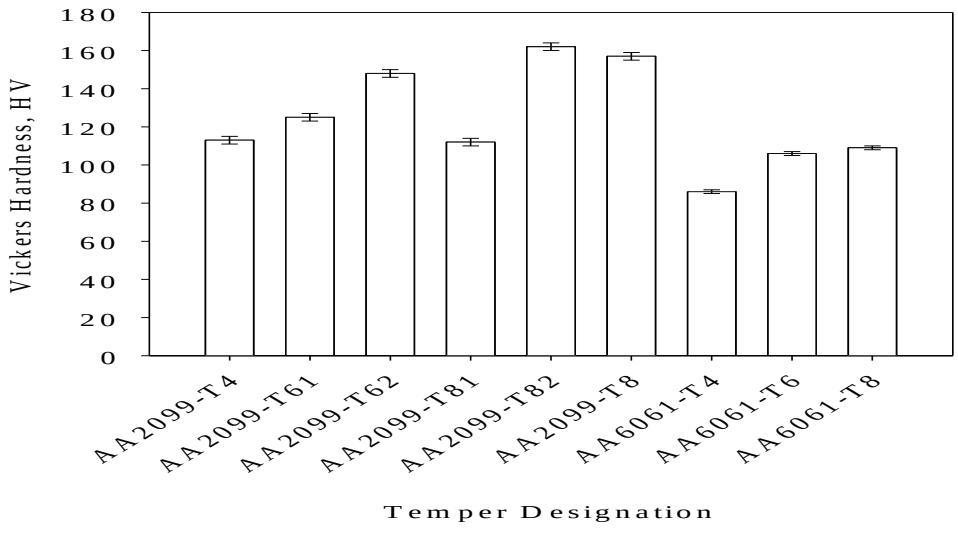

Figure 4.1. Result of vickers hardness test for AA2099 and AA6061 aluminum alloys as a function of temper condition and the associated standard error.

4.1.2 Compression Tests

Figures 4.2 and 4.3 show typical stress-strain curves obtained for AA2099 and AA6061 aluminum alloys in various temper conditions which were tested under compressive loading using a strain rate of 0.0032 s^{-1}. The total engineering strain at an applied load of 100 kN and the compressive yield strength of the alloys are presented in Table 4.1. At the applied maximum load of 100 kN, the alloys were not stressed to failure. Low engineering strain and high compressive yield strength are indications of high resistance to deformation. The comparable total engineering strain values obtained for AA2099 alloy in T4 and T61 temper conditions means one-step aging process does not have any effect on the resistance of the alloy to plastic deformation. Lower engineering strains were recorded in two- step aged alloys compared to the one-step aged alloys. In terms of compressive yield strength and total engineering strain, the alloy in T82 temper condition that is synthesized in our laboratory via a two-step age-hardening process shows a slightly more superior mechanical behaviour to the corresponding as-received AA2099-T8 alloy. The lower engineering strain and higher compressive yield strength recorded for the AA2099-T8 alloy than for the alloy in T61 and T62 temper conditions is attributed to the pronounced effects of dislocation on precipitation hardening of the alloy as will be discussed in section 4.1.3. These results are in-line with the result of hardness test. For AA6061 alloy, strain hardening prior to precipitation hardening has a more profound effect on strength than observed in hardness test. The yield strength of the alloy is considerably higher in T8 temper condition than in T6. An important observation here is that, although the alloy AA6061 show comparable hardness value in T6 and T8 temper conditions, the alloy in T6 temper condition shows poor mechanical behaviour under quasi-static compressive loading.

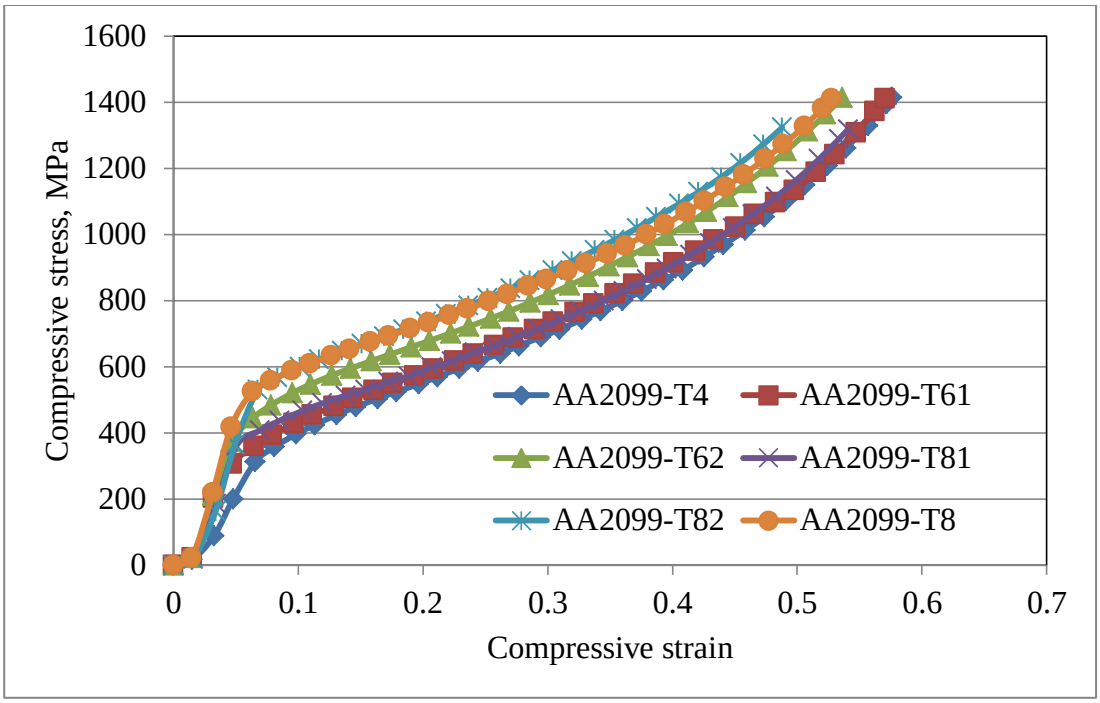

Figure 4.2. Typical stress-strain curves obtained for AA2099 aluminium alloys subjected to quasi-static compression test.

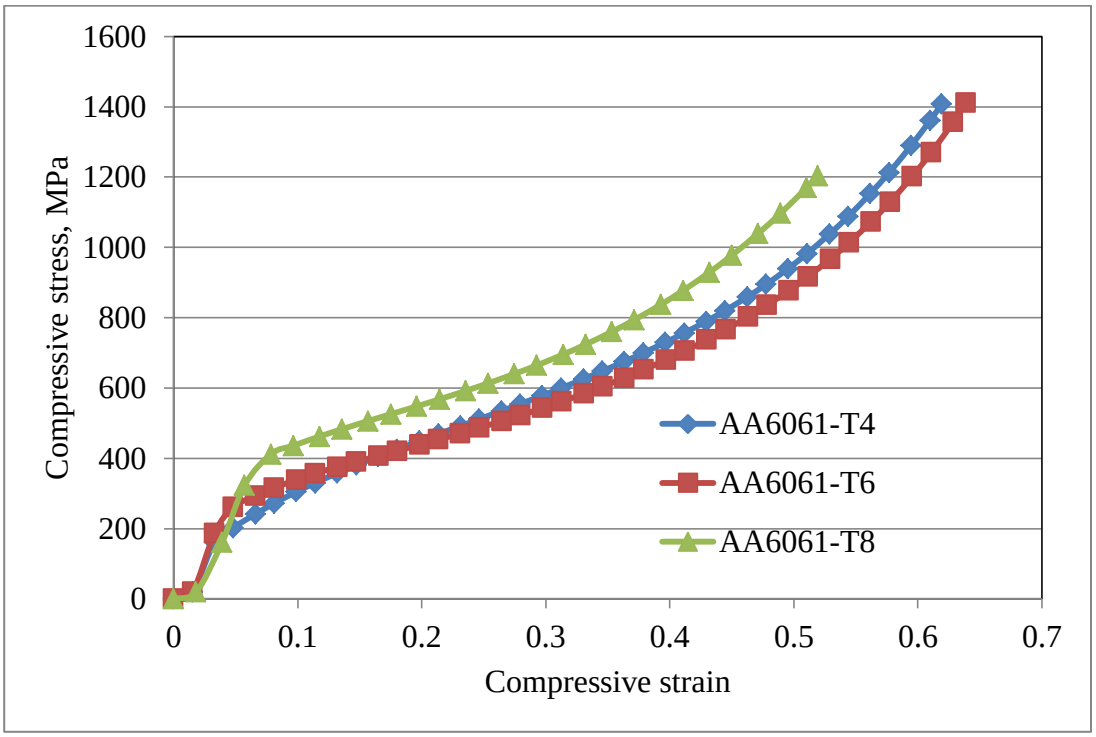

Figure 4.3. Typical stress-strain curves obtained for AA6061 aluminum alloy subjected to quasi-static compression test.

Table 4.1. Compressive yield strength and total strain (per 100 kN) of the investigated alloy obtained from quasi-static compression test.

Alloy	Yield Strength (MPa)	Total Strain (Per 100 KN)
AA2099-T4	360 ± 5	0.576
AA2099-T61	380 ± 5	0.571
AA2099-T62	460 ± 5	0.536
AA2099-T81	400 ± 5	0.541
AA2099-T82	560 ± 5	0.488
AA2099-T8	520 ± 5	0.528
AA6061-T4	174 ± 5	0.619
AA6061-T6	205 ± 5	0.639
AA6061-T8	406 ± 5	0.520

4.1.3 Precipitation Sequence of AA2099 and AA6061 Aluminum Alloys

As discussed in chapter three, the heat treatment of the alloys involves heating the alloys to the solution heat-temperature to form a single-phase supersaturated solid solution (SSS). The single phase supersaturated solid solution structure is retained in the alloys on quenching in water. This supersaturated solid solution contains vacancy-rich solute clusters. During artificial aging, second phase particles precipitate out of the supersaturated solid solution. As mentioned in section 3.2 of chapter three, a two-step process was used in the precipitation hardening of the AA2099 alloy while that of AA6061 is a one-step process.

During the first step aging, the AA2099 samples were heated to a temperature of 120 ºC. During this process, dissolution of the vacancy-rich solute clusters occur and Guinier-Preston (GP) zones are formed thereby causing an increase in strength. GP zones are the initial zones for the precipitates as they subsequently come out of solid solution. The GP zones are ordered solute-rich groups of atoms that are few atom planes thick and also coherent with the matrix. The strengthening associated with the coherency will be explained subsequently. During the second step aging, the AA2099

specimens are heated to a temperature of 160ºC, which is higher than that of the first step aging. During this process, the GP zones become unstable and transform to second phase particles depending on the various alloying elements. For example, in the two-step aging of Al-Zn-Mg [101], GP zones form when heated below 150 °C. At 150 °C, the GP Zones becomes unstable and then transform into semi-coherent η′ ($MgZn_2$) particle. As η′ particle coarsen, a more stable phase of η is formed. The sequence of the precipitation reaction is given in equation 4.1.

$$SSS \rightarrow Clusters \rightarrow GP\ Zones \rightarrow \eta' \rightarrow \eta \quad \text{.....(4.1)}$$

Al-Li-Cu-Mg system with high Copper and low Magnesium content such as AA2099 aluminum alloy contains homogeneously precipitated δ′ (Al_3Li) strengthening phase which remains coherent even after extensive aging [102,103]. The temperature – time graph for the heat treatment process for both AA2099 and AA6061 aluminium alloys investigated in this study are presented as Figures 3.2 and 3.3 in chapter 3. During artificial ageing, coarsening of δ′ particles with time leads to the formation of an equilibrium phase δ (AlLi) and the widening of the precipitate free zone (PFZ) as a result of solute dissolution in GP formation [104]. The δ (AlLi), being an intermetallic compound, precipitates along grain boundaries [104] at low ageing temperatures and in the matrix on dislocations at higher temperatures [105]. The sequence of precipitation reaction for the phase transformation reaction is given in equation 4.2.

$$SSS \rightarrow Clusters \rightarrow GP\ Zones \rightarrow \delta'(Al_3Li) \rightarrow \delta(AlLi) \quad \text{.....(4.2)}$$

When dispersoids (magnesium- and zirconium-containing phases) are introduced into binary Al-Li alloy, slip becomes homogenized [96,102,106]. The presence of copper and magnesium leads to the formation of semi-coherent precipitates. These precipitates also help in the slip homogenization [96,102,106]. Slip is defined as the plastic deformation that occurs due to dislocation motion. The dispersoids evenly spreads the precipitates and second phase particles throughout the microstructure thereby distributing dislocations evenly within the microstructure. All these additions help control recrystallization and hence, the grain size. They also lead to dense

co-precipitation of other phases such as T_1 (Al_2CuLi), T_2 (Al_6CuLi_3), θ′ (Al_2Cu), β′ (Al_3Zr) and S (Al_2CuMg) alongside δ′ phase during artificial aging. The exact phase(s) present in each Al-Li alloy vary depending on the alloy additions. The presence of copper in the Al-Li-Cu-Mg system such as the investigated AA2099 alloy helps reduce the solubility of lithium and then enhance the co-precipitation of other phases like GP zones, T_1 (Al_2CuLi) and θ′ (Al_2Cu) [1]. The precipitation however depends on the Cu/Li ratio. Low Cu/Li ratio is reported to favour the simultaneous precipitation of δ′ and T_1 phases [103,104,108]. δ′ is observed to form immediately after quenching which is then followed by θ′ and T_1 during the aging treatment [104,107]. T_1 being an equilibrium phase is observed to precipitate heterogeneously on dislocations few minutes into aging treatment. T_2 equilibrium phase has also been observed to either co-precipitate alongside T_1 or alone without T_1. The sequence of precipitation reaction leading to θ′ formation is given in equation 4.3 [96];

$$SSS \rightarrow Clusters \rightarrow GP\ Zones \rightarrow \theta'' \rightarrow \theta' \rightarrow \theta(Al_2Cu) \quad \text{.....(4.3)}$$

The presence of magnesium in the Al-Li-Cu-Mg alloy system also helps to reduce the solubility of lithium [96], enhances solid solution strengthening and also promotes the nucleation of homogeneously precipitated fine S′ phase on dislocation or sub-boundaries [96,104,107,109]. TEM analysis of AA2099 Al-Cu-Mg-Li alloy revealed homogeneous and dispersedly distributed partially coherent lathe-shape precipitate S′ (Al_2CuMg) and Spherical δ′ (Al_3Li) precipitates [110]. After addition of magnesium, the Guinier-Preston-Bagaryatsky (GPB) zones common to the Al-Cu-Mg alloy system are formed, leading to the precipitation of the S phase [111]. This GPB zone is known to form during high temperature aging and has a structure that is related to the cubic $Mg_2Al_5Cu_5$ [111]. The sequence of precipitation reaction leading to the formation of T_1, T_2 and S are shown in equation 4.4 to 4.6.

$$SSS_0 \rightarrow SSS_1 + \delta' \rightarrow SSS_2 + \delta' + T_1(Al_2CuLi) \quad \text{.....(4.4)}$$

$$SSS_0 \rightarrow SSS_1 + \delta' \rightarrow SSS_2 + \delta' + T_2(Al_6CuLi_3) \quad \text{.....(4.5)}$$

$$SSS_0 \rightarrow Clusters \rightarrow GPB\ Zones\ [111] \rightarrow S'' \rightarrow S' \rightarrow S\ (Al_2CuMg)\ \ldots\ldots\ldots\ldots\ldots\ldots(4.6)$$

In addition to Li, Cu and Mg, the investigated AA2099 alloy also contained zirconium. The presence of zirconium in Al-Li-Cu-Mg alloy system helps inhibit recrystallization through the precipitation of fine spherically coherent β′ (Al_3Zr) particles and also promote the decomposition of the supersaturated solid solution thereby leading to the formation of the metastable Li_2Al_3Zr phase [110]. Fendoni [98] suggested δ′ (Al_3Li), δ (AlLi), S′ (Al_2CuMg), T_1 (Al_2CuLi), T_2 (Al_6CuLi_3) and β′ (Al_3Zr) as the phases present in Al-Li-Cu-Mg alloy system containing high copper and low magnesium and zirconium with δ′ and T_1 being the major phases with high volume fraction and S′ and β′ being the minor phases with small volume fraction.

In Al-Si-Mg alloy system, the aging process involves the formation of independent clusters of Mg and Si atoms. These independent clusters lead to the formation of coherent co-clusters containing both Si and Mg. These coherent co-clusters further lead to the formation and growth of the semi-coherent β″ (Mg_5Si_6) strengthening phase [112-118]. As aging progresses, this strengthening phase decomposes into β′ ($Mg_{1.8}Si$) first and then finally to the incoherent equilibrium phase β (Mg_2Si) [114,116,118]. Silicon in various morphologies has been observed to also precipitate alongside β [114]. The sequence of precipitation reaction for β transformation is given below.

$$SSS \rightarrow Clusters \rightarrow GP\ Zones \rightarrow \beta'' \rightarrow \beta' \rightarrow \beta + Si\ \ldots\ldots\ldots\ldots\ldots\ldots\ldots\ldots\ldots\ldots\ldots\ldots(4.7)$$

During the aging process also, incoherent phases such as B′ ($Mg_9Al_3Si_7$), U1 ($MgAl_2Si_2$) and U2 (MgAlSi) are observed to precipitate after the β phase [112,115,117]. These incoherent phases are referred to as post-β phases. The addition of copper to the Al-Si-Mg alloy system leads to the formation of the Al-Si-Mg-Cu alloy system, of which the investigated AA6061 aluminum alloy is a prominent member. During the aging of this alloy, the incoherent equilibrium phase β (Mg_2Si) also precipitates in similarity to the Al-Si-Mg alloy system. However, the presence of copper in the Al-Si-Mg-Cu system brings about the precipitation of QP phase and θ (Al_2Cu) phase [113,119] alongside the β equilibrium phase and also modifies the relative amounts of Si

and β phase. These phases appear to be distinctively different from those precipitated during the artificial aging of the Al-Si-Mg alloy system. During cooling, QP phase first decompose to form QC which is situated on θ′ plate and then decomposes further to form Q stable phase [113,119] through the reaction given below.

$$QP \rightarrow QC \rightarrow Q' \rightarrow Q \quad \text{.....(4.8)}$$

The exact composition of the Q phase is unknown but has been suggested to be any of the following; $Al_5Cu_2Mg_8Si_6$, $Al_4CuMg_5Si_4$, $Al_4Cu_2Mg_8Si_7$ or $Al_3Cu_2Mg_9Si_7$ [115]. The transformation of θ′ to θ (Al_2Cu) phase is also observed during the precipitation process. The exact phases present in the Al-Si-Mg-Cu alloy system has been observed to be largely dependent on the Mg/Si ratio [113]. Mg/Si ratio greater than 1 has been observed to favour both the precipitation of Q, θ (Al_2Cu) and β (Mg_2Si) phases [113] and more nucleation of β″ on dislocations [112]. Mg/Si ratio less than 1 however favours the precipitation of Q, β (Mg_2Si) and Si. However, increasing the amount of copper also tend to promote the precipitation of θ (Al_2Cu) in favour of β (Mg_2Si). From the composition of AA6061 aluminum alloy used in this study, Mg/Si ratio is observed to be greater than 1. Thus, the expected phases present in the microstructure of AA6061aluminum alloy will be Q, θ (Al_2Cu) and β (Mg_2Si).

Generally, under quasi-static loading, AA2099 aluminum alloy showed more resistance to deformation compared to AA6061. This is due to the presence of lithium-containing phases in the microstructure [1]. This unique microstructure of Al-Li based alloys contain homogeneously precipitated δ’ (Al_3Li) strengthening phase which remains coherent even after extensive aging [102]. Dispersoid phases containing magnesium and zirconium as well as semi-coherent second phase particles such as T_1 (Al_2CuLi), θ’ (Al_2Cu) or S (Al_2LiMg) through copper or magnesium when introduced helps to homogenize slip [96,102,106]. These additions help control recrystallization and, hence, the grain size. This explains why AA2099 has better deformation resistance than AA6061 as observed in the hardness and compression tests.

During cold working, dislocations are generated. These dislocations act as nucleation sites for strengthening precipitates such as T_1 (Al_2CuLi) and S (Al_2LiMg) during precipitation hardening [10,102]. The second phase particles present in this alloy are as discussed earlier. Thus, strength increase in AA2099-T8 and AA2099-T82 under quasi-static loading condition is attributed to these fine precipitates rather than the change in dislocation density [120]. This means more strengthening precipitates will be present in T8, T81 and T82 temper conditions than in T4, T61 and T62 temper conditions. As explained above that T_1 nucleates on dislocations, No T_1 precipitate will formed in the matrix of non-cold worked samples but is formed at the grain boundaries. Any T_1 precipitate found in non-cold worked samples (T4, T61 and T62) are due to dislocations remaining after solution heat treatment [10]. This explains the high resistance to deformation of AA2099 in T8, T81 and T82 temper conditions compared to T61 and T62 temper conditions when subjected to quasi-static loading conditions.

Other strengthening second phase particles observed in other Al-Li alloys includes; T_2 (Al_6CuLi_3), Al_3Zr, and Guinier-Preston (GP) zones [10,100]. High aging temperatures and long aging time are known to promote the growth of large particles of precipitate [10,96]. As the coherent particles grow, misfits strain fields are generated between these particles and the host lattice. These misfit strains slow down dislocation motion. For dislocation to cut through these coherent particles, the applied stress must exceed that required to move dislocations through the matrix. Due to this high stress, the particles shear as dislocations cut through them [120]. When incoherent particles grow however, dislocations are unable to cut through the particles. Instead, the dislocations loop around individual particles. More energy is required for dislocation to cut through a coherent precipitates than loop around incoherent precipitates. As more dislocations loop around the particles however, the effective distance between adjacent particle decreases with each dislocation passage thereby resulting in increased strength for an alloy that is strengthened with incoherence precipitates.

Romios *et al*. [10] proposed that clustering of solute atom occurs during the first step aging while evenly distributed various sized precipitates form in the second step. The aging treatment is based on the principle that low temperatures favours nucleation of

strengthening precipitates while high temperatures favour the growth of such precipitates [10]. Both AA2099 and AA6061 alloys are not over-aged during precipitation hardening within the considered aging temperatures and times. Brooks [96] reported that typical Al-Li alloys and AA6061 alloy are peak-aged at similar aging conditions. Because over-aging never occurred, the more particles in T82 compared to T81 leads to a much higher strength thereby increasing the deformation resistance. This also explains the increased deformation resistance in T62 compared to T61. The aging time, aging temperature, type, volume fraction, size and distribution of the second phase particles are affected by the original structure of the alloy [96]. A study on the heat treatment of Al-Mg-Si-Cu alloys reveals that the AA6061 aluminum alloy is peak-aged during the artificial aging process.

4.2 Dynamic Mechanical Tests

In dynamic mechanical test, direct impact compression test and dynamic torsion test were carried out on the two alloys in T4, T6 and T8 temper conditions.

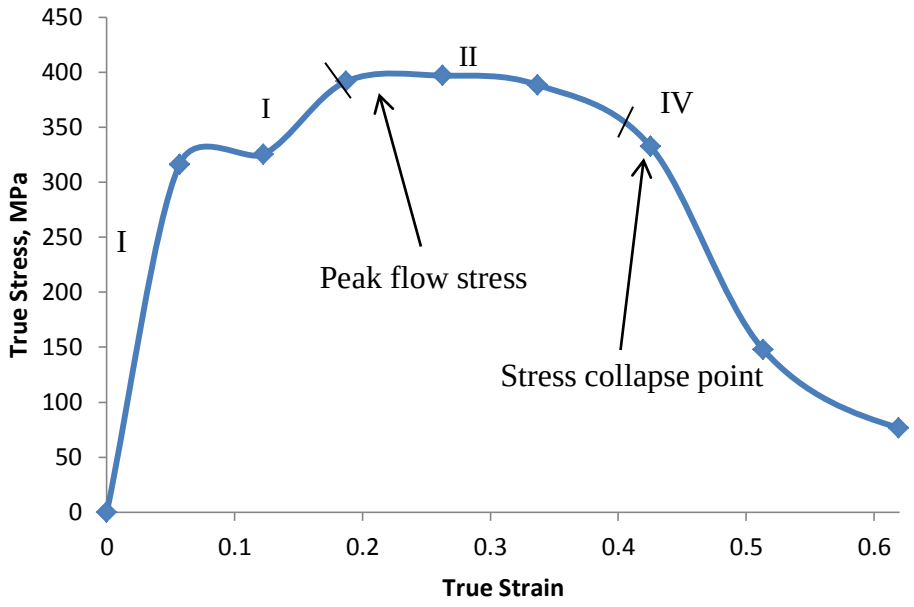

Figure 4.4. Dynamic stress-strain Curve for 2099-T82 impacted at 33 kg m s^{-1}.

Figure 4.4 shows a typical dynamic stress-strain curve of AA2099-T82 generated from a direct impact compression test. During impact, about 90% of the projectile's kinetic energy is converted into heat which causes thermal softening of the impacted specimen. Thus, both thermal softening and strain hardening occur simultaneously in the specimen as it deforms under the impact loading. Deformation of the alloy proceeds in four stages. In stage I, deformation is elastic while in stages II – IV, it is plastic. In stage II, strain hardening dominates the plastic deformation process up to the point of peak flow stress. The yield point is clearly visible unlike the case of quasi-static loading condition. Beyond this point of peak flow stress (stage III), thermal softening begins to dominate the plastic deformation process leading to decrease in flow stress as strain increases further. In stage IV, a condition of adiabatic heating occurs and the flow stress collapses as a result of excessive thermal softening in the adiabatically heated region. The stress collapse is a consequence of the thermo-mechanical instability inside the shear band.

4.2.1 Direct Impact Test

Direct Impact Test for AA2099 aluminum alloy

Figures 4.5 to 4.7 show the dynamic stress-strain curves of AA2099 aluminum alloy in T4, T61 and T62 temper conditions as a function of the impact momentum and strain rates. The higher the impact momentum, the higher is the strain rate. The strain rate corresponding to an impact momentum depends on the temper condition of the aluminum alloy. In T4 temper condition, peak flow stress and strain rates increased with increasing impact momentum. At impact momentum of 28 kg m s^{-1}, peak flow stress value of 316 MPa was recorded. As impact momentum increased to 39 kg m s^{-1}, peak flow stress also increased to 381 MPa. No drop in peak flow stress was observed with increasing impact momentum. In T61 temper condition, maximum flow stress value of 350 MPa is recorded at 28 kg m s^{-1} impact momentum. As impact momentum increased to 39 kg m s^{-1}, peak flow stress also increased to 378 MPa. No drop in peak flow stress was observed. In T62 temper condition, peak flow stress value of 380 MPa is recorded both at 28 and 31 kg m s^{-1} impact momentums. Increasing the impact momentum to 39 kg m s^{-1} increases the peak flow stress value to 415 MPa. It can be

observed in T4, T61 and T62 temper conditions that as strain rate increases, the peak flow stress increases with increasing impact momentum.

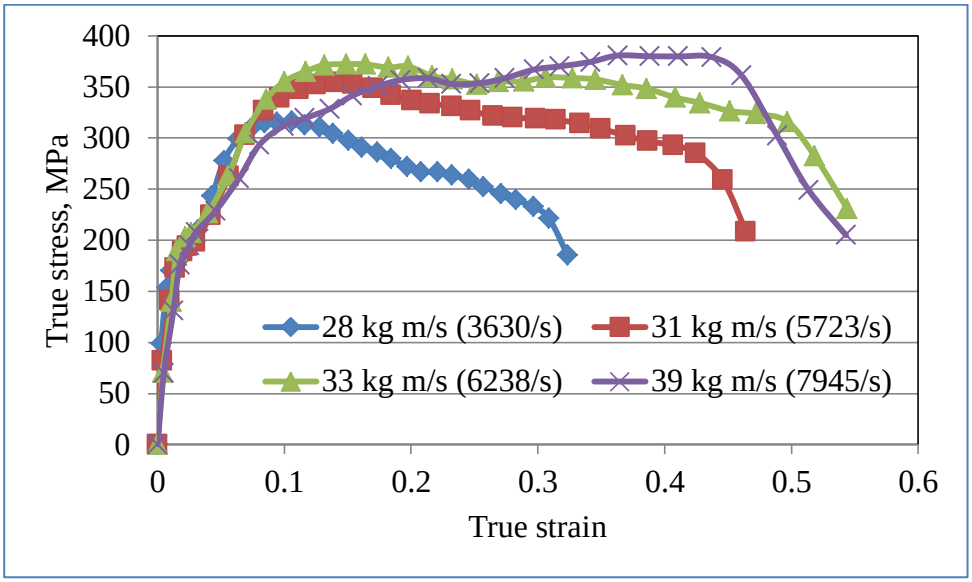

Figure 4.5. Dynamic stress-strain curves for AA2099-T4 alloy as a function of impact momentum and strain rate.

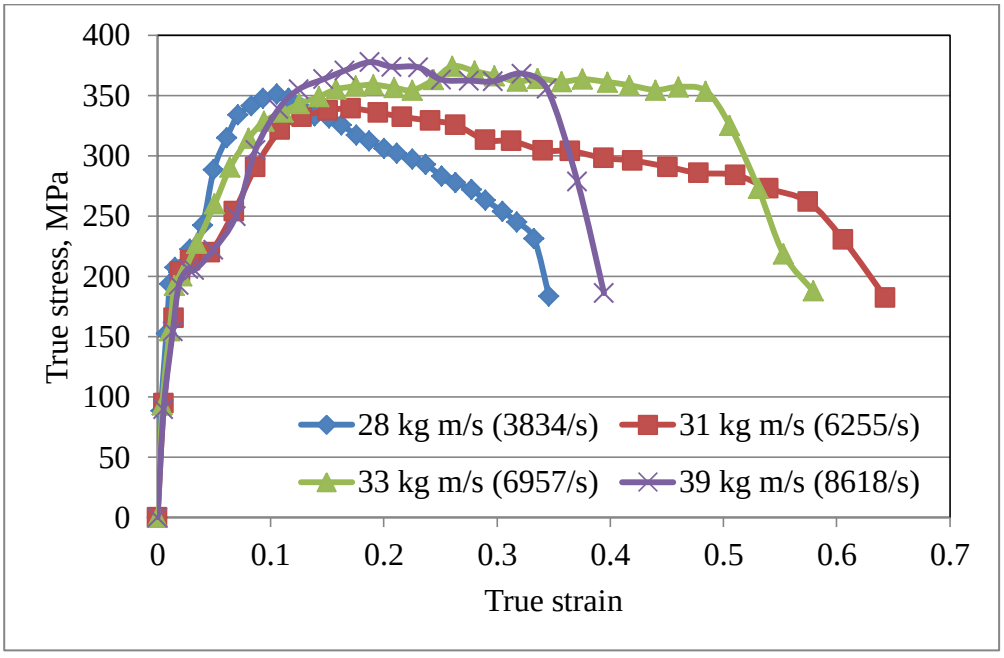

Figure 4.6. Dynamic stress-strain curves for AA2099-T61 alloy as a function of impact momentum and strain rate.

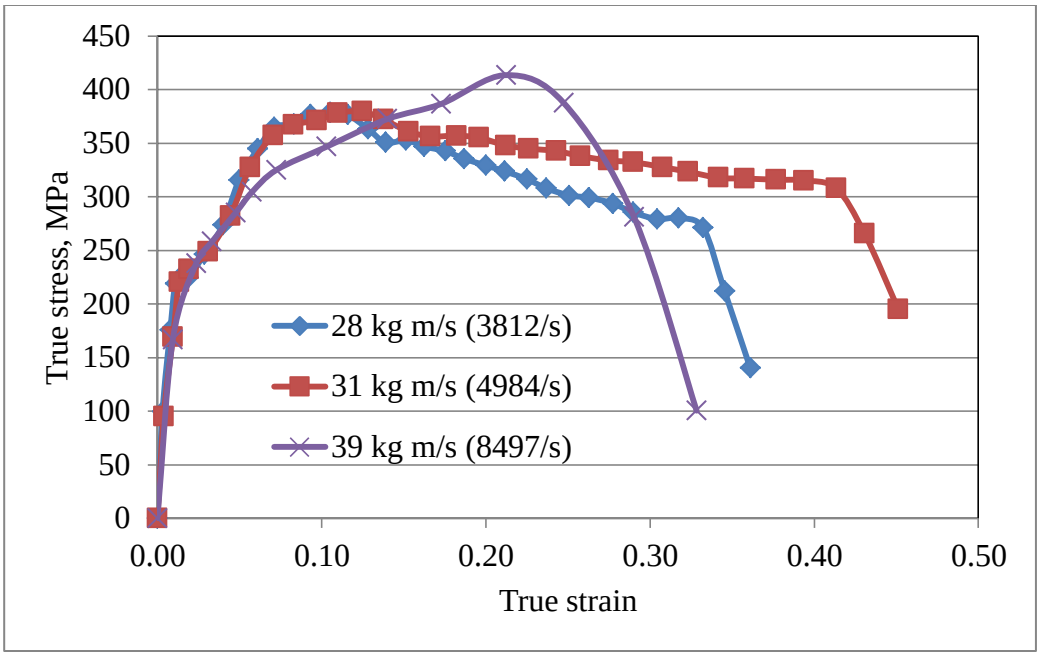

Figure 4.7. Dynamic stress-strain curves for AA2099-T62 alloy as a function of impact momentum and strain rate.

Figures 4.8 to 4.10 show the dynamic stress-strain curves of AA2099 aluminum alloy in T81, T82 and T8 temper conditions. In T81 temper condition, peak flow stress value of 300 MPa was recorded at 28 kg m s^{-1} impact momentum. Increasing impact momentum to 31 kg m s^{-1} leads to increase in peak flow stress up to 410 MPa. However, further increase in the impact momentum leads to drop in peak flow stress. In T82 temper condition, a peak flow stress of 420 MPa was recorded at 28 kg m s^{-1} impact momentum. This further increased to 450 MPa at 33 kg m s^{-1} impact momentum. Beyond this impact momentum, peak flow stress dropped slightly to 440 MPa at 39 kg m s^{-1} impact momentum. In as received condition (T8), peak flow stress of 375 MPa is recorded at 28 kg m s^{-1} impact momentum. This slightly increased to 390 MPa at 31 kg m s^{-1} but then decreased beyond this point. The early drop in the peak flow stress of T81, T82 and T8 temper conditions is an indication of a more intense adiabatic heating. During this process, the deformation becomes so rapid that little strain hardening is allowed to take place. According to equations 2.1 and 2.2 from chapter two of this report, increasing stress increases the temperature inside the shear band and hence, increases the tendency for thermal softening. This explains the observed peak stress

drop in T81, T82 and T8 temper conditions as the impact momentum was increased beyond 31 kg m s^{-1}. The drop in peak flow stress as impact momentum increases beyond 31 kg m s^{-1} indicate higher susceptibility in this alloy in T8 temper condition than T4 or T6 temper condition.

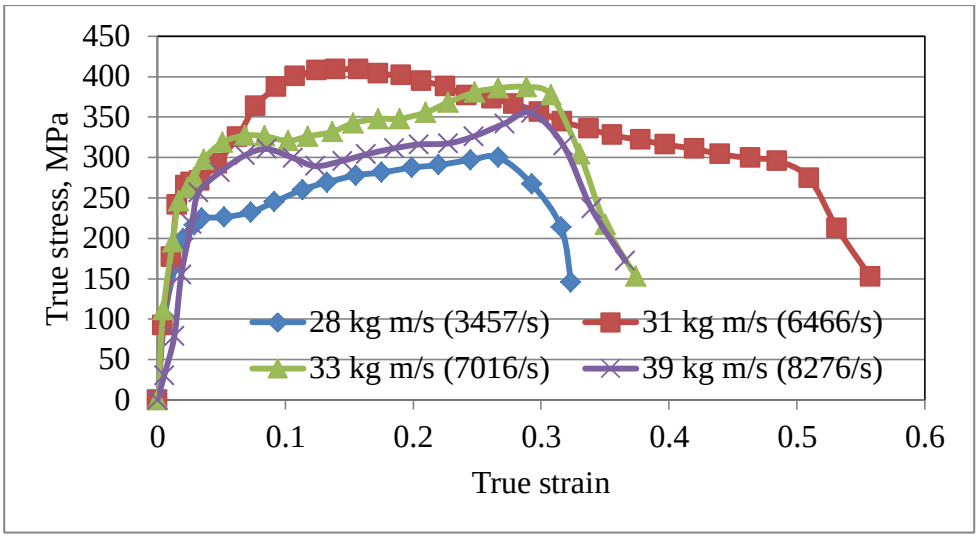

Figure 4.8. Dynamic stress-strain curves for AA2099-T81 alloy as a function of impact momentum and strain rate.

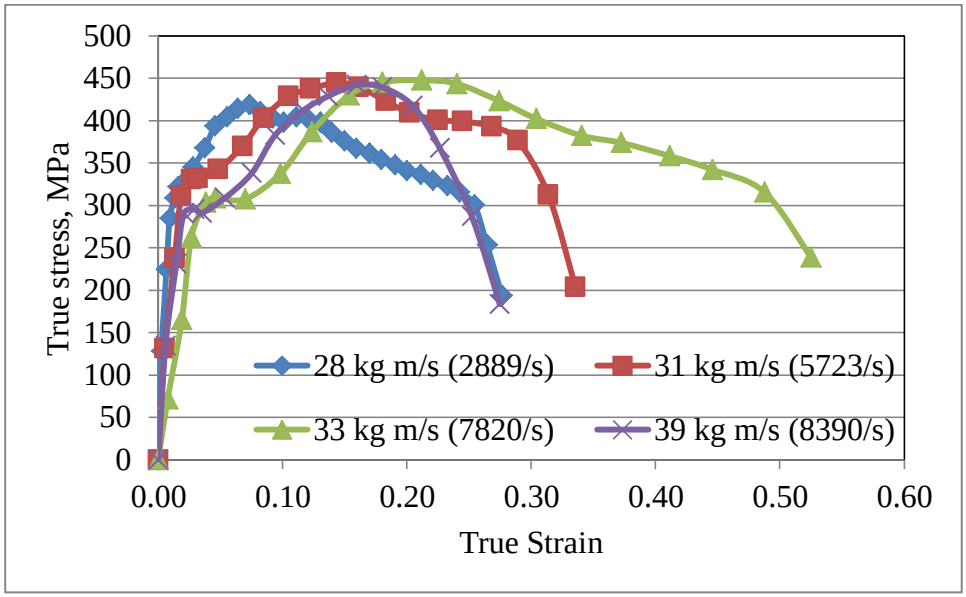

Figure 4.9. Dynamic stress-strain curves for AA2099-T82 alloy as a function of impact momentum and strain rate.

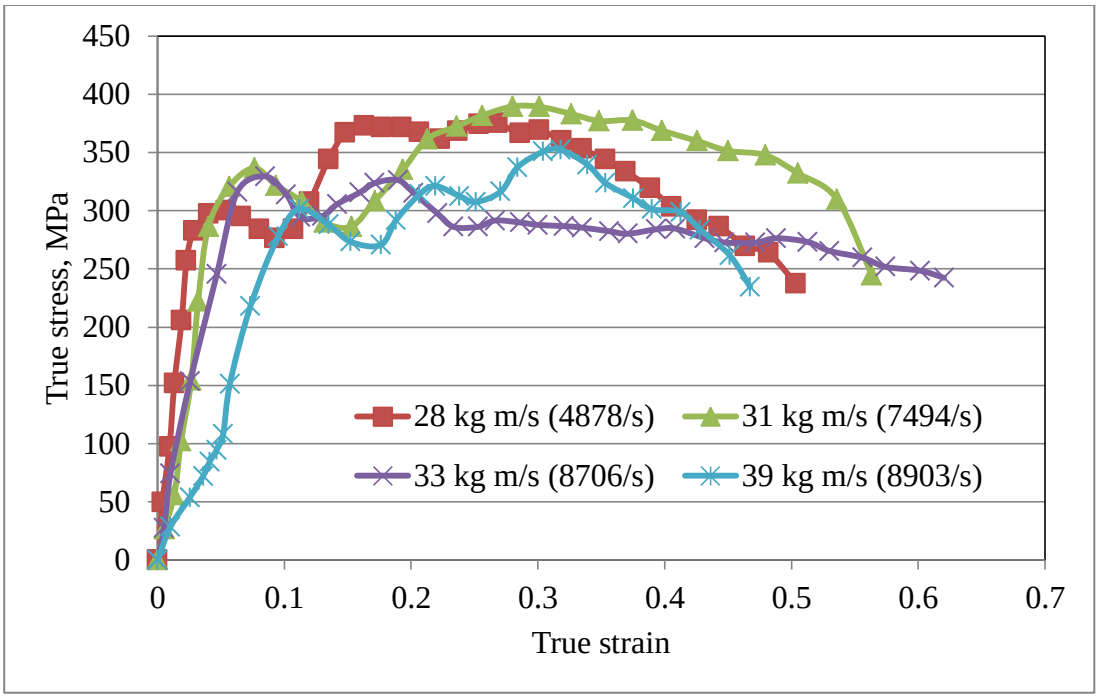

Figure 4.10. Dynamic stress-strain curves for AA2099-T8 alloy as a function of impact momentum and strain rate.

In order to compare the dynamic mechanical response of the AA2099 aluminum alloy in various temper condition, the strain rates and engineering strains associated with each alloy are compared at a single impact momentum of 33 kg m s^{-1} in Table 4.2. It can be inferred that high strain rates and engineering strain values indicate a high deformation resistance. AA2099-T8 appears to have both the highest strain rate and engineering strain values. This means AA2099 in T8 temper condition has the lowest resistance to deformation under dynamic impact loading. The presence of strains due to cold work introduced perturbations which lead to local adiabatic heating and stress collapse. Perturbation refers to a state of disturbance experienced by the alloy due to factors such as change in stress, strain, geometry, etc. Similar levels of engineering strain and strain rate are observed between T61 and T81 as well as T62 and T82. This means cold work has little additional effect on the strength of the alloys under dynamic impact loading. However, low engineering strain and strain rate recorded in the one-step aged alloy (T61 or T81) compared to their double step aged counterparts (T62 or T82) means the second step aging has no effect on the strength of the alloys under dynamic impact loading. The lowest engineering strain and strain rate recorded in AA2099-T4 showed that it has the

highest resistance to deformation under dynamic impact loading. In general, thermal softening, adiabatic heating and strain localization all play dominant roles on the dynamic mechanical response on AA2099 aluminum alloy under dynamic impact loading.

Table 4.2. Total engineering strain and strain rate of AA2099 alloys impacted at 33 kg m s^{-1}.

Alloy	Total Engineering Strain	Strain rate, s^{-1}
AA2099-T4	0.544	6238
AA2099-T61	0.607	6957
AA2099-T62	0.678	7773
AA2099-T81	0.612	7016
AA2099-T82	0.683	7820
AA2099-T8	0.7598	8706

Direct Impact Test for AA6061 aluminum alloy

Figures 4.11 to 4.13 show the dynamic stress strain curves for AA6061 aluminum alloys. In T4 temper condition, peak flow stress of 396 MPa occurred at 33 kg m s^{-1} impact momentum. Increasing impact momentum to 39 kg.m/s increases the peak flow stress to 560 MPa. Beyond 39 kg m s^{-1} impact momentum, a drop in peak flow stress to 336 MPa is observed at 44 kg m s^{-1} impact momentum. Similarly in T6 temper condition, peak flow stress of 432 MPa was recorded at 33 kg m s^{-1} momentum. Further increase to 39 kg m s^{-1} momentum increases the peak flow stress to 571 MPa. Beyond this momentum, peak flow stress drops to 339 MPa at 44 kg m s^{-1} momentum. This trend is however not followed in T8 temper condition. Increase in momentum leads to increase in peak flow stress. No drop in peak flow stress value was observed. At 33 kg m s^{-1} momentum, peak flow stress was observed to be 401 MPa. Increasing momentum to 44 kg m s^{-1} leads to increase in the peak flow stress to 502 MPa.

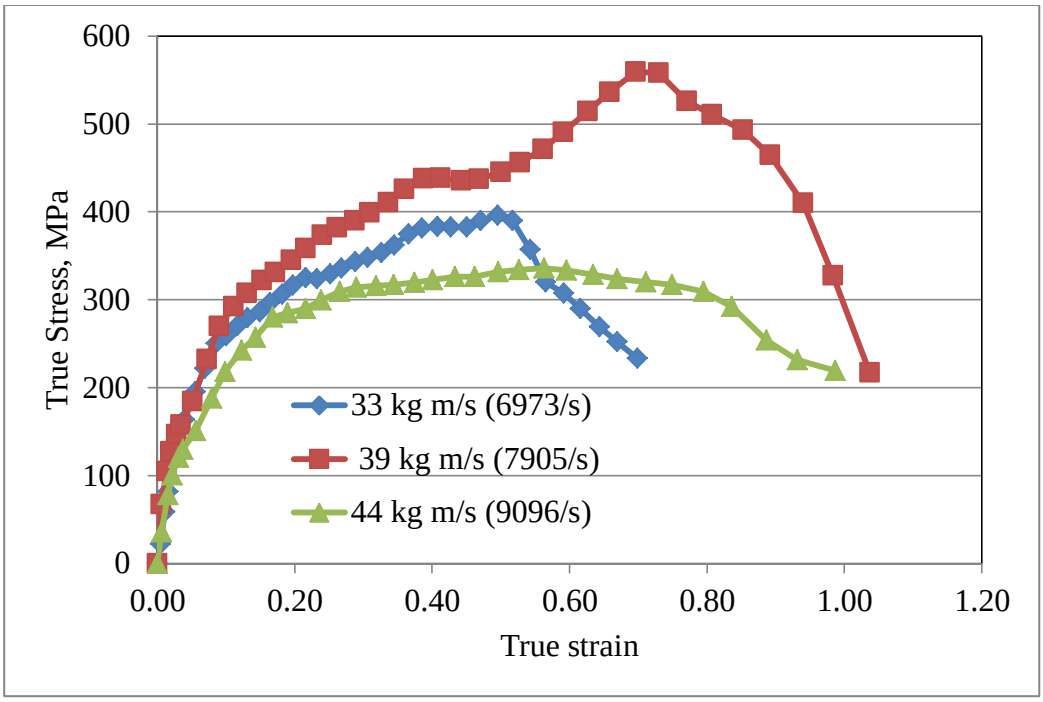

Figure 4.11. Dynamic stress-strain curves for AA6061-T4 alloy as a function of impact momentum and strain rate.

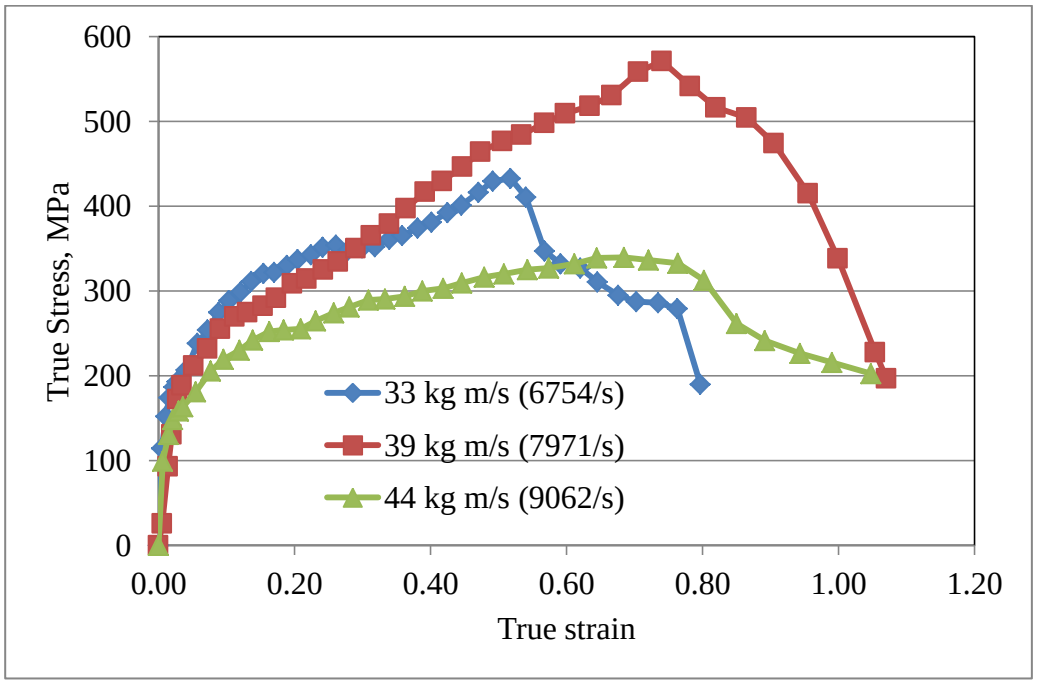

Figure 4.12. Dynamic stress-strain curves for AA6061-T6 alloy as a function of impact momentum and strain rate.

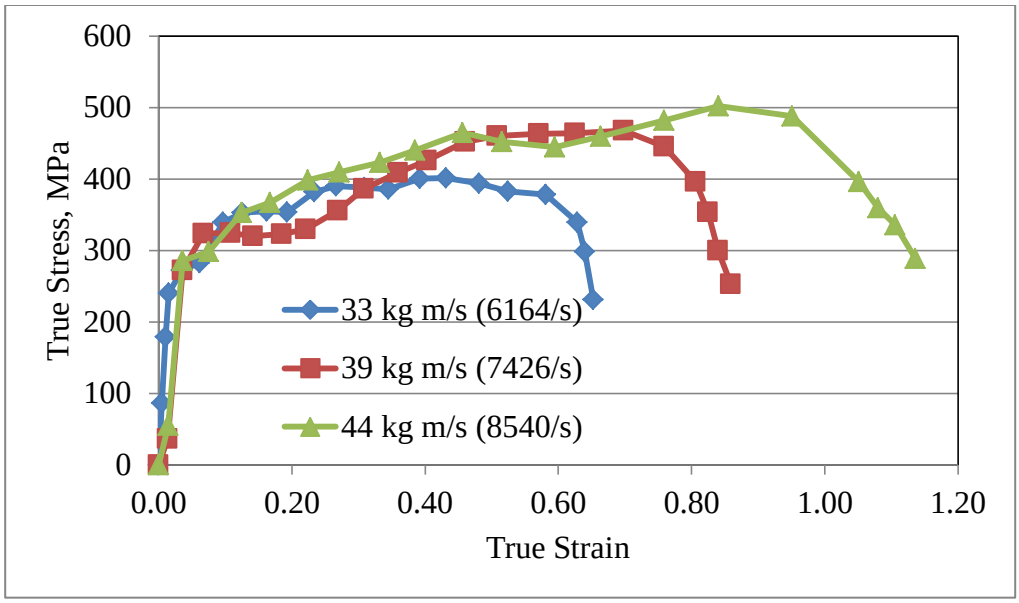

Figure 4.13. Dynamic stress-strain curves for AA6061-T8 alloy as a function of impact momentum and strain rate.

To also fully understand the response of these AA6061 alloys, comparisons using strain rates and engineering strains associated with each alloy are made at a single impact momentum of 33 kg m s^{-1} in Table 4.4. As previously explained, the high strain rates and engineering strain values also indicate a high deformation resistance in AA6061 aluminum alloy. The highest strain rate and engineering strain were achieved in AA6061-T4. This indicates low deformation resistance. AA2099-T4 was observed to behave in an opposite manner. Low strain rate and engineering strain achieved in AA6061-T6 compared to AA6061-T4 indicates that the precipitation hardening process has effect on the strength of the alloy under dynamic impact loading. This means AA6061-T6 is more resistant to deformation than AA6061-T4 under dynamic impact test. The combined effect of strain hardening and precipitation hardening tend to further lower the strain rate and engineering strain values. This is observed in the case of AA6061-T8 which showed more resistance to deformation under dynamic impact loading. The low engineering strains and strain rates recorded in AA6061 compared to AA2099 show that AA6061 aluminum alloy is more resistant to deformation under dynamic impact loading. This is a reverse of what was observed under quasi-static

loading. Experimental data sheet showing strain rate, total engineering strain and the deformation mode for investigated impact momentum range is presented in Table 4.3.

Table 4.3: Experimental Data sheet for direct impact test.

Material	Impact momentum, kg m s^{-1}	Engineering strain	Peak flow stress, MPa	Strain rate, s^{-1}	ASB
AA2099-T4	28	0.3168	315	3630	None
	31	0.4995	350	5723	None
	33	0.5444	372	6238	Heavily Deformed
	39	0.6934	380	7945	Faint Transformed
AA2099-T61	28	0.3346	350	3834	Slightly Deformed
	31	0.5459	340	6255	Faint Transformed
	33	0.6072	375	6957	Faint Transformed
	39	0.7521	378	8618	Faint Transformed
AA2099-T62	28	0.3327	378	3812	Heavily Deformed
	31	0.4350	380	4984	Heavily Deformed
	33	0.6784	330	7773	Heavily Deformed/Heavily Transformed
	39	0.7416	410	8497	Fully Transformed
AA2099-T81	28	0.3017	300	3457	Slightly Deformed
	31	0.5643	410	6466	Faint Transformed
	33	0.6123	390	7016	Faint Transformed
	39	0.7223	360	8276	Heavily Deformed/Faintly Transformed
AA2099-T82	28	0.2521	420	2889	Partially Transformed
	31	0.4995	445	5723	Fully Transformed
	33	0.6825	448	7820	Fully Transformed
	39	0.7322	442	8390	Fully Transformed

Material	Impact momentum, kg m s^{-1}	Engineering strain	Peak flow stress, MPa	Strain rate, s^{-1}	ASB
AA2099-T8	28	0.4257	373	4878	Fully Transformed
	31	0.6540	390	7494	Fully Transformed
	33	0.7598	330	8706	Fully Transformed
	39	0.7770	350	8903	Fully Transformed
AA6061-T4	33	0.6086	390	6973	Partially Transformed
	39	0.6899	560	7905	Fully Transformed
	44	0.7939	336	9096	Fully Transformed
AA6061-T6	33	0.5895	430	6754	Fully Deformed
	39	0.6957	571	7971	Fully Deformed/Fully Transformed
	44	0.7909	336	9062	Fully Transformed
AA6061-T8	33	0.5380	401	6164	Slightly Deformed
	39	0.6481	482	7426	Fully Transformed
	44	0.7453	502	8540	Fully Transformed

Table 4.4. Total engineering strain and strain rate of AA6061 alloys impacted at 33 kg m s^{-1}.

Alloy	Total Engineering Strain	Strain rate, s^{-1}
AA6061-T4	0.609	6973
AA6061-T6	0.590	6754
AA6061-T8	0.538	6164

4.2.2 Dynamic torsion Test

Figures 4.14 to 4.16 show the stress-strain curves of AA2099-T6, AA2099-T8 and 6061-T6 aluminum alloys as function of the applied torque. The torque was applied suddenly to enable rapid deformation of the thin-walled specimen. In AA2099-T6, peak flow stress of 153 MPa was observed for applied torque of 259 N m. Increasing the torque to 302 N m resulted in increase in the peak flow stress to 245 MPa. On increasing the applied torque beyond 302 N m, the peak flow stress dropped to 238 MPa at a torque of 345 N m. In AA2099-T8, a torque of 173 N m generated a peak flow stress value of 350 MPa. Increasing the torque to 216 N m increased the peak flow stress to 368 MPa. Beyond 216 N m, a drop in peak flow stress occurred. At 259 N m, peak flow stress dropped to 353 MPa. In AA6061-T6, peak flow stress of 247 MPa was generated at 173 N m torque. At a torque of 259 N m, peak flow stress was 269 MPa. At a torque of 302 N m, peak flow stress was 285 MPa. Beyond 302 N m, peak flow stress dropped slightly to 283 MPa at 345 N m. The reduction in peak flow stress with increasing torsional loading at high values of applied torque can be attributed to increased thermal softening over strain hardening during plastic deformation as the magnitude of the applied torque increases.

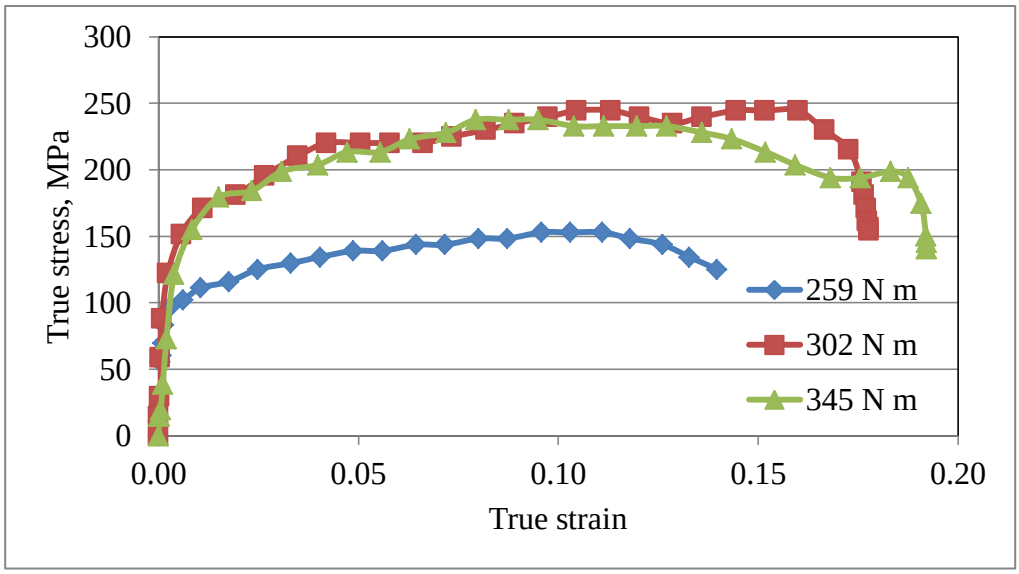

Figure 4.14. Dynamic stress-strain curves for AA2099-T6 alloy in torsion as a function of the applied torque.

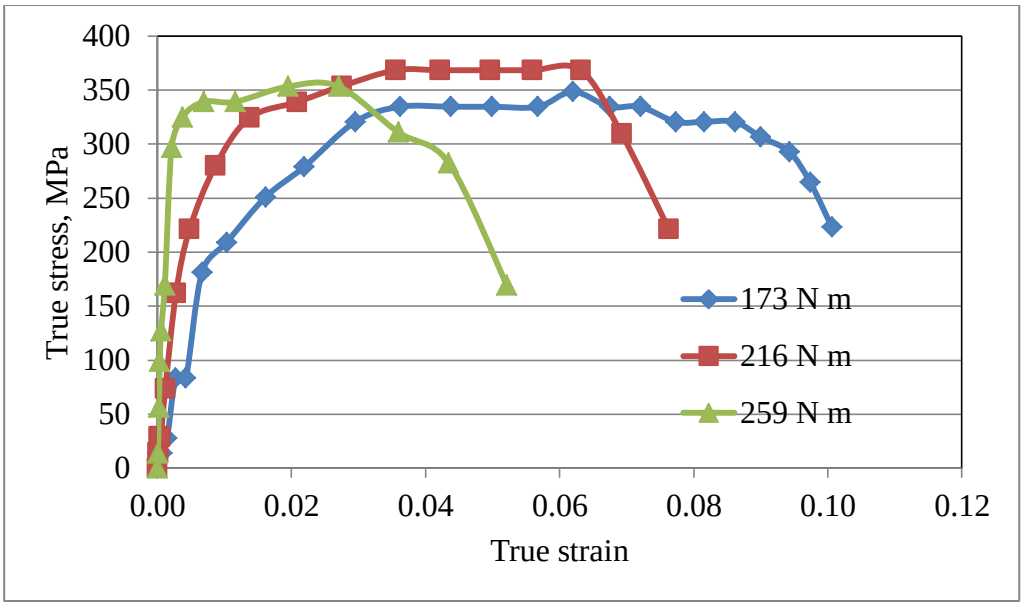

Figure 4.15. Dynamic stress-strain curves for AA2099-T8 alloy in torsion as a function of the applied torque.

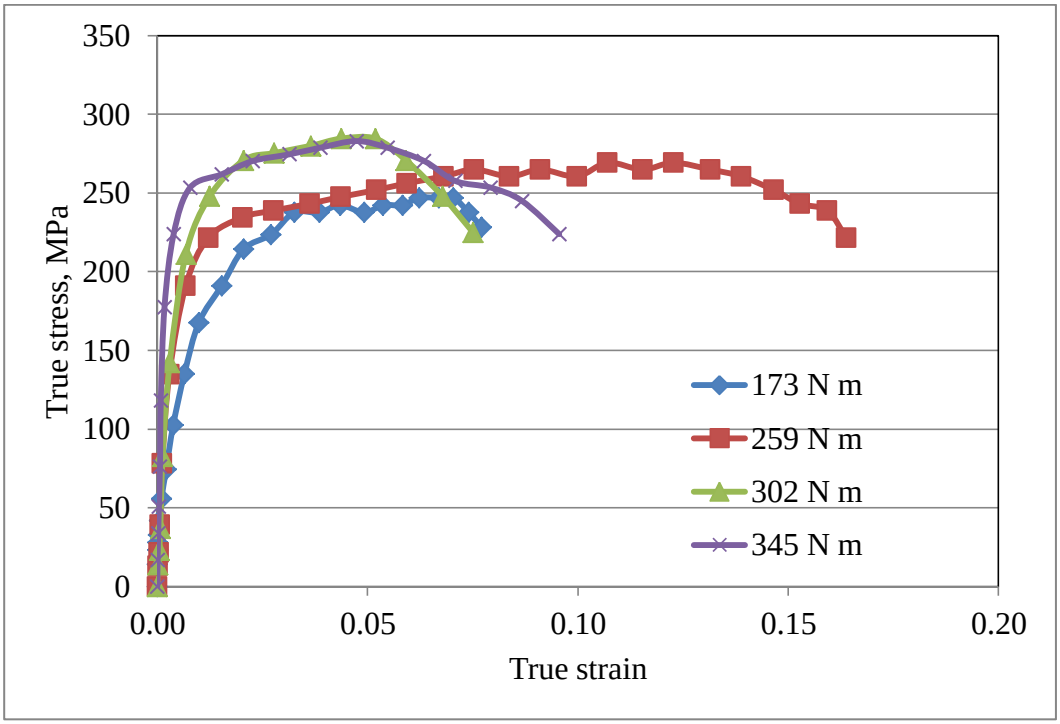

Figure 4.16. Dynamic stress-strain curves for AA6061-T6 alloy in torsion as a function of the applied torque.

In order to compare the behaviour of the alloys under high strain-rate loading in torsion, responses are studied as a function of applied torque generating the peak flow stress and peak flow stress itself as shown in Table 4.5. In AA2099-T6, an applied torque of 302 N m generated a peak flow stress of 250 MPa. In AA2099-T8 however, it took a lower applied torque of 216 N m to generate a peak flow stress of 370 MPa. This means more torque is needed to deform the AA2099 aluminum alloy in T6 temper condition than in T8. This means strain hardening has no effect on the response of AA2099 aluminum alloy under torsional loading at high strain rates. In AA6061-T6, a much higher applied torque of 345 N m is needed to generate a peak flow stress of 291 MPa. This means AA6061 has more deformation resistance than AA2099 under dynamic torsional loading. This result is in line with that of the dynamic impact test. In summary, AA2099 aluminum alloy show less resistance to deformation than AA6061 under dynamic mechanical loading at high strain rates. Reverse is however the case when the alloys are deformed under quasi-static loading.

Table 4.5. Peak flow stress and the applied torque values generating the peak flow stress in AA2099 and AA6061 aluminum alloys.

Sample	**Applied torque generating peak flow stress, N m**	**Peak flow stress, MPa**
2099-T6	302	250
2099-T8	216	370
6061-T6	345	291

4.3 Microstructural Analysis

4.3.1 Microstructure of heat treated samples before impact

4.3.1.1 AA2099 aluminum alloys

Optical microscopic examinations of all AA2099 aluminum alloy in T4, T61, T62, T81, T82 and T8 temper conditions reveal elongated grain structure. Second phase particles can be clearly seen within the microstructure. Scanning electron microscopic examination using secondary electron imaging technique is further carried out to provide more detailed information about the second phase particles that are not obtainable in the optical micrographs. The precipitated phases in present in AA2099 aluminum alloy as discussed previously in section 4.1.3 are suggested to be δ′ (Al_3Li), S′ (Al_2CuMg), β′ (Al_3Zr), δ (AlLi), T_1 (Al_2CuLi) and T_2 (Al_6CuLi_3). The coherent phases are δ′ (Al_3Li), δ (AlLi) and β′ (Al_3Zr) while S′ (Al_2CuMg), T_1 (Al_2CuLi) and T_2 (Al_6CuLi_3) are either semi-coherent or incoherent phases. For the coherent particles, the alloy becomes strengthened when dislocations cut through the particles usually at high stresses. For incoherent particles, dislocations loop around the particles and the effective distance between adjacent particle decreases with each dislocation passage, thereby resulting in increased strength.

Optical microscopic examination of AA2099-T4 reveals the elongated grain structure as well as spherically shaped second phase particles (Fig 4.17a). The particles appear to be more sparsely distributed in the microstructure compared to other temper condition and they appear in various sizes. Using secondary electron images technique, these spherically shaped second phase particles and few irregularly shaped particles can also be seen can be seen clearly (Fig 4.17b). The sparse distribution of second phase particles means fewer second phase particles are precipitated during natural aging. This explains the low deformation resistance under quasi-static loading conditions. The presence of these particles means that they were either present after the solution heat treatment or they may have precipitated out of the super saturated solid solution over time during natural aging.

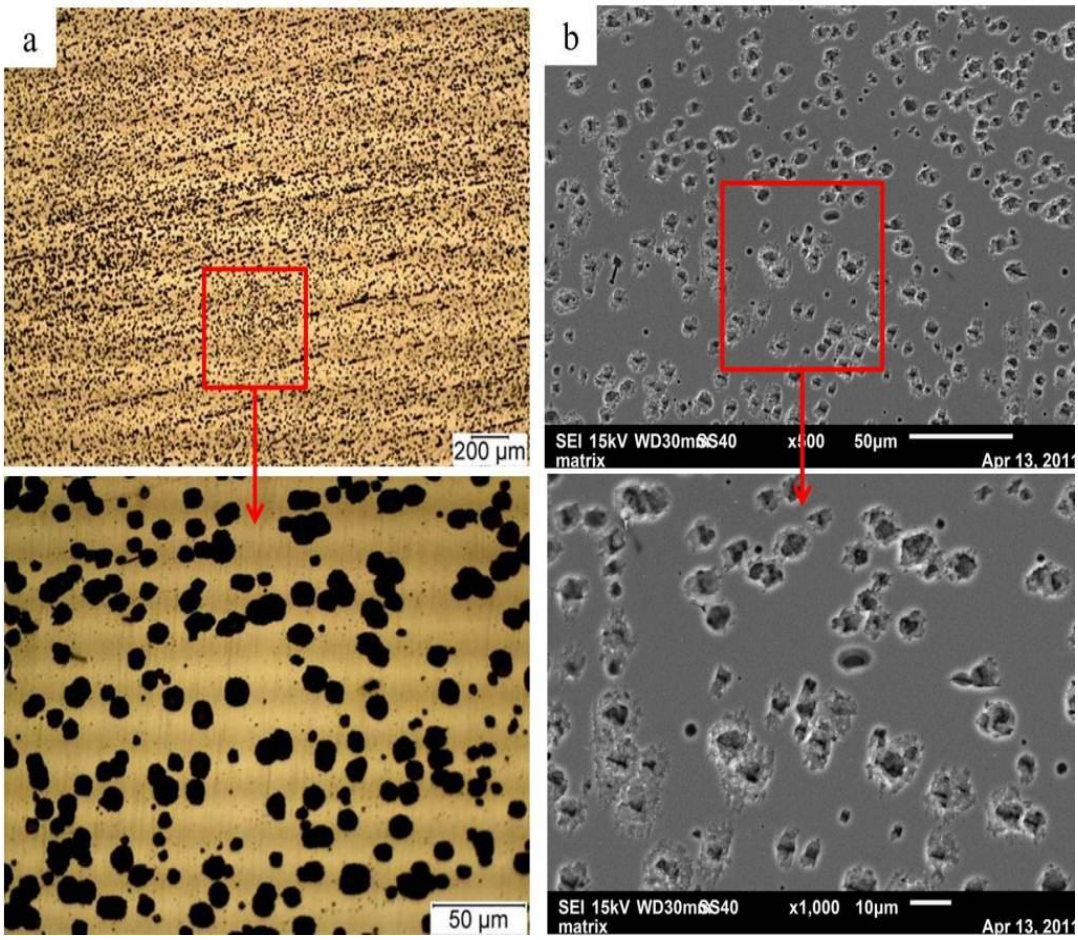

Figure 4.17. (a) Optical and (b) SEM micrographs of the aluminum AA2099-T4 alloy showing elongated grain structure and second phase particles.

Optical micrograph of the AA2099-T61 (Fig 4.18a) alloy suggests that it contains more irregularly shaped second phase particles compared to AA2099-T4. These irregularly shaped second phase particles occur in different sizes, shape and distribution. Using scanning electron microscopic imaging technique, some of these second phase particles are however observed to be spherically shaped. The colour contrast helps reveals the differences in these particles (Fig 4.18b). A few tiny white particles that were not visible in the optical micrograph can also be observed. These tiny particles in T61 temper condition accounts for the increase in strength under quasi-static loading compared to T4. These particles appear in AA2099-T61 because artificial aging favours the precipitation of more second phase particles. Optical and scanning electron micrographs of AA2099-T62 (Fig 4.19) however show the particles to be coarser and more uniformly

dispersed than those observed in AA2099-T61. This growth of second phase particles occurred during the second step aging. The secondary electron image further reveals more precipitation of the tiny white particles which is also uniformly dispersed within the microstructure. This is in agreement with the submission of Romios *et al.* [10] that clustering of solute atom occurs during the first step aging while evenly distributed various sized precipitates form in the second step. Due to the absence of cold work, dislocations are thereby not generated in T4, T61 and T62 temper conditions. This means T_1 strengthening phase will be absent in these specimens but they will contain few S strengthening phases.

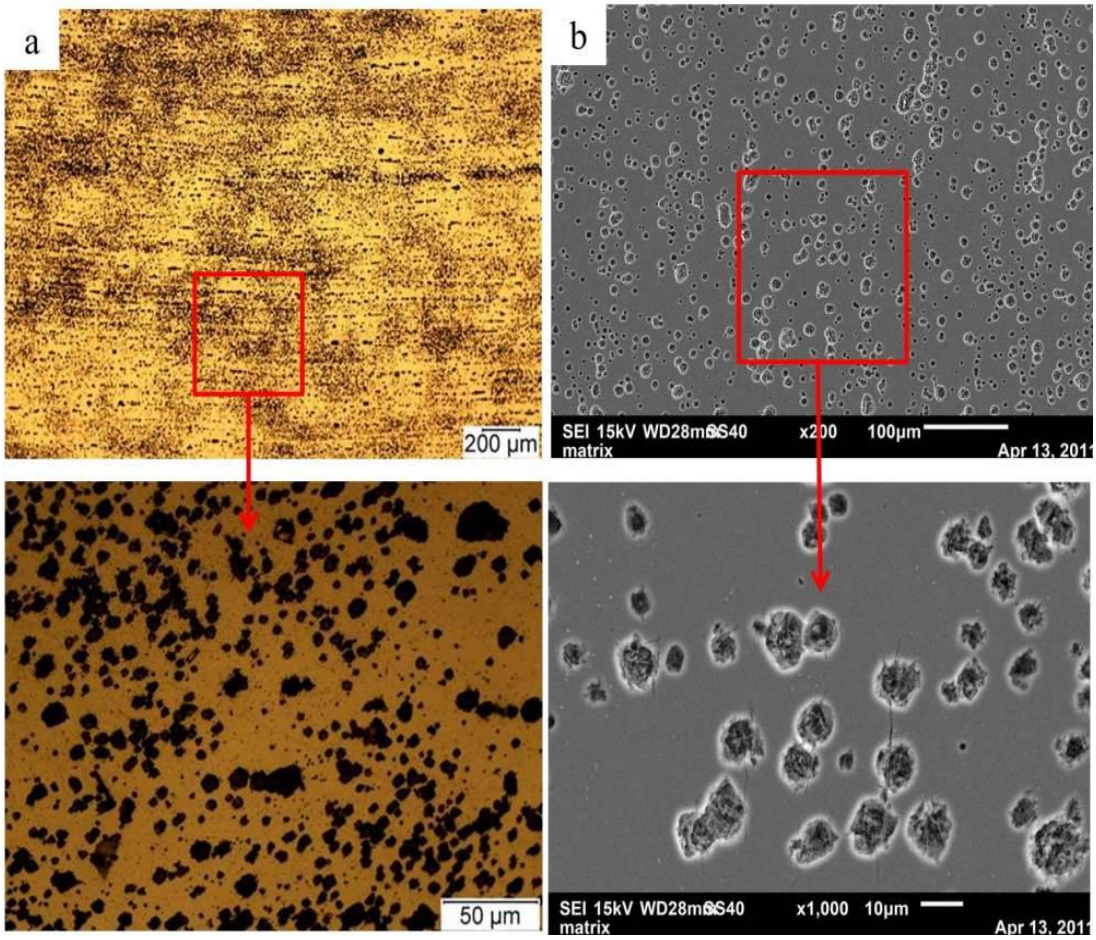

Figure 4.18. (a) Optical and (b) SEM micrographs of AA2099-T61 alloy showing elongated grain structure and second phase particles.

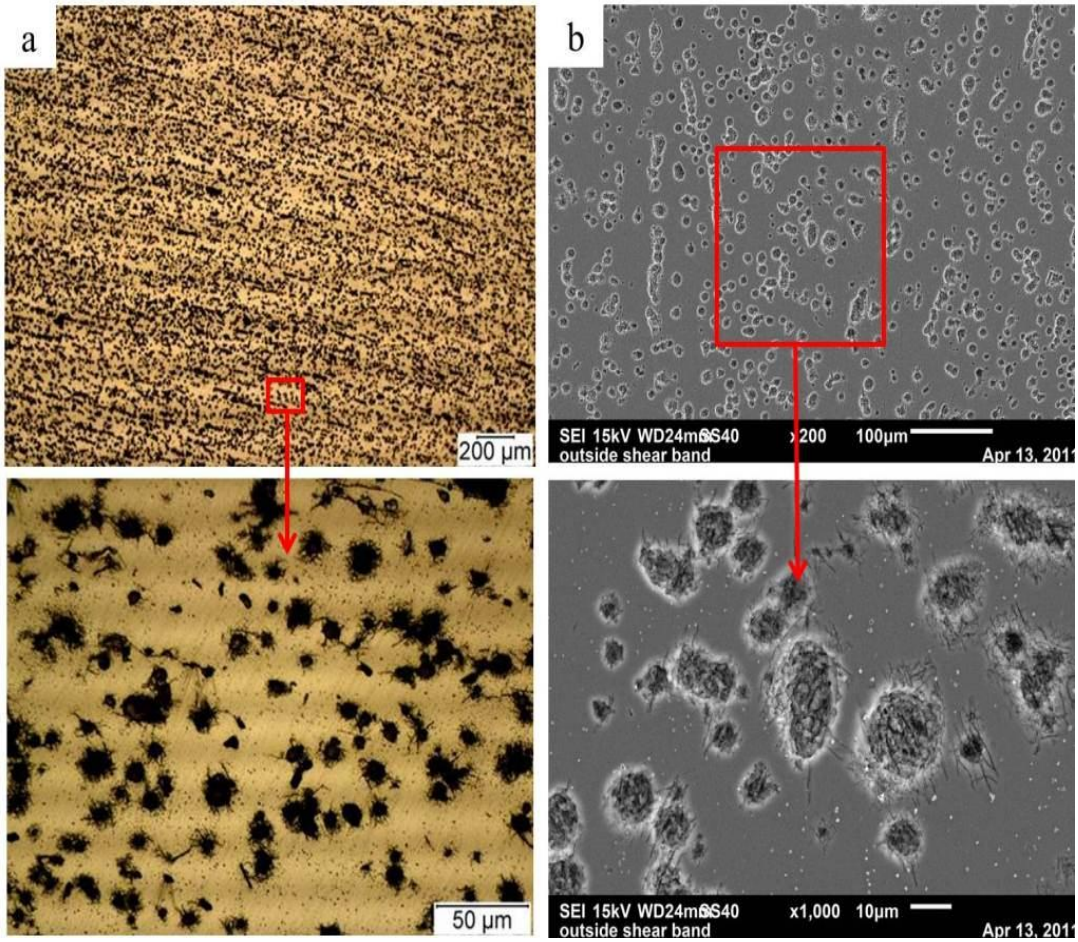

Figure 4.19. (a) Optical and (b) SEM micrographs of AA2099-T62 alloy showing elongated grain structure and second phase particles.

Optical micrographs of AA2099-T81 (Fig 4.20a) show an elongated grain structure containing very fine second phase particles. These second phase particles are more than those observed in T4, T61 and T62 temper conditions. They appear to be irregular in shapes and sizes. They are also uniformly dispersed within the microstructure. These particles appear to be orderly arranged and well dispersed as observed in the SEM image shown in Figure 4.20b. The SEM micrographs also reveal the presence of spherically shaped second phase particles in the alloy. This uniform dispersion caused by the addition of dispersoids causes slip to be homogenized thereby controlling recrystallization and grain sizes. During slip homogenization, dislocations are uniformly distributed within the microstructure. This make the time for dislocation pile-up around the second phase particles longer. The strength increase associated with each second

phase particle; be it coherent or incoherent has been discussed in section 4.1.3. This further explains the increase in strength observed in AA2099-T81 under quasi-static loading compared to the non-cold worked specimens (T4, T61 and T62).

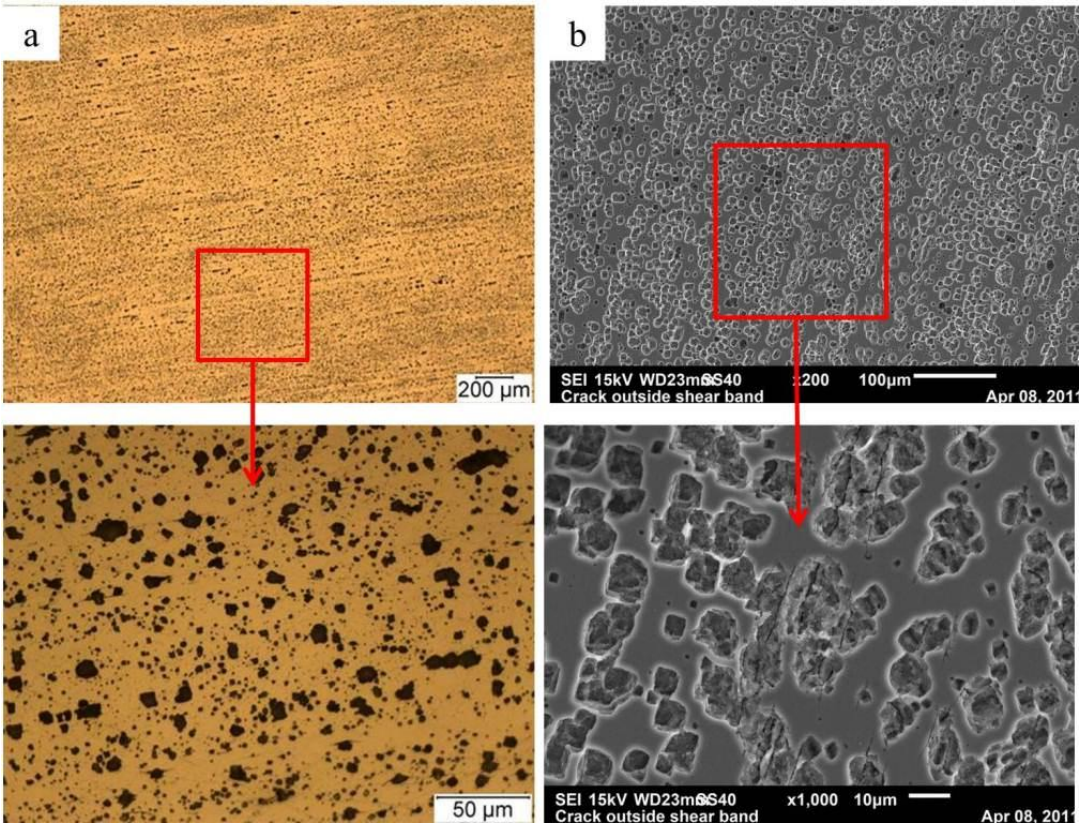

Figure 4.20. (a) Optical and (b) SEM micrographs of AA2099-T81 alloy showing elongated grain structure and second phase particles.

The irregular shaped second phase particles observed in AA2099-T81 become very coarse in AA2099-T82 (Fig 4.21a) even though it is still within the peak-aged region. The second phase particles, when viewed using the scanning electron microscope (Fig 4.21b), appear to be much coarser and closely packed. The tiny white second phase particles observed in AA2099-T81 are also clearly visible. Due to the big sizes and close packed nature of these particles, the effective distances between the particles are reduced thereby making dislocation motion difficult. This leads to increase in strength in AA2099-T82 and increased resistance to deformation under quasi-static loading. These tiny white particles were also observed in AA2099-T61 and AA2099-T62 as discussed earlier. However, they are conspicuously absent in AA2099-T4 and AA2099-T81. The

absence of this white particle can be responsible for the similar levels of hardness and compressive strains observed in AA2099-T4 and AA2099-T81 during quasi-static compression loading.

Similarly in AA2099-T8 (Fig 4.22a), the elongated grains appear to contain coarse second phase particles. It will be recalled that AA2099-T8 is the as-received alloy in T8 temper condition which was also subjected to two-step aging by the manufacturer. The fraction of these coarse second phase particles observed in AA2099-T8 are smaller than those found in AA2099-T82. This explains why AA2099-T8 possesses less deformation resistance than A2099-T82 under quasi-static loading. Secondary electron image of the alloy also reveals the presence of the white tiny particles alongside the coarse grains (Fig 4.22b). However, the low deformation resistance of AA2099-T81 compared to AA2099-T82 is attributed to the second stage precipitation hardening. This is also in agreement with the hypothesis proposed by Romios *et al*. [10]. As mentioned earlier, the higher deformation resistance in these cold worked specimens (T81, T82 and T8) under quasi-static loading over non-cold worked specimens (T4, T61 and T62) is largely due to the presence of T_1 and S phases which nucleates on dislocations. So, they occur in T81, T82 and T8 temper conditions of AA2099 aluminum alloy.

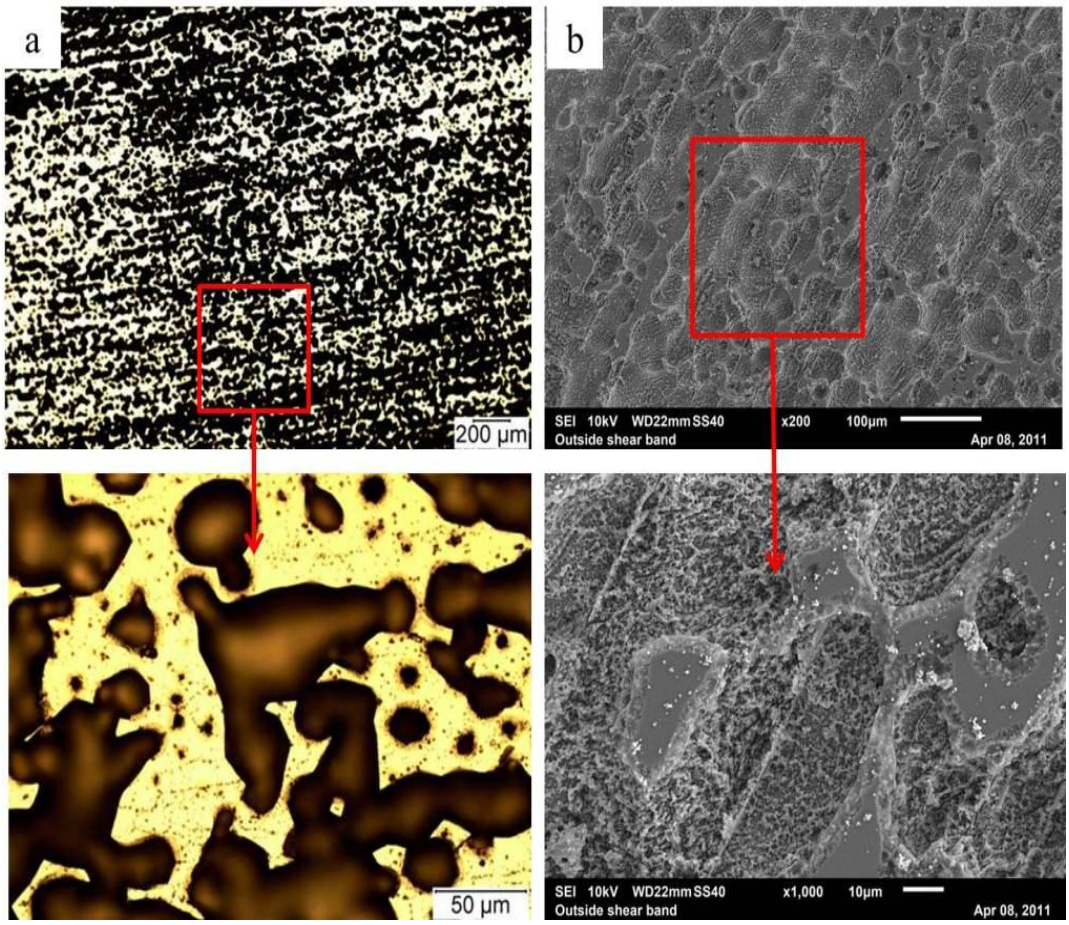

Figure 4.21. (a) Optical and (b) SEM micrographs of AA2099-T82 alloy showing elongated grain structure and second phase particles.

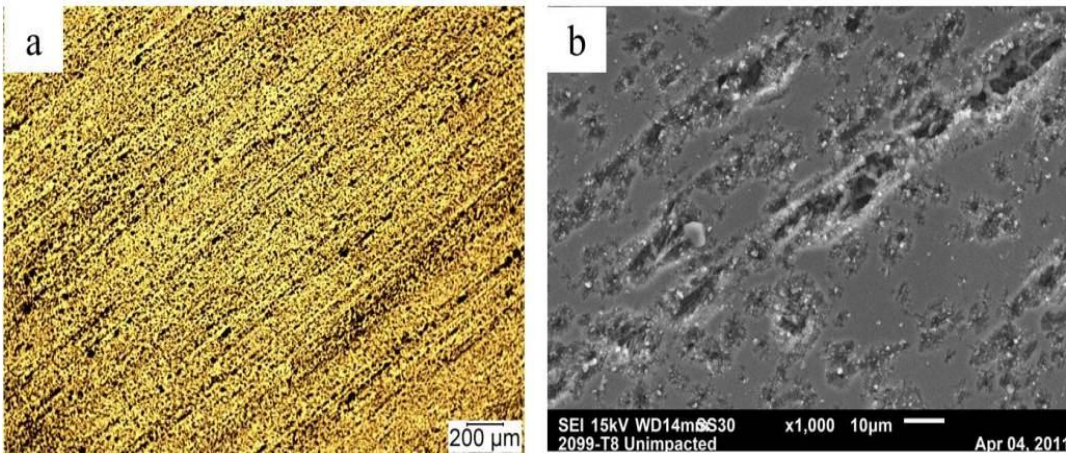

Figure 4.22. (a) Optical and (b) SEM micrographs of AA2099-T8 alloy showing elongated grain structure and second phase particles.

4.3.1.2 AA6061 aluminum alloys

Optical microscopic examinations of the AA6061 aluminum alloy in T4, T6 and T8 temper conditions reveal equi-axed grain structure. The optical micrographs of the alloy in these temper conditions are similar. Second phase particles are observed to be uniformly distributed within the microstructure (Fig 4.23). These second phase particles as discussed in section 4.1.3 are Q, θ (Al_2Cu) and β (Mg_2Si). SEM investigations of AA6061-T4 (Fig 4.24) using secondary electron imaging technique reveals irregularly shaped second phase particles. However in AA6061-T6 (Fig 4.25) and AA6061-T8 (Fig 4.26), the second phase particles appear rectangular in shape. The HF-containing etching solution preferentially attacks the precipitates and they appear as grooves under the scanning electron microscope (Fig 4.27).

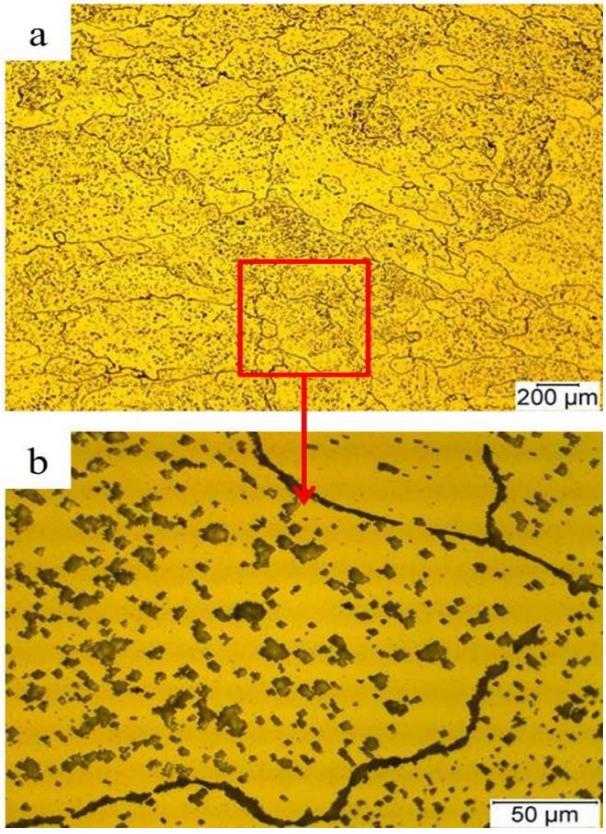

Figure 4.23. Typical optical micrographs of AA6061 alloy showing the equi-axed grain structure.

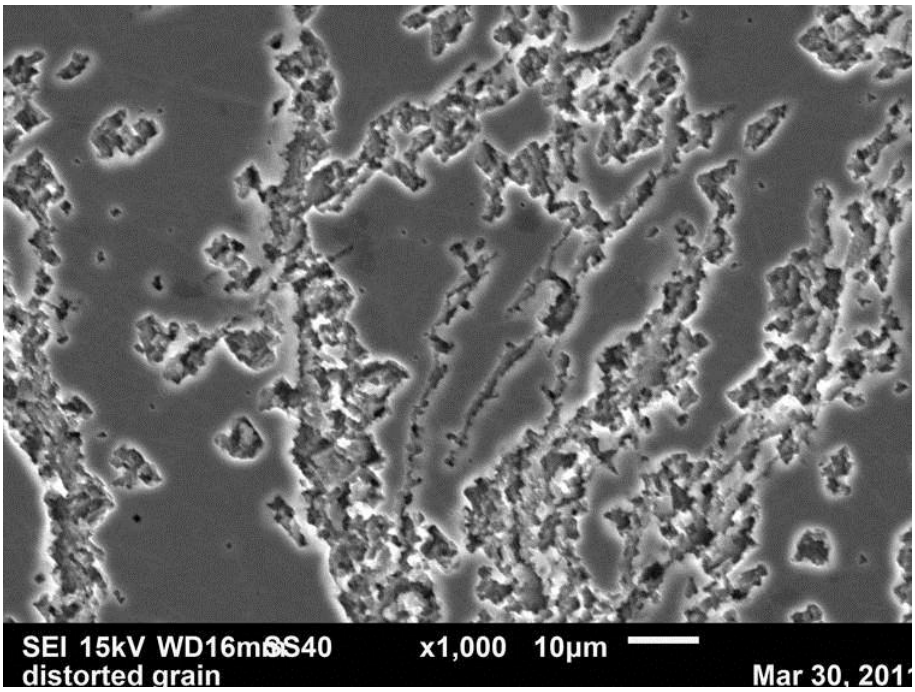

Figure 4.24. SEM micrograph of AA6061-T4 alloy showing irregularly shaped second phase particles.

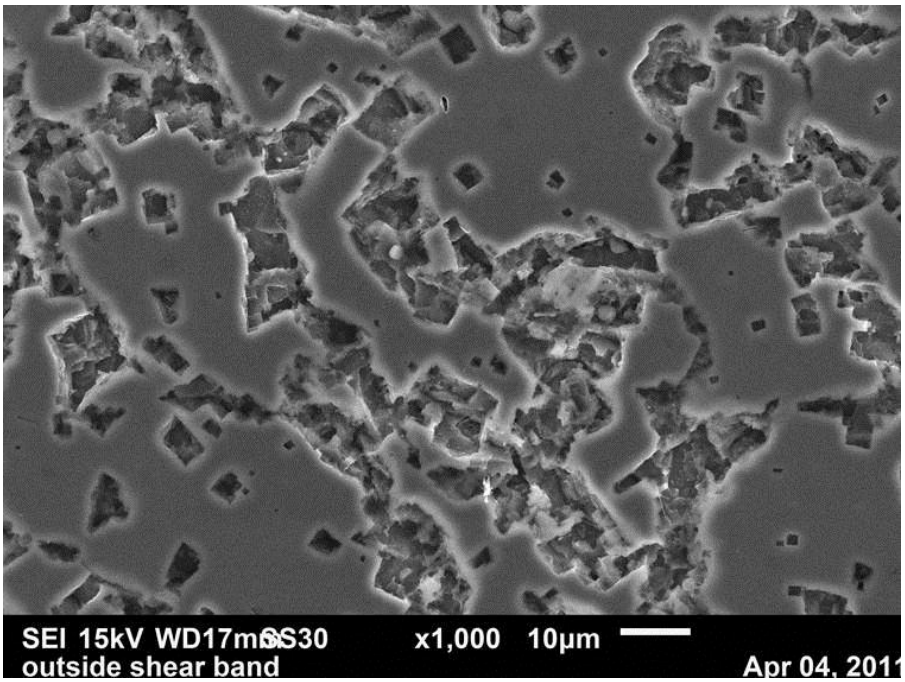

Figure 4.25. SEM micrograph of AA6061-T6 alloy showing rectangular shaped second phase particles.

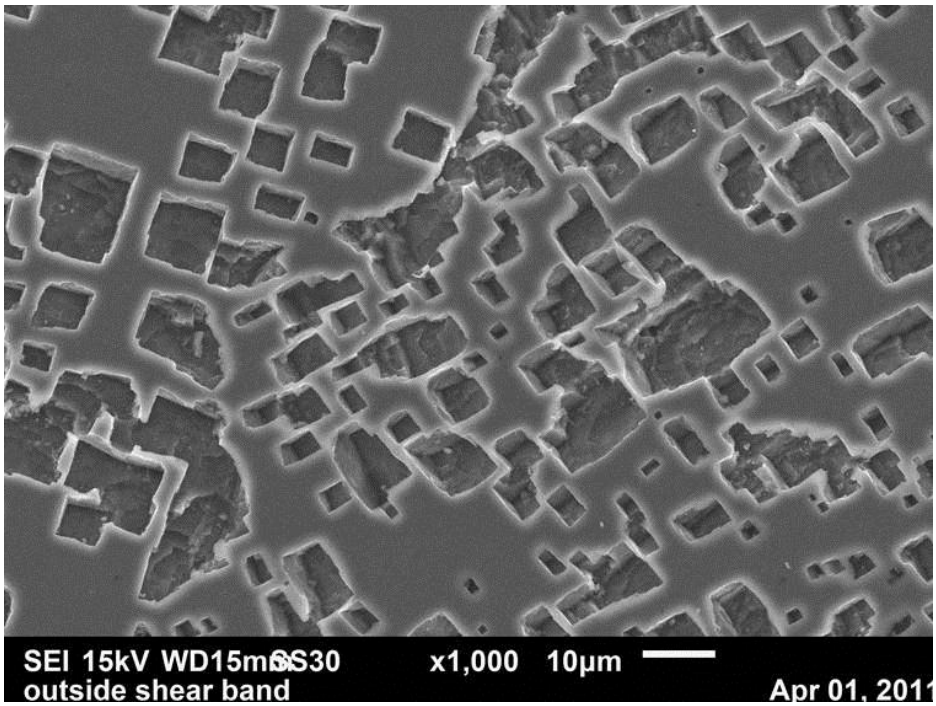

Figure 4.26. SEM micrograph of AA6061-T8 alloy showing rectangular shaped second phase particles.

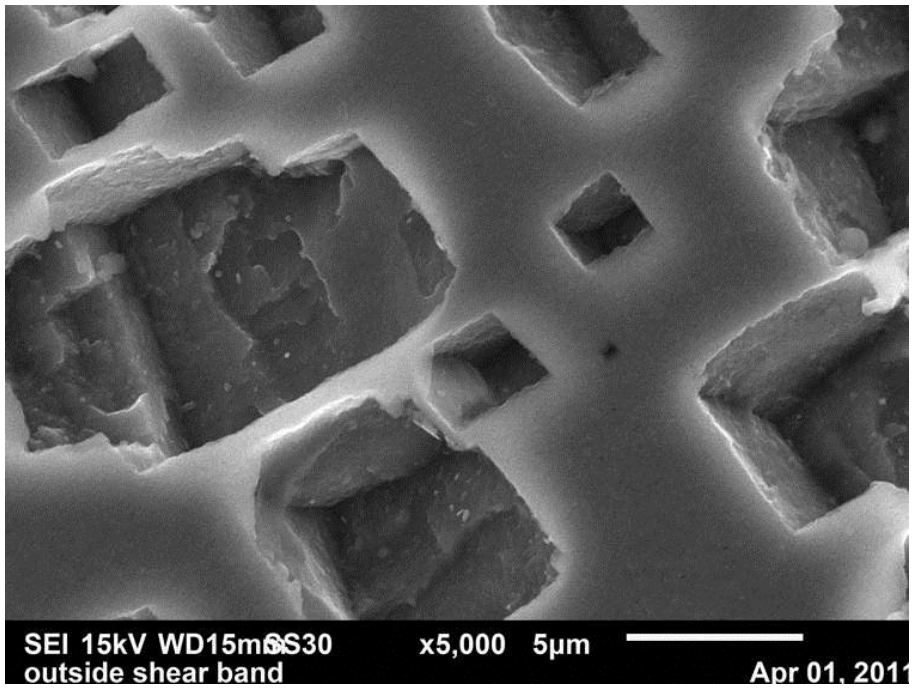

Figure 4.27. SEM micrograph of AA6061-T8 alloy showing rectangular shaped second phase particles at high magnification.

4.3.2 Microstructure of heat treated samples after impact

4.3.2.1 AA2099 aluminum alloy (Optical Microscopy)

The experimental data sheet showing the occurrence of strain localisation in various impacted specimens of the two investigated aluminum alloys as influenced by the strain rates or impacted momentum is provided in Table 4.3. Optical microscopic examination of AA2099-T4 impacted at 28 kg m s^{-1} reveals a microstructure free of shear band. The micrograph is the same as that of un-impacted AA2099-T4 shown in figure 4.17. As impact momentum reached 33 kg m s^{-1}, a heavily deformed band appeared (Fig 4.28a). But when impacted at 39 kg m s^{-1}, a faint transformed band appeared along with crack in the microstructure (Fig 4.28b).

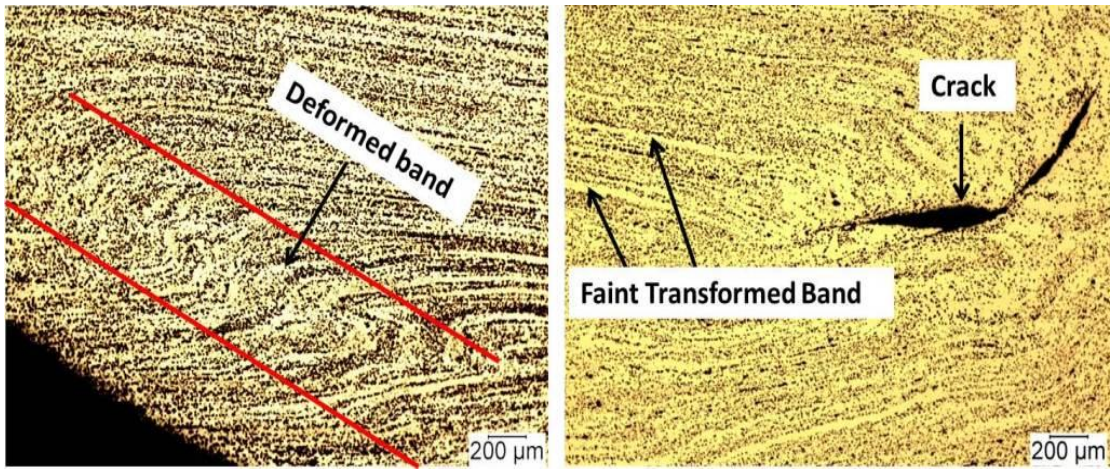

Figure 4.28. Optical micrographs of AA2099-T4 alloy showing (a) heavily deformed band when impacted at 33 kg m s^{-1}, and (b) faint transformed band and crack when impacted at 39 kg m s^{-1}.

For the impacted AA2099-T61 alloy, a slightly deformed band was observed at 28 kg m s^{-1} (Fig 4.29). When impacted at 31 kg m s^{-1}, a faint transformed band was observed (Fig 4.30a) as well as crack (4.30b) traversing the alloy. When impacted at 39 kg m s^{-1} momentum, the faint transformed bands were still observed along with multiple cracks traversing the alloy. In AA2099-T62, a deformed band was also observed at 28 kg m s^{-1} momentum (Fig 4.31). When impacted at 33 kg m s^{-1}, transformed band (Fig 4.32a) appeared alongside deformed band (Fig 4.32b). A high

viscous plastic flow of metal showing extreme strain localization (4.33a) was observed in addition to cracks propagating along shear band (4.33b). The plastic flow of metal observed is an indication of the high intensity of heating in this region of the impacted specimen. Severe localization was observed with crack along shear band at 39 kg m s^{-1} momentum (Fig 4.34).

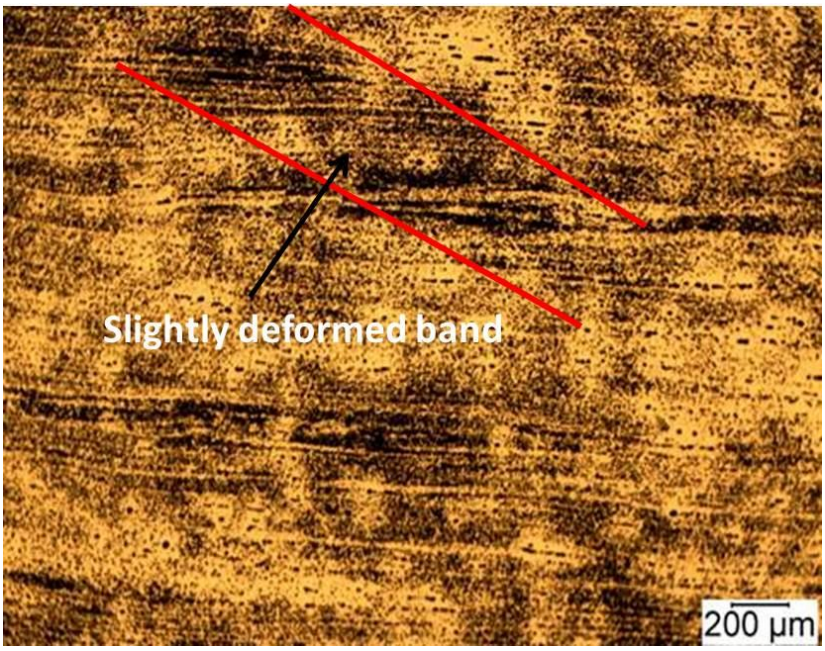

Figure 4.29. Optical micrograph of AA2099-T61 alloy impacted at 28 kg m s^{-1} showing slightly deformed band.

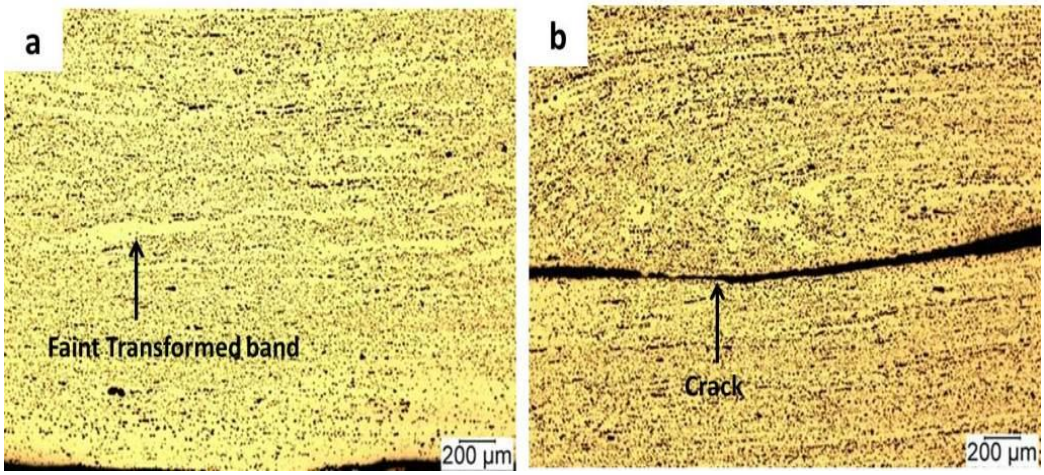

Figure 4.30. Optical micrographs of AA2099-T61 alloy impacted at 31 kg m s^{-1} showing (a) faint transformed band and (b) crack traversing the alloy.

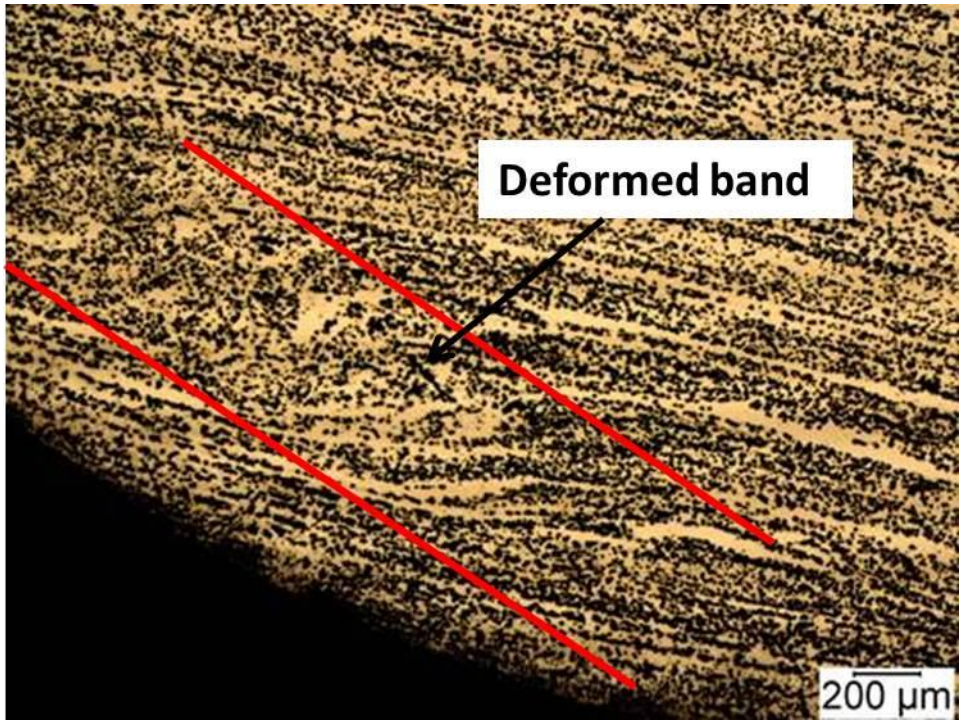

Figure 4.31. Optical micrograph of AA2099-T62 impacted at 28 kg m s^{-1} showing deformed band.

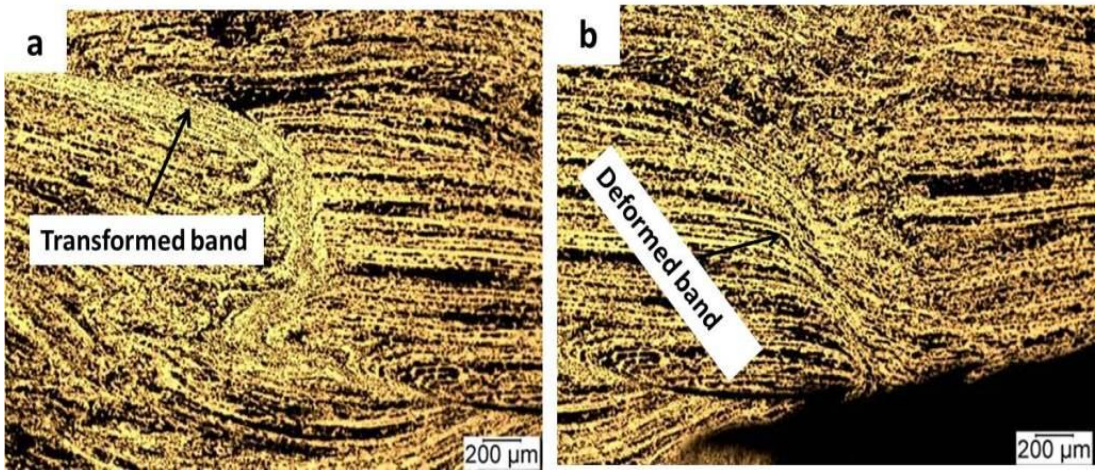

Figure 4.32. Optical micrographs of AA2099-T62 alloy impacted at 33 kg m s^{-1} showing (a) transformed band and (b) deformed band.

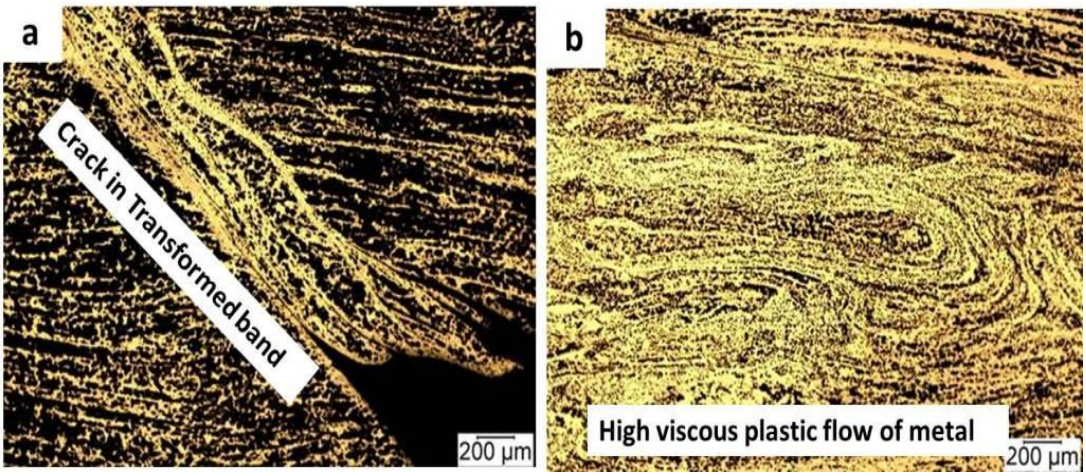

Figure 4.33. Optical micrographs of AA2099-T62 alloy impacted at 33 kg m s^{-1} showing (a) crack propagating through transformed band, and (b) high viscous plastic flow of metal.

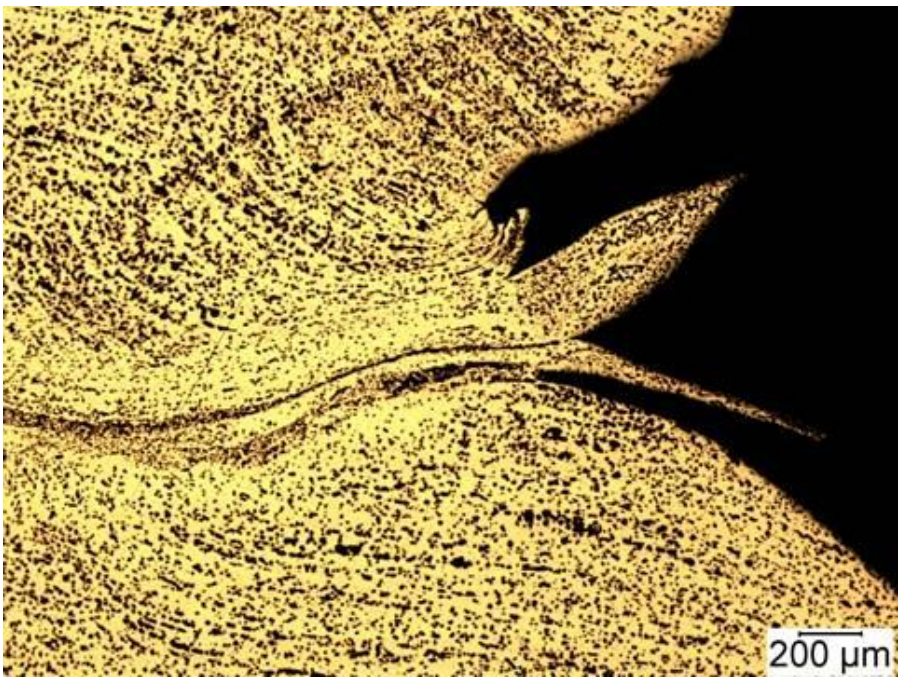

Figure 4.34. Optical micrograph of AA2099-T62 alloy impacted at 39 kg m s^{-1} showing severe strain localization along transformed band.

In AA2099-T81 alloy, slightly deformed band (Fig 4.35) was observed when impacted at 28 kg m s^{-1}. At 31 kg.m/s momentum, very faint transformed band was observed and cracks were observed propagating across the alloy (Fig 4.36a). Heavily distorted grain and crack propagating along transformed band (Fig 4.36b) were observed at 39 kg m s^{-1} momentum. In AA2099-T82, transformed band was observed at the edge of the sample when impacted at 28 kg m s^{-1} (Fig 4.37). At 33 kg m s^{-1}, crack was observed propagating along shear band as well as a fully formed crack traversing the specimen (Fig 4.38a). At 39 kg m s^{-1}, multiple shear bands as well as multiple cracking occurred along a shear band (4.38b). In the as received condition (AA2099-T8), transformed band was also observed when impacted at 28 kg m s^{-1} and fully formed cracks were observed traversing the alloy (Fig 4.39a). At 31 kg m s^{-1}, bifurcation of shear band occurred and high viscous plastic flow was observed within shear band at 33 kg m s^{-1} (Fig 4.39b). Figure 4.40 shows a general overview of shear band in AA2099-T8 impacted at 39 kg m s^{-1} showing bifurcation of shear band.

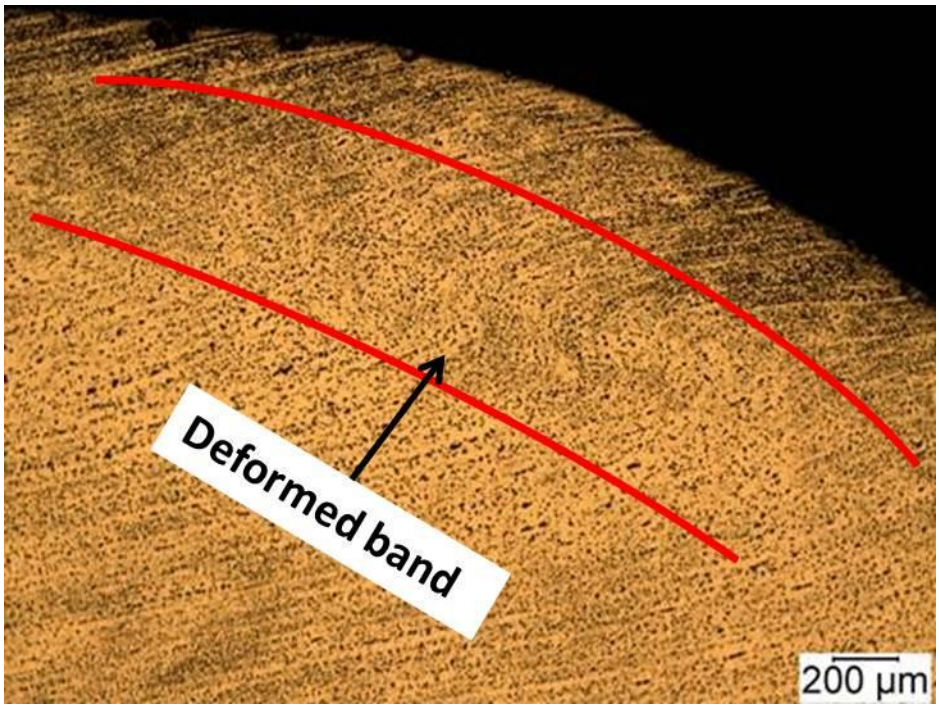

Figure 4.35. Optical micrograph of AA2099-T81 alloy impacted at 28 kg m s^{-1} showing slightly deformed band.

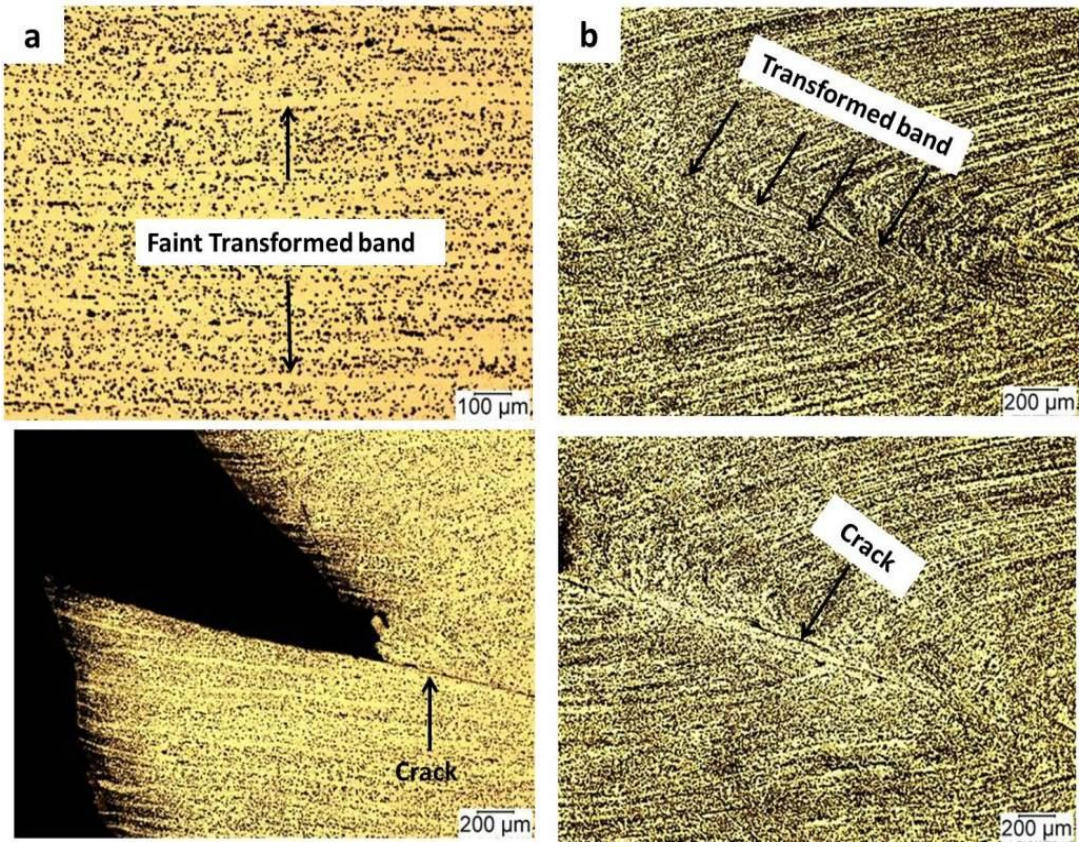

Figure 4.36. Optical micrographs of AA2099-T81 alloy showing (a) very faint transformed band and cracks propagating through transformed band when impacted at 31 kg m s^{-1}, and (b) heavily distorted grain and crack propagating along transformed band at 39 kg m s^{-1}.

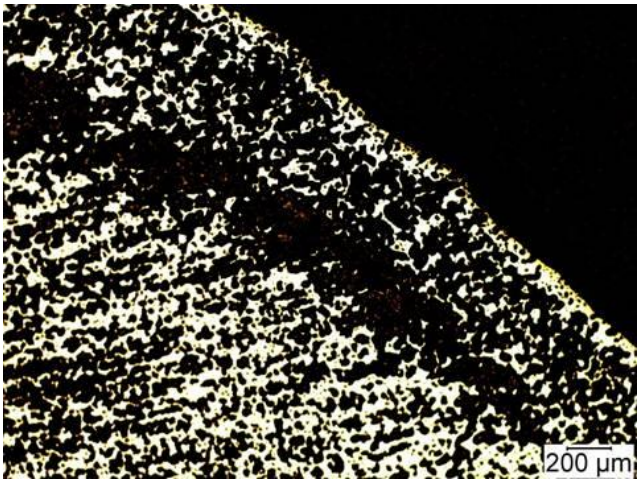

Figure 4.37. Optical micrograph of AA2099-T82 alloy impacted at 28 kg m s^{-1} showing transformed band.

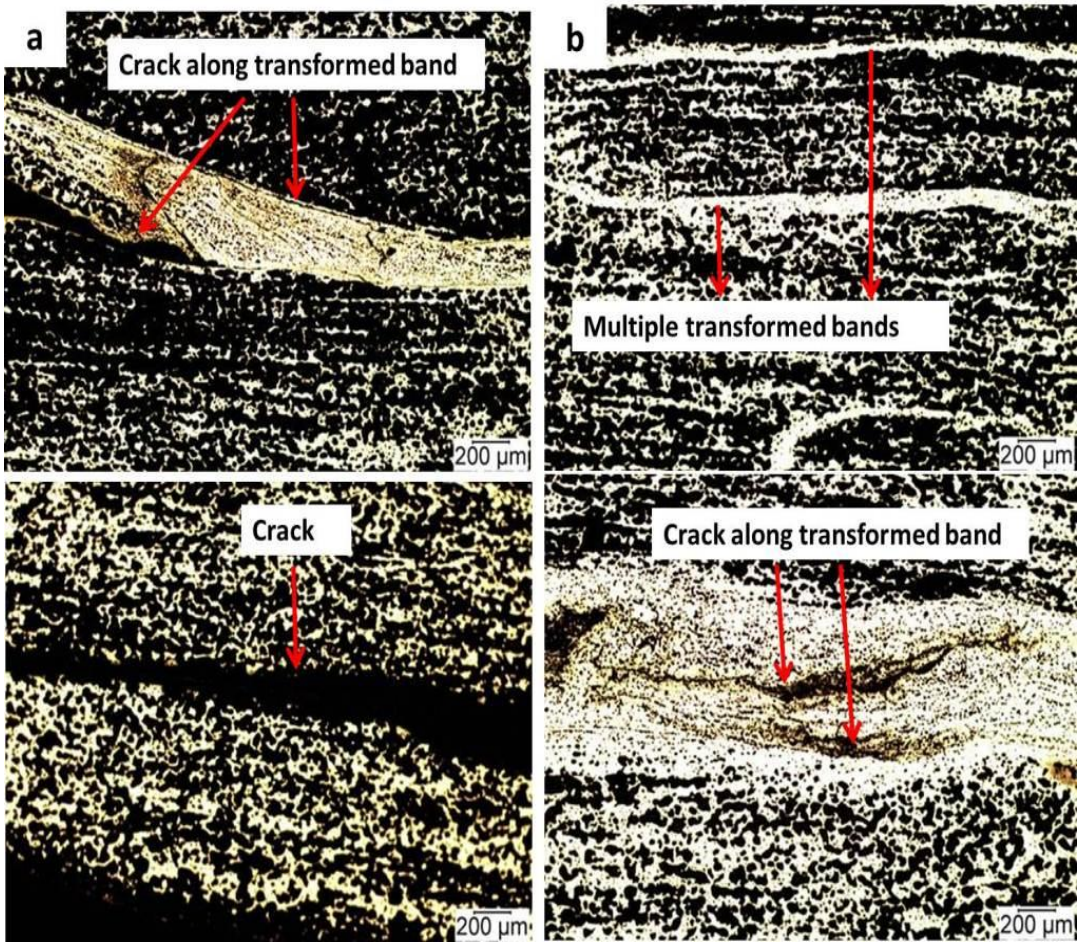

Figure 4.38. Optical micrographs of AA2099-T82 alloy showing (a) crack propagating along transformed band and fully formed crack traversing the specimen when impacted at 33 kg m s^{-1}, and (b) multiple transform bands and multiple crack propagation along transform band when impacted at 39 kg m s^{-1}.

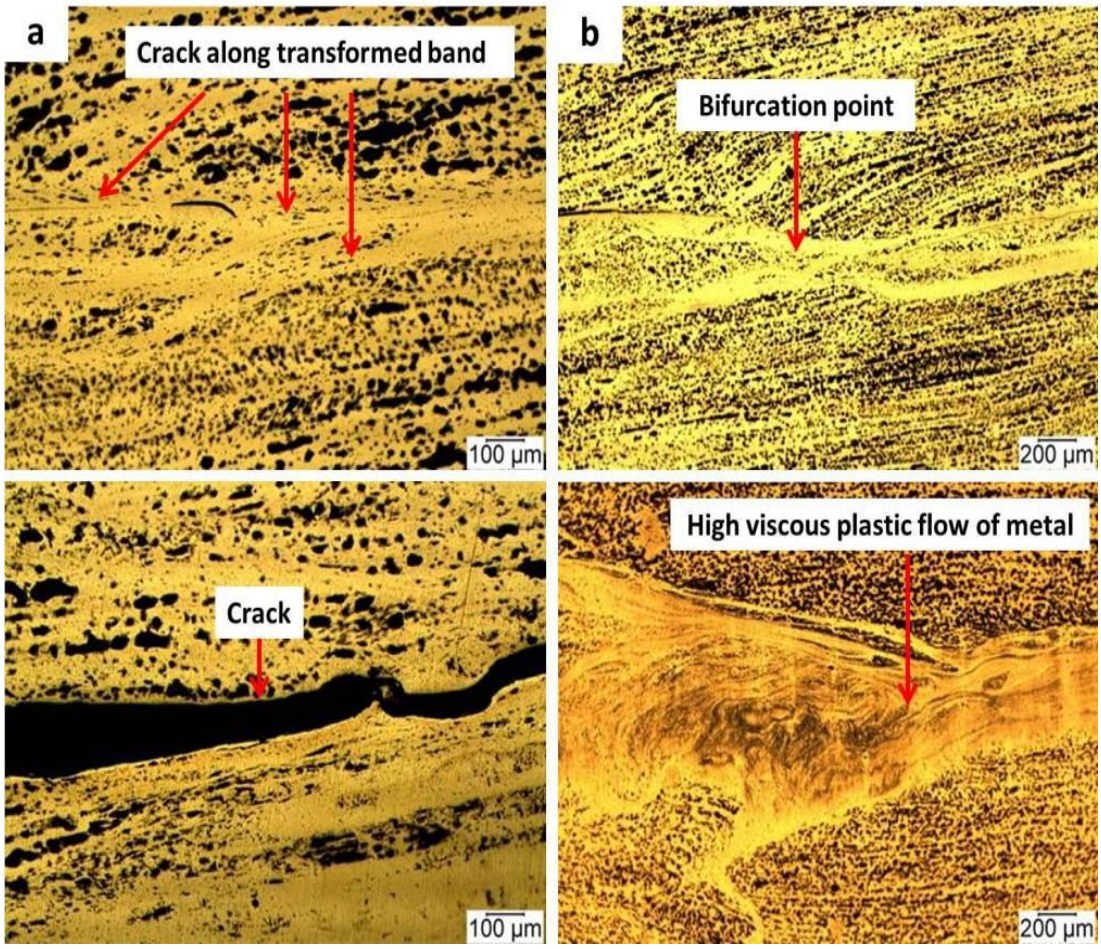

Figure 4.39. Optical micrographs of AA2099-T8 alloy showing (a) transformed band and fully formed cracks traversing the alloy when impacted at 28 kg m s^{-1}, and (b) bifurcation of shear band appears at 31 kg m s^{-1} and high viscous plastic flow of metal within shear band at 33 kg m s^{-1}.

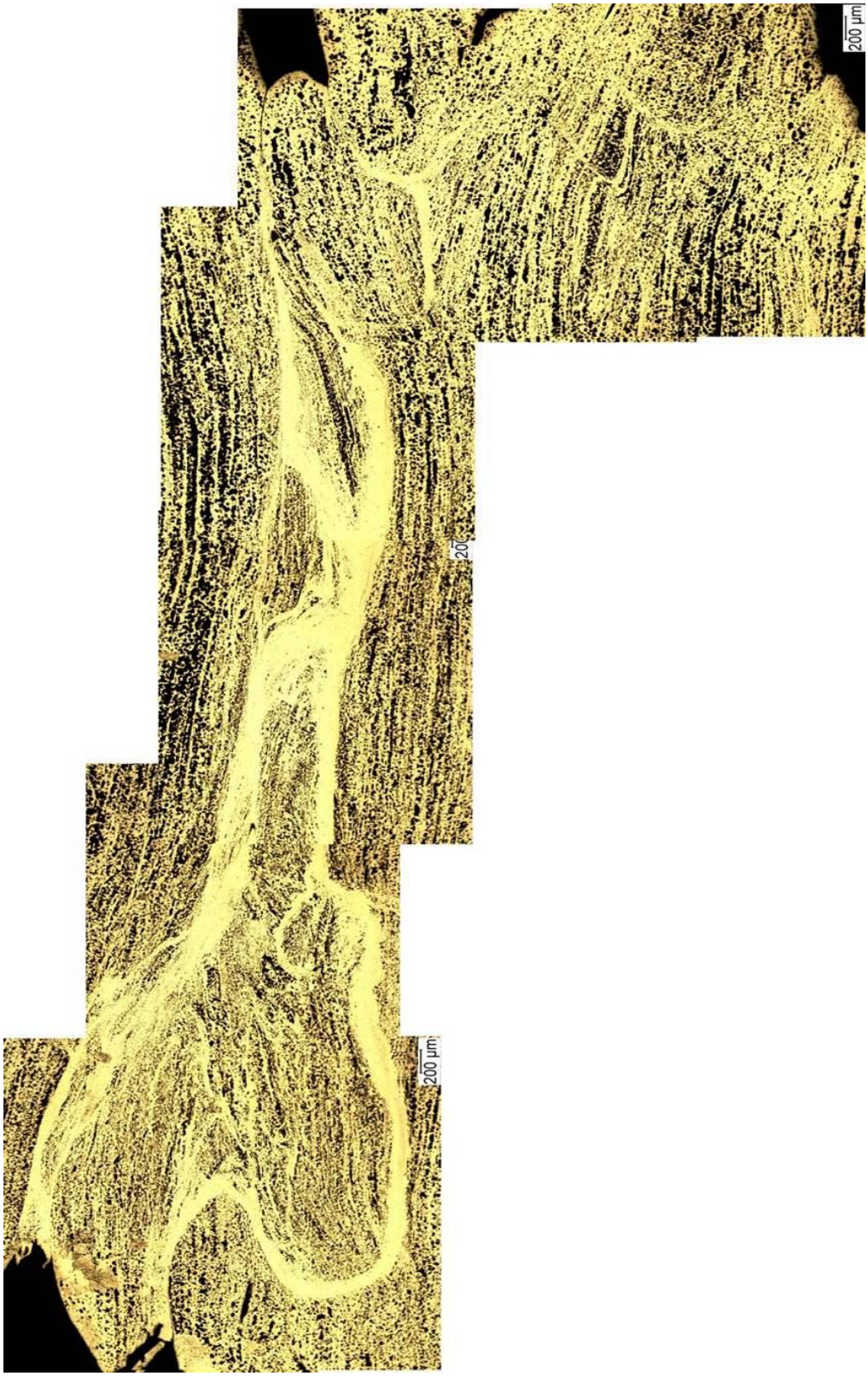

Figure 4.40. Optical micrographs showing an overview of the transformed band formed in AA2099-T8 alloy specimens impacted at 39 kg m s^{-1}.

Optical microscopic investigations of AA2099 impacted at 28 kg m s^{-1} showed no shear band in T4 temper condition while deformed band was observed in T61, T62 and T81 temper conditions. Transformed band was observed in T82 and T8 temper conditions. As previously discussed in chapter two, there is a critical strain rate for the formation of either deformed band or transformed band. This implies that T4 temper has the lowest tendency to form adiabatic shear bands compared to T61, T62, T81 and T82 tempers. This is in line with the low tendency for formation of adiabatic shear band observed in T61 (slightly deformed band) compared to T62 (well deformed band) as well as T81 (slightly deformed band) compared to T82 or T8 (transformed band). The critical strain rate for formation of deformed band is always lower than that required to form transformed band. The occurrence of faint transformed band at impact momentum of 31 kg m s^{-1} in T61 and T81 compared to the heavily formed transformed band in T82 and T8 is also an indication of the lower tendency for formation of adiabatic shear band in the T82 and T8 alloy. The results of microstructural investigation are in good agreement with the analysis of dynamic stress-strain curves for this alloy both in compression and in torsion.

The high viscous plastic flow observed in T62 and T8 at 33 kg m s^{-1} occurred as a result of the intense localized adiabatic heating, which caused dissolution of second phase particles inside the transformed bands. This was also observed inside the transformed band of AA2099-T82 and AA2099-T8. This explains why there was an early drop in maximum flow stress values experienced in the dynamic stress-strain curves of AA2099-T82 (Fig 4.9) and AA2099-T8 (Fig 4.10). For this reason, AA2099-T82 and AA2099-T8 have very high engineering strain and strain rates values as shown in Table 4.2. Splitting of transformed band along direction of propagation is observed in T8 temper condition (Fig 4.40). This unique special pattern of adiabatic shear band called bifurcation, occurs when barriers such as second phase particle and impurity inhibits the shear band propagation along its original path thereby forcing the shear band to change direction [121]. Apart from bifurcation, shear bands are also known to exhibits other special pattern such as crossing, collection, annihilation and N-shape [121,122].

4.3.2.2 AA2099 aluminum alloy (Scanning Electron Microscopy)

Scanning electron microscopic investigations were carried out on AA2099 aluminum alloy specimens impacted at 39 kg m s^{-1} using secondary electron and backscattered electron imaging techniques. The microstructures of the region inside and outside shear band were investigated in more detail than possible using optical microscopy. In AA2099-T4, secondary electron image of the region inside the shear band reveal the shearing of second phase particles along the crack propagation path which appear at the boundary region between shear band and the bulk material (Fig 4.41a).

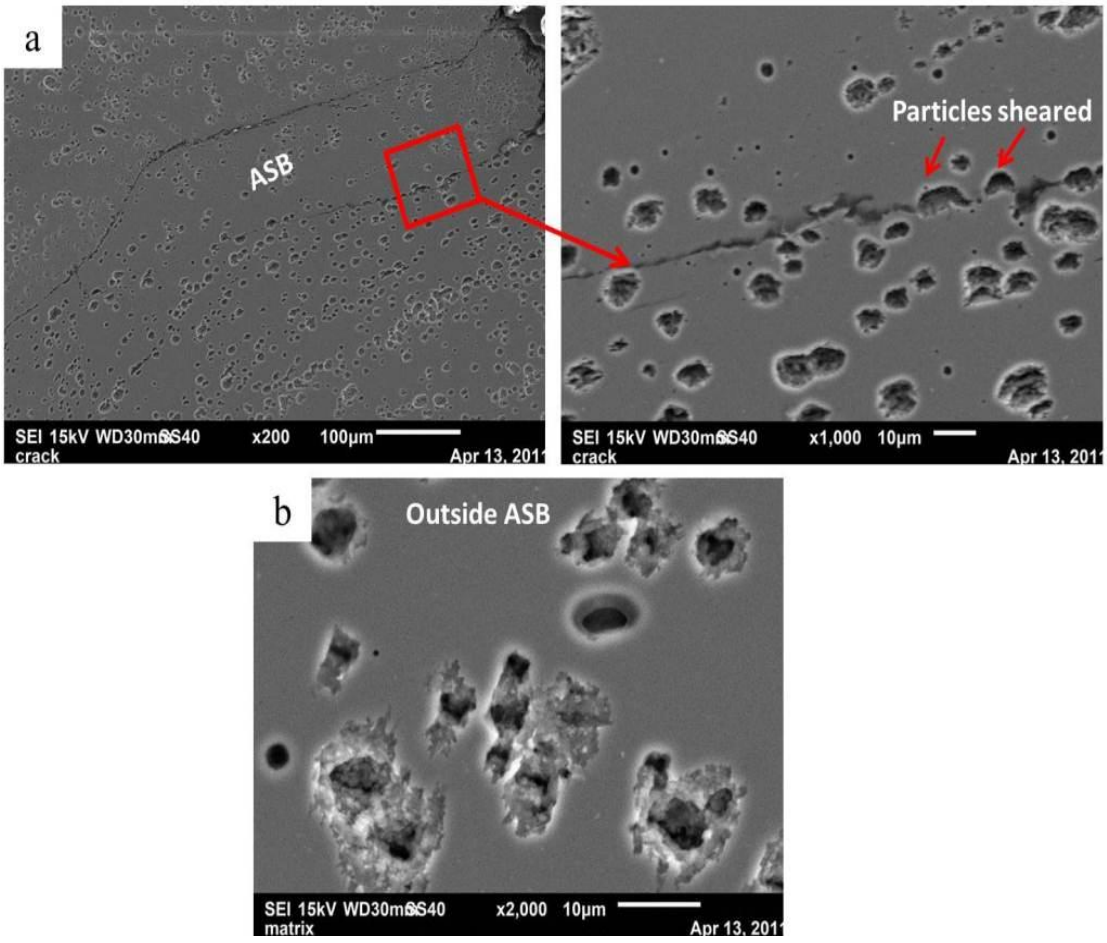

Figure 4.41. SEM micrographs of impacted AA2099-T4 alloy showing (a) shearing of second phase particles along the crack propagation path within the shear band region, and (b) sparse distribution of second phase particles in regions outside the shear band.

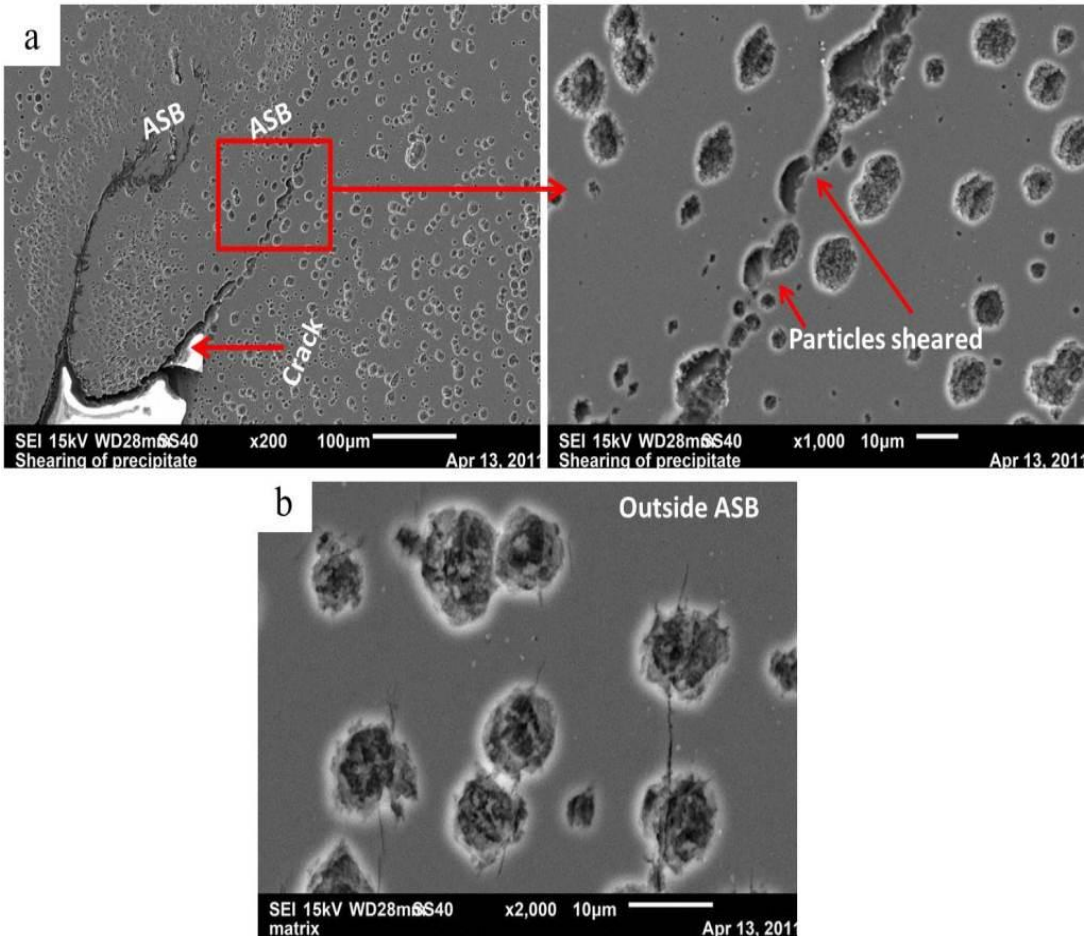

Figure 4.42. SEM micrographs of impacted AA2099-T61 alloy showing (a) shearing of second phase particles along the crack propagation path within the shear band region, and (b) single crack cutting across second phase particles in the regions outside shear band.

In AA2099-T61, secondary electron image also reveal particle shearing along crack propagation path within the shear band (Fig 4.42a). These particles shear due to the misfit strains formed around them. As the coherent particles grow, misfits strain fields are generated between these particles and the host lattice. These misfit strains slow down dislocation motion. For dislocation to pass through these coherent particles, the applied stress must be relatively high. Due to this high stress, shearing of the particles occurs [120]. In the region outside the shear band, single cracks were observed across second phase particles (Fig 4.42b). In AA2099-T62 however, the second phase particles inside the transformed band become elongated instead of being sheared along the crack propagation path. Adjacent to this, particles coalesce into a continuous phase instead of

being sheared or elongated. The high temperature generated created a viscous plastic flow within the shear band which then caused the particles to coalesce (Fig 4.43a). In a way similar to AA2099-T61, multiple cracks appear across the second phase particles in the region outside shear band of AA2099-T62 (Fig 4.43b).

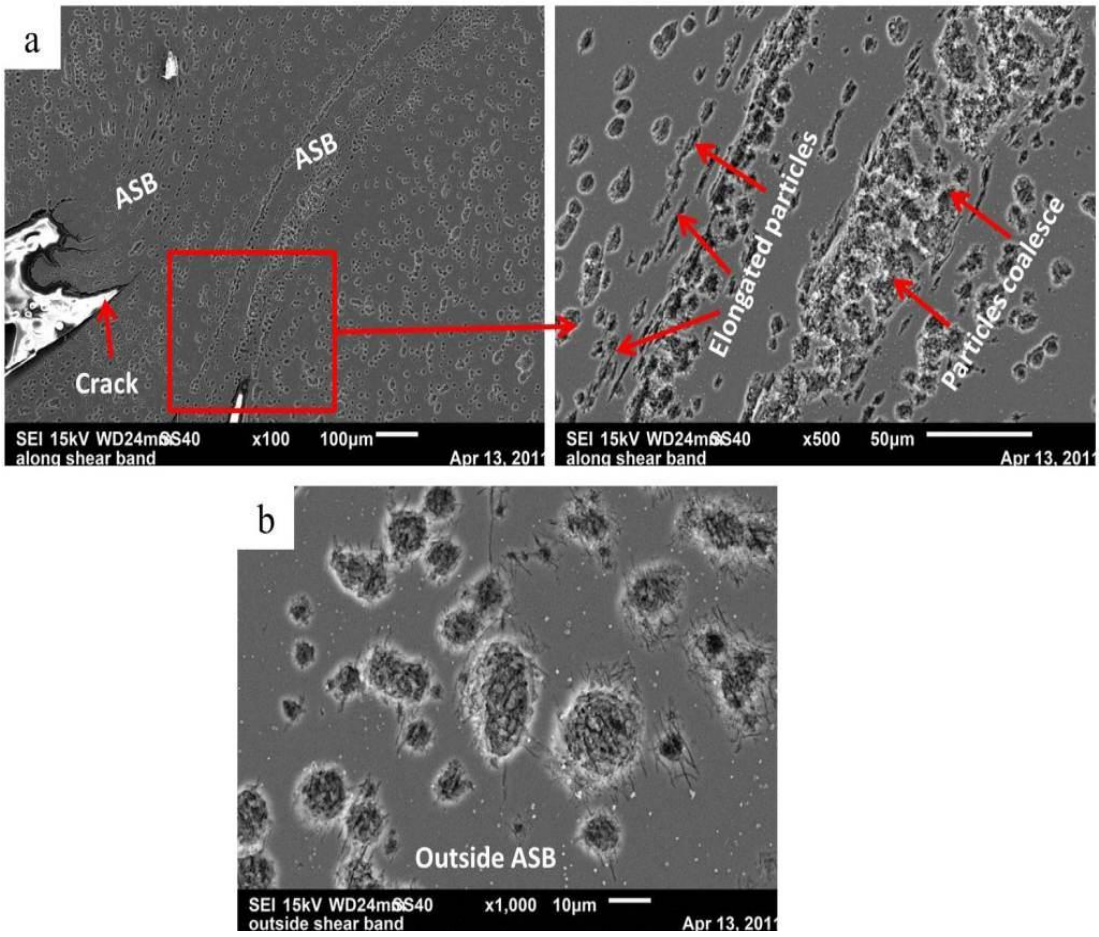

Fig 4.43. SEM micrographs of impacted AA2099-T62 alloy showing (a) elongation of particles along the crack propagation path as well as the coalescence of particles into a continuous phase within the shear band region, and (b) multiple cracks cutting across second phase particles in the regions outside the shear band.

In AA2099-T81, secondary electron images show crack propagating along the boundary region between the bulk matrix and the shear band (Fig 4.44a). The particles in the bulk material at this boundary region very close to the crack are elongated along the crack direction. In the region outside the shear band, cracks are observed across second phase particles (Fig 4.44b). Secondary electron image of region inside shear band of AA2099-

T82 reveals the dissolution of some secondary phase particle inside the shear band (Fig 4.45a). The bigger coarse particles observed before impact dissolved thereby leaving behind the spherically shaped, tiny white and other irregularly shaped particles. Some irregularly shaped particles appear to be squeezed and located within the centre of the shear band. In the region outside the shear band, the particles look the same as that of the un-impacted AA2099-T82 (Fig 4.45b).

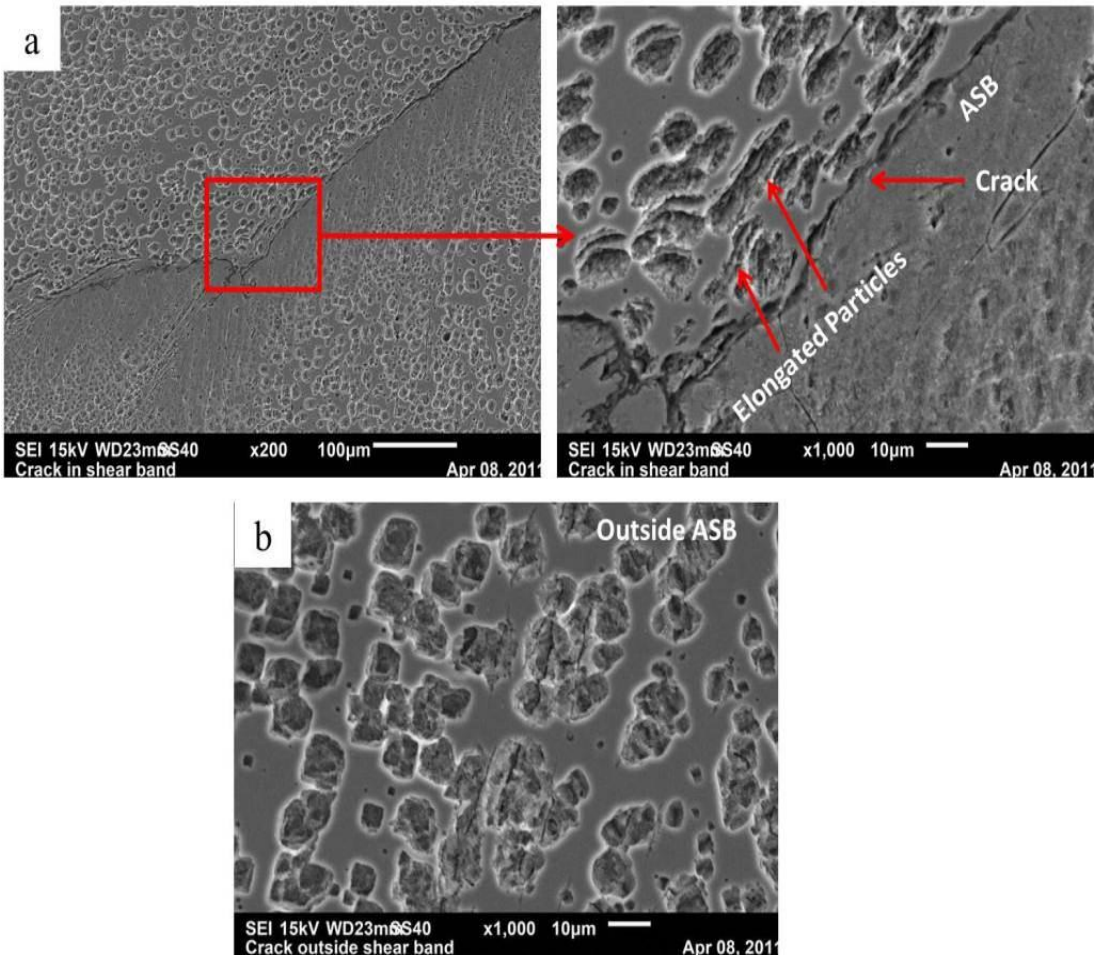

Figure 4.44. SEM micrographs of impacted AA2099-T81 alloy showing (a) crack propagating along the peripheral edge of the shear band as well as particles elongating in direction of the crack, and (b) crack cutting across second phase particles.

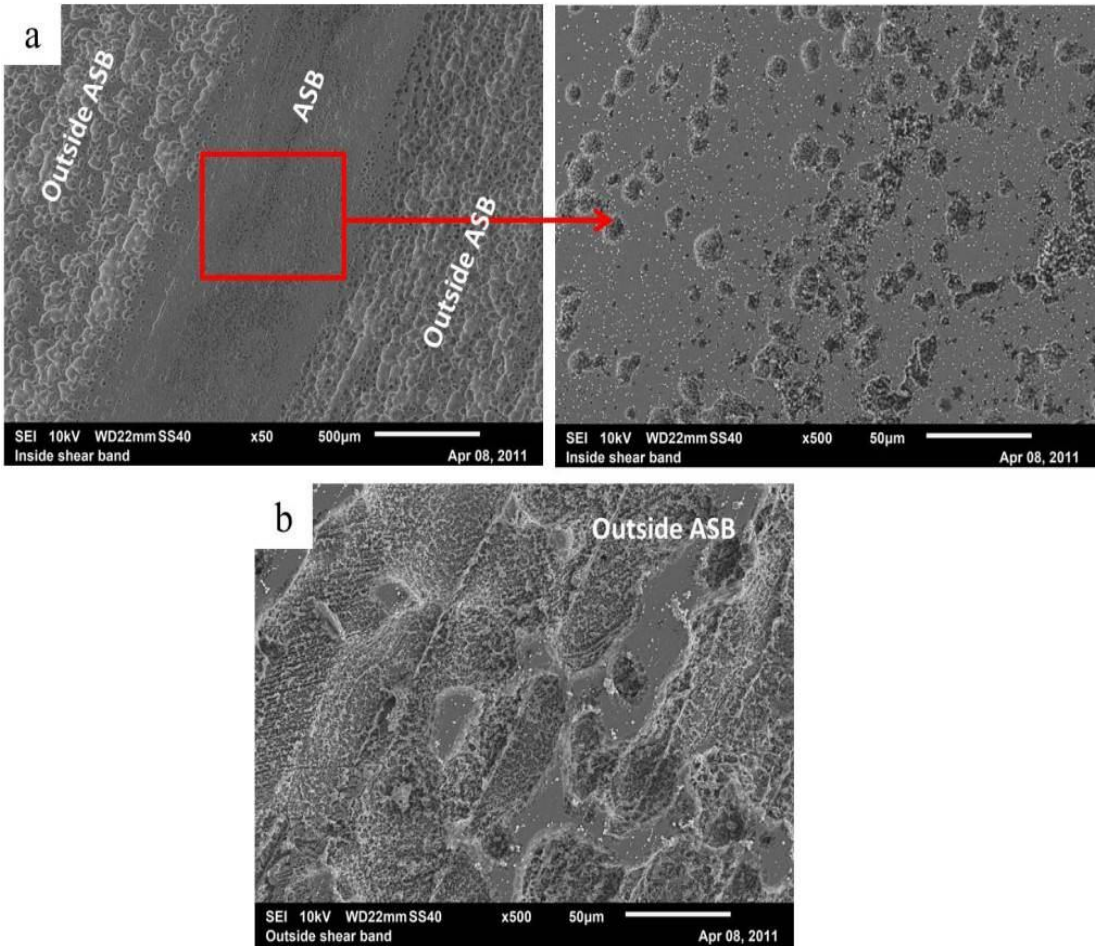

Figure 4.45. SEM micrographs of impacted AA2099-T82 alloy showing (a) dissolution of second phase particles inside shear band as well as the particles squeezed to the centre of the shear band, and (b) coarse particles similar to that present in the un-impacted specimen.

For impacted AA2099-T8 alloy (as received), backscattered electron image of regions within shear band revealed the presence of few second phase particles within the shear band. This means more dissolution of second phase particles took place inside the shear band of AA2099-T8 (Fig 4.46a) compared to AA2099-T82. Few particles were also observed lined up along the centre of the shear band. These particles also appear to be squeezed along the centre of the shear band. Dissolution of the second phase particles occurred due to intense localized adiabatic heating. Due to the rapid cooling of the shear band, there was insufficient time for new particles to precipitate out of the supersaturated solid solution after deformation [117]. Secondary electron image of the region outside the shear band also revealed the same grain structure as that of the un-

impacted AA2099-T8 (Fig 4.46b). However, the grains appeared much smaller than those of AA2099-T82.

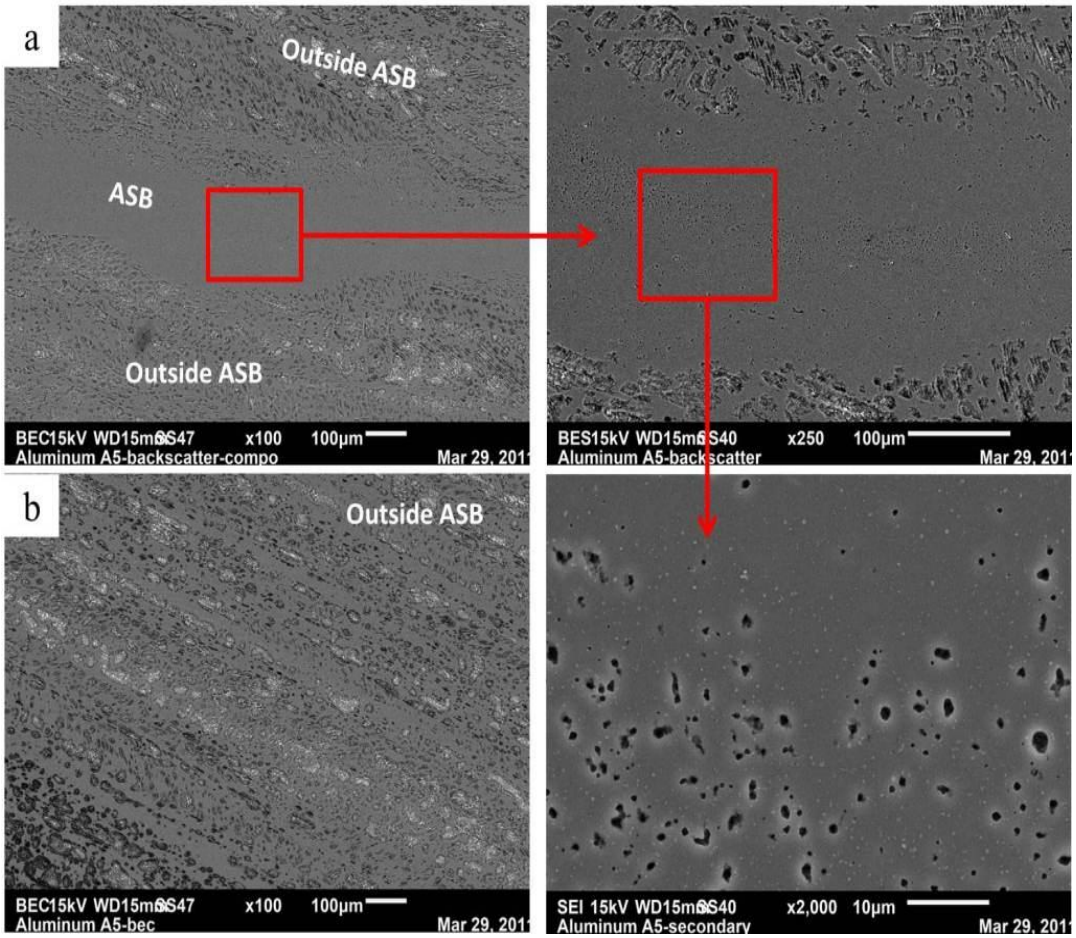

Figure 4.46. SEM micrographs of impacted AA2099-T8 alloy showing (a) dissolution of second phase particles inside shear band as well as the particles squeezed to the centre of the shear band, and (b) coarse particles similar to that present in the un-impacted specimen.

4.3.2.3 AA6061 aluminum alloy (Optical Microscopy)

The results of optical microscopic examinations of the impacted specimens of AA6061 aluminum alloy are shown in Figures 4.47-4.49. Partially formed transformed band was observed in AA6061-T4 alloy when impacted at 33 kg m s^{-1} (Fig 4.47a). This became fully developed at 39 kg m s^{-1} momentum (Fig 4.47b). Transformed bands in this alloy appear darker than the bulk material. These shear bands bifurcated (Fig 4.47c) at 44 kg m s^{-1} momentum and cracks propagated along transformed bands (Fig 4.47d). Deformed band was formed in AA6061-T6 at the sample's edge at 33 kg m s^{-1} momentum (Fig 4.48a). At impact momentum of 39 kg m s^{-1}, transformed band formed at the centre of the alloy (Fig 4.48b) with the deformed band at sample's edge unchanged. At 44 kg m s^{-1}, shear band bifurcated (Fig 4.48c) and crack propagated along the shear band (Fig 4.48d).

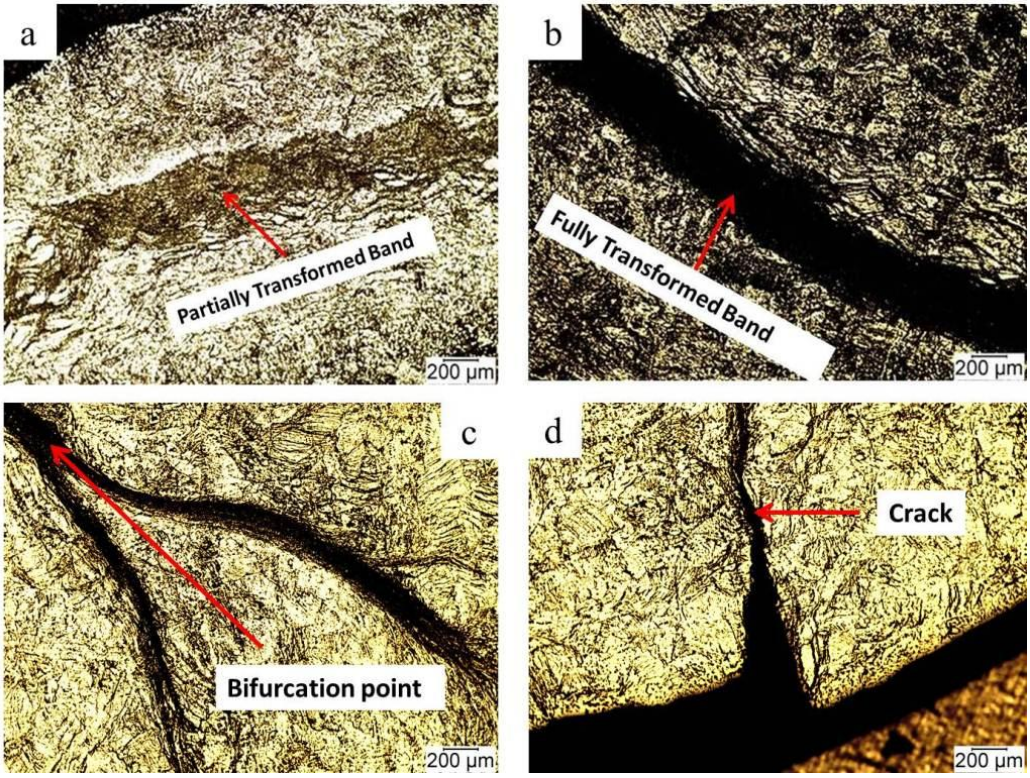

Figure 4.47. Optical micrographs of impacted AA6061-T4 alloy showing (a) partially formed transformed band at 33 kg m s^{-1}, (b) fully formed transformed band at 39 kg m s^{-1}, (c) shear band bifurcation at 44 kg m s^{-1}, and (d) crack propagating through transformed band at 44 kg m s^{-1}.

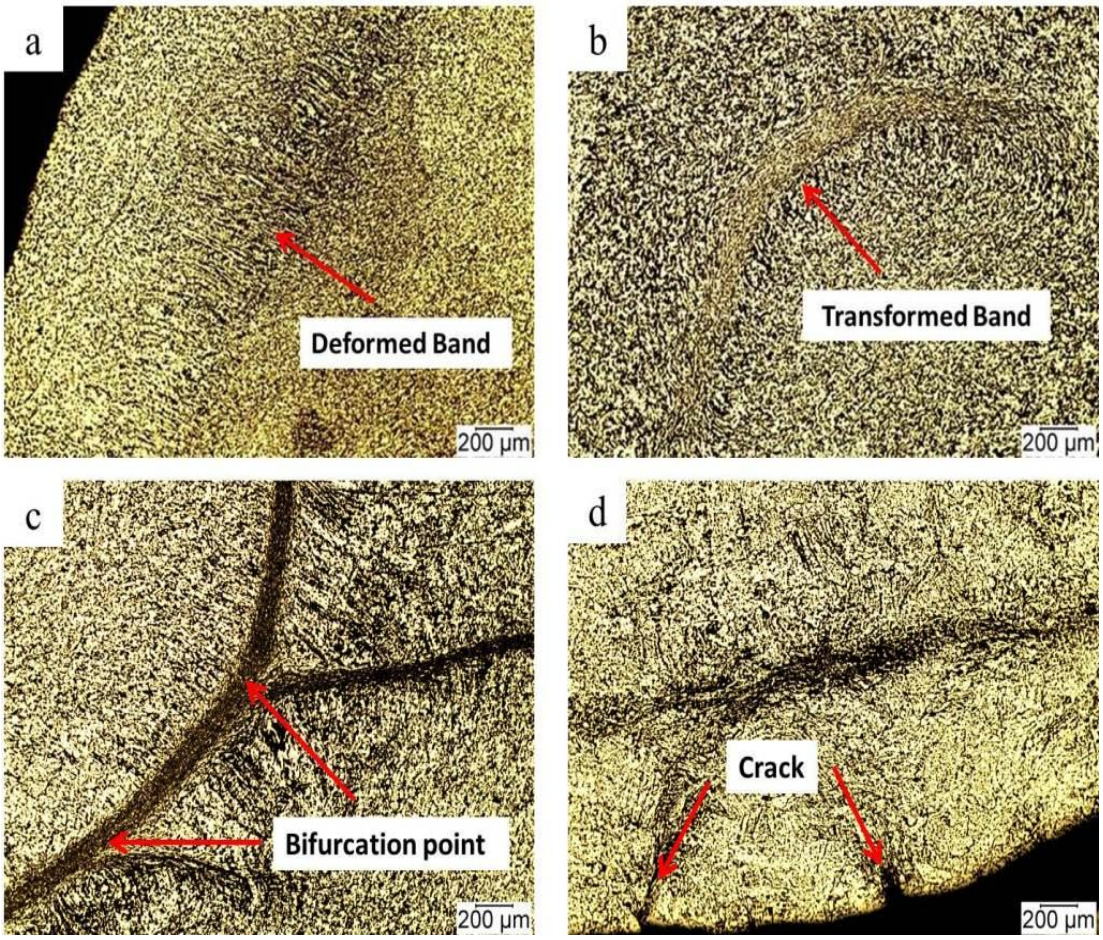

Figure 4.48. Optical micrographs of impacted AA6061-T6 alloy showing (a) deformed band at 33 kg m s^{-1}, (b) transformed band at 39 kg m s^{-1}, (c) shear band bifurcation at 44 kg m s^{-1}, and (d) crack propagating through transformed band at 44 kg m s^{-1}.

In AA6061-T8, a slightly deformed band (Fig 4.49a) was observed close to the sample's edge when impacted at 33 kg m s^{-1} momentum. At 39 kg m s^{-1}, the deformed band changed to transformed band (Fig 4.49b). At 44 kg m s^{-1}, transformed shear band at specimen centre bifurcated (Fig 4.49c) and crack propagated along the transformed band (Fig 4.49d). The results of the optical microscopic examination of the impacted AA6061 aluminum alloy specimens showed the formation of partially transformed band in T4, deformed band in T6 and slightly deformed band in T8 when impacted at 33 kg m s^{-1}, which is in agreement with the results obtained in the dynamic mechanical tests. This implies that the AA6061 alloy in T4 temper has the lowest deformation resistance while

T8 temper has the highest deformation resistance under dynamic impact loading at high strain rates.

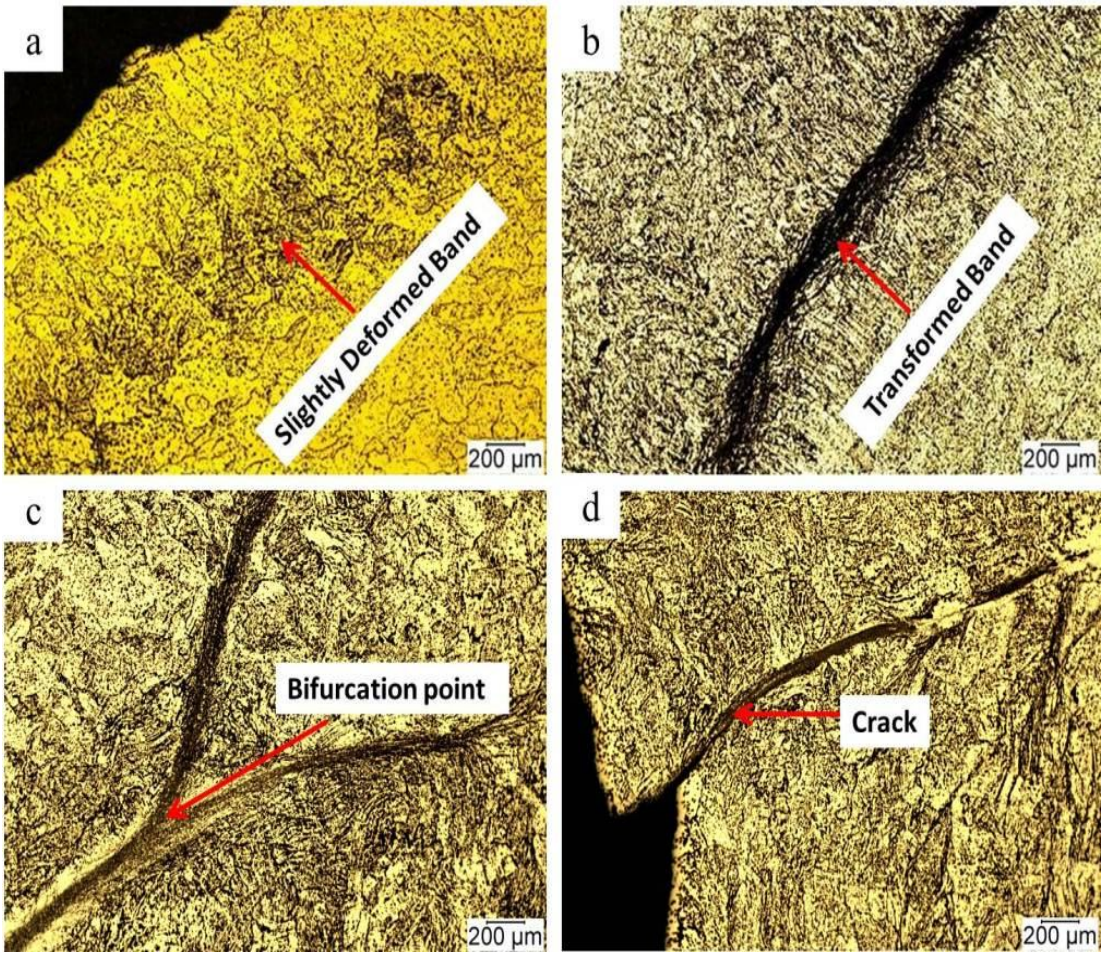

Figure 4.49. Optical micrographs of impacted AA6061-T8 alloy showing (a) slightly deformed band at 33 kg m s^{-1}, (b) transformed band at 39 kg m s^{-1}, (c) shear band bifurcation at 44 kg m s^{-1}, and (d) crack propagating through transformed band at 44 kg m s^{-1}.

4.3.2.4 AA6061 aluminum alloy (Scanning Electron Microscopy)

The results of the scanning electron microscopic investigations of the impacted AA6061 aluminum alloy specimens impacted at 44 kg m s^{-1} using secondary electron imaging technique are presented in Figures 4.50 to 4.52. The microstructures of the region inside and outside shear band were investigated. Secondary electron images show that the shear bands consist of fine submicron size grains of average size of 0.574 µm in T8 (Fig

4.50), 0.633 μm in T6 (Fig 4.51) and 0.654 μm in T4 (Fig 4.52) tempers. The microstructural morphology inside the shear bands is similar for the three temper conditions as presented in the secondary electron images for the alloys impacted at 44 kg m s^{-1}. It is evident from Figure 4.50 that secondary phase particles were squeezed into the centre of the shear band leaving behind a zone relatively free of particles or with low density of particles at the periphery of the shear band. Secondary electron images of transformed bands in impacted AA6061-T6 (Fig 4.51) and AA6061-T4 (Fig 4.52) did not reveal such a particle free zone on both sides of the transformed band observed in the T8 temper condition. The squeezing of particles in AA6061-T8 caused the secondary phase particles to become more closely packed. High intensity of localized deformation in AA6061-T4 caused formation of tree-shaped transformed bands in this material (Fig 4.52a). Microvoids leading to crack formation and propagation were observed in AA6061-T4 (Fig 4.52c). Due to the high temperature generated during adiabatic heating, the interface between particles became weak and particle debonding occurs thereby creating voids. The secondary electron images of regions outside shear band in the AA6061 aluminum show rectangular shape of the secondary phase particle in the T8 alloy (Fig 4.50c). Although, such rectangular shaped particles can be observed in the T6 alloy (Fig 4.51c), the precipitates have irregular shape in the T4 alloy (Fig 4.52d). The microstructure of regions outside shear band in T4, T6 and T8 look the same as those of the un-impacted specimens.

In order to understand the mechanism of formation of the submicron size grains observed inside the transformed bands of AA6061 in T4, T6 and T8 temper conditions, optical micrograph of the region ahead of transformed band was closely studied. Optical micrographs of AA6061-T4 (Fig 4.47c), AA6061-T6 (Fig 4.48c) and AA6061-T8 (Fig 4.49c) show elongation of grains ahead of the transformed band suggesting elongation and fragmentation of the second phase particles inside the transformed band [34]. Formation of these submicron grains can also be attributed to dynamic recovery [74,75] and dynamic recrystallization mechanisms [12,26,30,89-91]. However, the manner at which the transformed bands are preceded by elongated second phase particles aligning in the shear flow direction suggests fragmentation of the second phase

particles as the mechanism of formation of the fine subgrains inside the shear bands. Shear stress from the rigid walls of the shear bands is suggested to cause the elongation and fragmentation of second phase particles inside the shear bands.

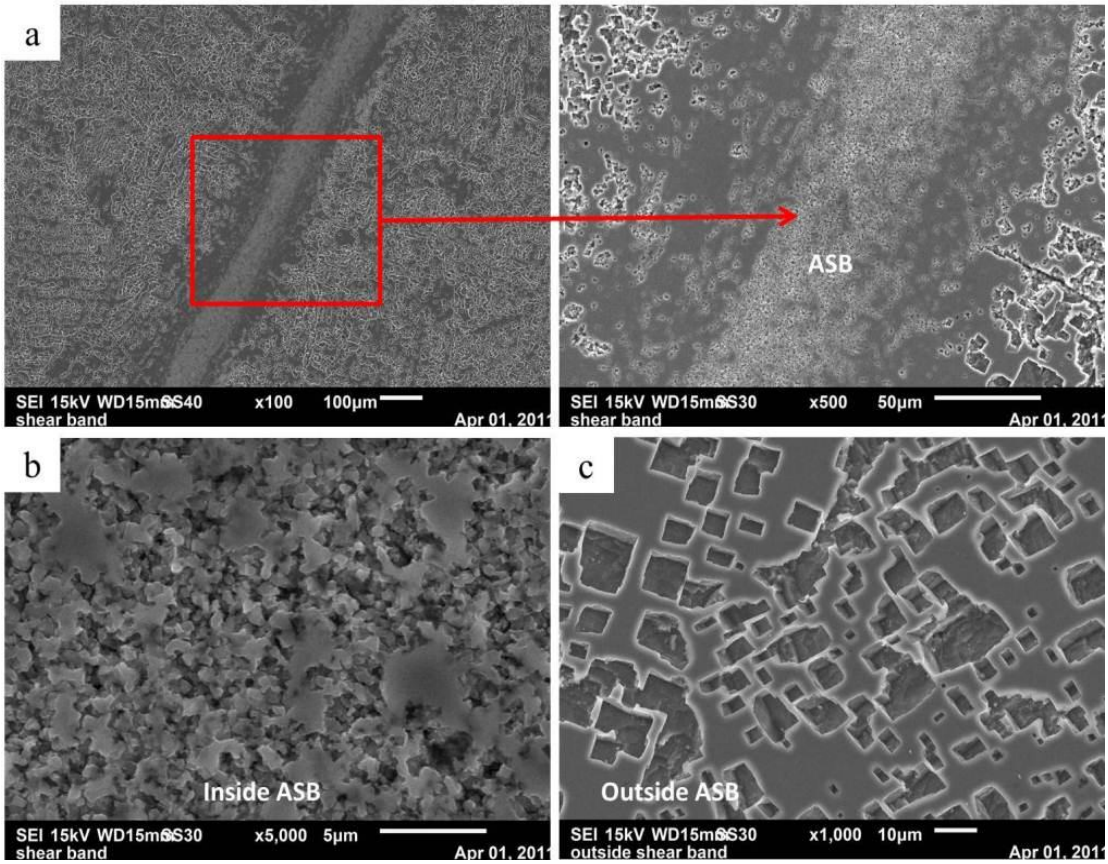

Figure 4.50. SEM micrographs showing the microstructure inside and outside transformed ASBs in AA 6061-T8 aluminum alloy impacted at 44 kg.m/s (a) overview, (b) inside ASB and (c) outside ASB.

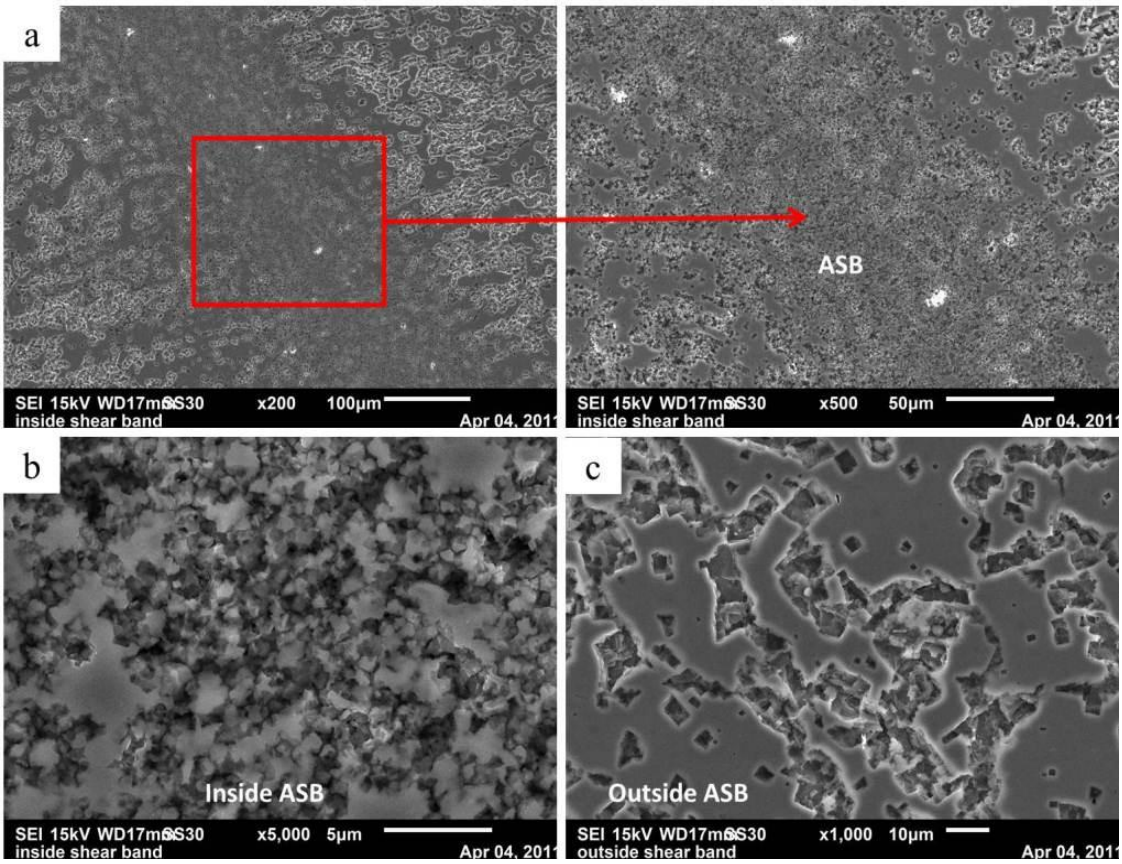

Figure 4.51. SEM micrographs showing the microstructure inside and outside transformed ASBs in AA 6061-T6 aluminum alloy impacted at 44 kg.m/s (a) overview, (b) inside ASB and (c) outside ASB.

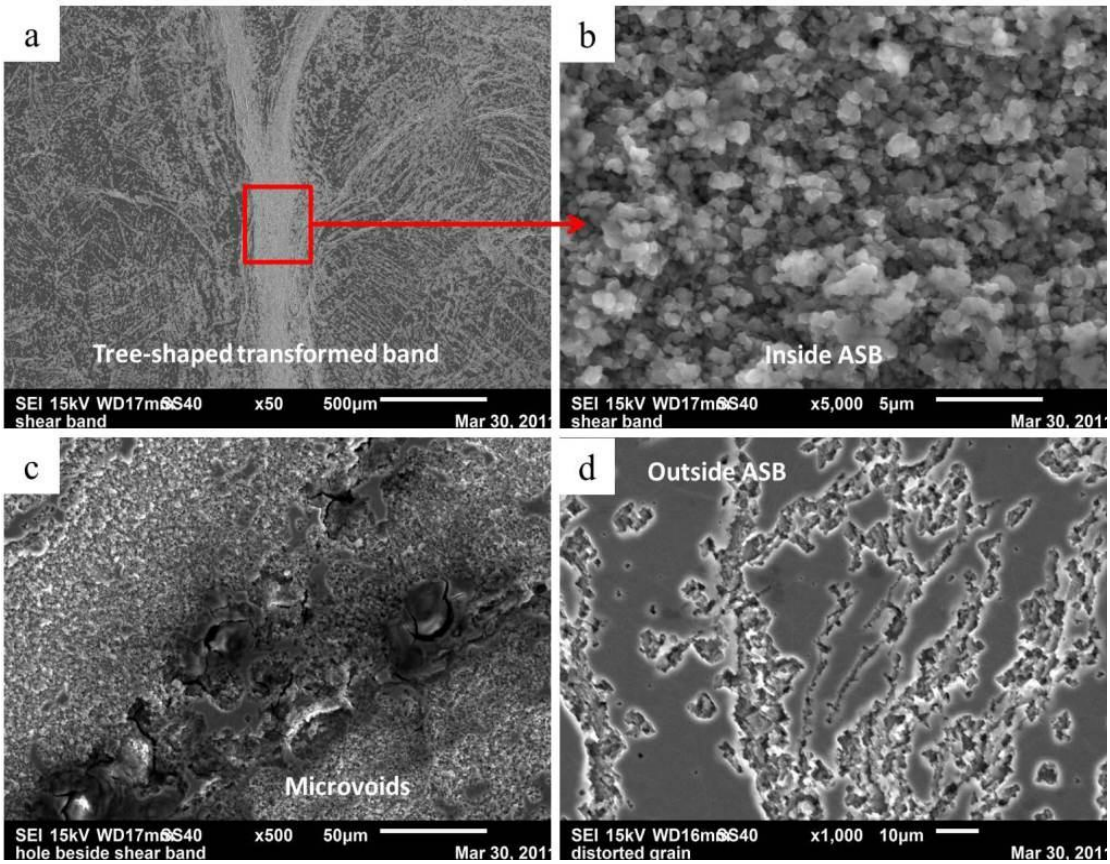

Figure 4.52. SEM micrographs showing the microstructure inside and outside transformed ASBs in AA 6061-T4 aluminum alloy impacted at 44 kg.m/s (a) overview, (b) inside ASB, (c) microvoids leading to crack formation inside ASB and (d) outside ASB.

4.3.2.5 AA6061 aluminum alloy (X-PEEM with NEXAFS Spectroscopy)

In order to further understand the phase changes associated with the intense adiabatic heating and formation of transformed bands in the AA6061 aluminum alloy, X-ray photoemission electron microscopy (X-PEEM) and near edge X-ray absorption fine structure (NEXAFS) spectroscopy was carried out on AA6061-T6 alloy sample that showed transformed bands. X-PEEM investigations were carried out at soft X-ray spectromicroscopy (SM) beamline of the Canadian Light Source in Saskatoon, Saskatchewan, Canada. The results of this study are presented in Figures 4.53-4.55. Figure 4.53a shows PEEM image of the shear band using 5.0 eV UV source. The image contrast is due to variation in the work function of the elements inside and outside the shear band. Brighter area indicates that more electrons are emitted and hence less work

function. Clear distinction between regions inside and outside the shear band were observed. Shear band region appear brighter indicating low work function compared to the outside shear band region (Fig 4.53). Figure 4.53b shows, Si 1s-2p mapping of the same area using tunable X-rays from synchrotron. The image contrast appeared reversed. The silicon mapping (white for silicon) of X-PEEM images produced from the synchrotron radiation indicates the presence of more silicon adjacent to the shear band region than inside the shear band.

Figures 4.54 and 4.55 show Al and Si K-edge NEXAFS spectra from the same area. No difference is observed in the Al K-edge spectra for both inside and outside shear band region as both spectra have the same intensity, however with a little shift (Fig 4.54). Peaking of aluminum at 1564 eV with energy change (ΔE) of +4 eV is found to be in agreement with previously achieved results on Al K-edge spectra in natural aluminum minerals [123-127]. The observed shift in peak is suggested to be due to problem with equipment alignment. The Si K-edge spectra show a higher intensity of silicon in the region outside the shear band than the region inside the shear band (Fig 4.55). The silicon peak observed in the silicon K-edge spectra at 1845 eV in the region outside the shear band agrees with previous results achieved in Si K–edge spectra [128-129]. It is believed that the combined effect of intense heating and strain coupled with the flow of the viscous materials inside the shear band caused some silicon-rich phase (Mg_2Si) to be squeezed out of the shear band. Due to equipment breakdown at the Canadian Light Source, the investigation of the shear band in AA2099 could not be carried out.

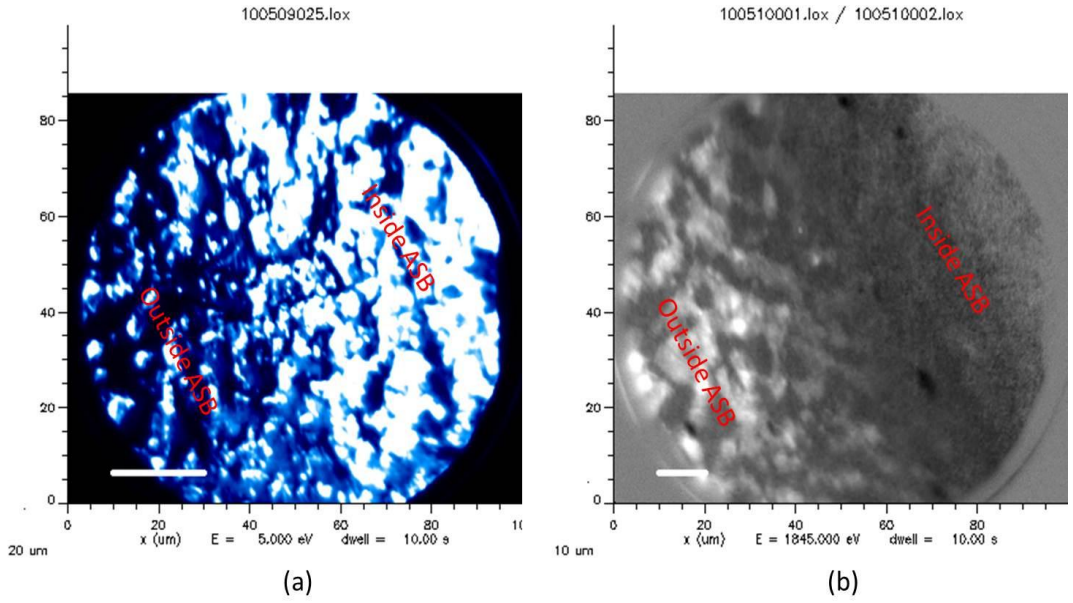

Figure 4.53. X-PEEM images of impacted AA6061-T6 alloy using (a) 5 eV mercury lamp and (b) silicon mapping using synchrotron radiation at 1845 eV.

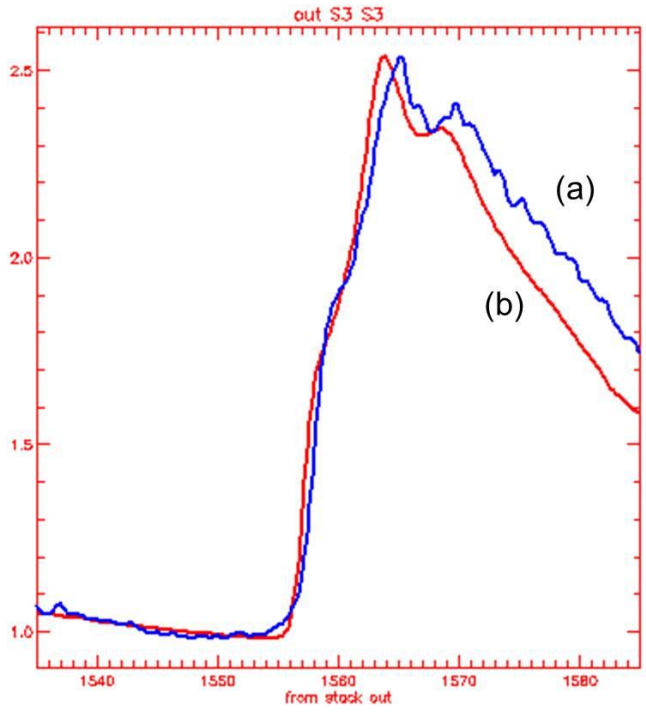

Figure 4.54. Al K-edge spectra (a) inside shear band and (b) outside shear band.

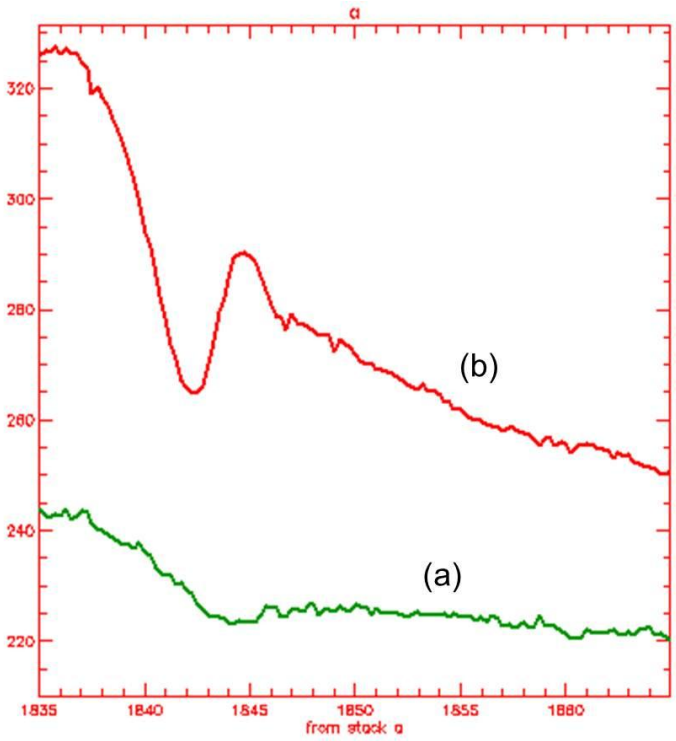

Figure 4.55. Si K-edge spectra (a) inside shear band and (b) outside shear band.

5. CONCLUSIONS AND RECOMMENDATIONS

This chapter itemizes the conclusions deduced from hardness test, quasi-static compression test, dynamic impact test, dynamic torsion test, optical microscopic examinations and scanning electron microscopic examinations of the investigated AA2099 and AA6061 aluminum alloys in T4, T6 and T8 temper conditions before and after impact loading.

5.1 Quasi-static tests (Hardness and compression tests)

1. Two-step aging treatment increases deformation resistance in AA2099 compared to the one-step aging treatment.
2. Strain hardening (cold work) prior to two-step aging treatment further increases the deformation resistance in AA2099 aluminum alloy.
3. Strain hardening prior to artificial aging had minimal effect on the hardness of AA6061 alloy but increased its deformation resistance under quasi-static loading.
4. AA2099 aluminum alloy possesses a higher deformation resistance compared to AA6061. This strength increase is attributed to the presence of more coherent or incoherent second phase particles in this alloy.

5.2 Dynamic mechanical tests (Direct impact and dynamic torsion tests)

1. Although AA2099 shows superior mechanical properties to AA6061 for all the temper conditions investigated under quasi-static loading, the reverse is observed to be the case under high strain rate loading. The AA6061 alloy showed more deformation resistance compared to AA2099 under dynamic mechanical loading at high strain rates.

2. The lower deformation resistance of AA2099 alloy at high strain rate is due to higher susceptibility to localized adiabatic heating and occurrence of adiabatic shear bands.
3. Strain hardening prior to aging treatment reduces the deformation resistance of AA2099 alloy under dynamic impact loading. The deformation resistance is also reduced in two-step aged AA2099 alloy compared to the one-step aged alloy.
4. The presence of several coherent or incoherent precipitated second phase particles increases the tendency of AA2099 to shear strain localization.
5. The naturally aged AA2099 alloy showed the highest deformation resistance under dynamic impact loading. It however showed the lowest deformation resistance under quasi-static loading.
6. Strain hardening (cold work) prior to age hardening in AA6061 increases the deformation resistance of the alloy under dynamic impact loading.

5.3 Optical and scanning electron microscopic investigations

1. Paths of extreme shear strain localization are observed in both AA2099 and AA6061 aluminum alloys under dynamic impact loading. Depending on the strain rate and temper condition of the alloys, deformed and/or transformed bands are formed.
2. The dissolution of second phase particles occurs within the transformed band of AA2099 alloy, which impairs its response under dynamic impact loading. It explains the ease at which peak flow stress drops during impact loading.
3. The formation of very faint transformed bands in non-cold worked AA2099 alloy compared to the wide transformed band observed in cold worked samples (T81, T82 and T8) accounts for the high deformation resistance observed in non-cold worked (T4, T61 and T62) AA2099 alloy samples under dynamic shock loading.
4. The shearing (T4 and T61), elongation and coalescence (T62) of various sized second phase particles instead of their dissolution results in higher deformation resistance for non-cold worked AA2099 alloy specimens (T4, T61 and T62).

5. No second phase particle dissolution was observed in AA6061. Instead, the second phase particles were fragmented within the transformed bands of AA6061. The transformed bands consist of equi-axed grains of size ranging between 0.574 – 0.654 μm depending on the temper condition.

5.4 X-PEEM with NEXAFS on transformed band in AA6061-T6 alloy

1. XPEEM elemental mapping shows the presence of equal intensities of Al in the regions inside and outside the transformed band.
2. XPEEM elemental mapping shows more silicon adjacent to the transformed band than inside the transformed band.

In summary, AA2099 aluminum alloy shows excellent mechanical behaviour under quasi-static loading conditions but its high susceptibility to intense adiabatic heating and occurrence of adiabatic shear bands impair its mechanical behaviour at high strain rates. Under dynamic shock loading, the AA2099 aluminum alloy shows superior deformation resistance in T4 temper condition compared to T6 and T8 tempers.

5.5 Recommendations for future works

1. Detailed study of the second phase particles observed in AA2099 using TEM should be carried out to ascertain their chemical composition and their roles in the behaviour of the alloy under dynamic loading conditions.
2. A systematic study of the effect of aging time on the mechanical behaviour of AA2099 and AA6061 alloys under dynamic loading conditions is suggested for future work.
3. There is need to perform a microhardness test across each shear band observed in both AA2099 and AA6061 alloys in order to obtain useful information on the mechanical properties of transformed bands that formed in these alloys.
4. It is recommended that X-PEEM and NEXAFS be used to determine compositional changes in the transformed band formed in AA2099 as influenced by the temper condition. This will shed more light on microstructural evolution in the transformed bands of AA2099 alloy.

6. REFERENCES

[1]. Alloy 2099-T83 and 2099-TE67 Extrusions, *ALCOA Aerospace Technical Fact Sheet*.

[2]. V. V. Zakharov, "Aluminum Alloys: Some Problems of the Use of Aluminum – Lithium Alloys", *Metal Science and Heat Treatment* 45 (1 – 2) (2003) 49 – 54.

[3]. S. Kalyanam, A.J. Beaudoin, R.H. Dodds Jr. and F. Barlat, "Delamination cracking in advanced aluminum–lithium alloys: Experimental and computational studies", *Engineering Fracture Mechanics* 76 (2009) 2174 – 2191.

[4] G.B. Burger, P.W. Jeffrey and D.J. Lloyd, "Microstructural control of aluminum sheet used in automotive applications", *Materials Characterization* 35 (1) (1995) 23 – 39.

[5] G.S. Cole and A.M. Sherman, "Lightweight materials for automotive applications", *Materials Characterization* 35 (1) (1995) 3 – 9.

[6] G. Lucas, "Aluminum structural applications", *Advance Materials and Processes* 149 (5) (1996) 29 – 30.

[7] B. Irving, "Interest in welded aluminum automobiles gathers momentum worldwide", *Welding Journal* 77 (6) (1998) 31 – 35.

[8]. H. Demir and S. Gündüz, "The effects of aging on machinability of 6061 aluminium alloy", *Materials and Design* 30 (2009) 1480 – 1483.

[9]. S. Nemat-Naser, "Introduction to High Strain Rate Testing, High Strain Rate Tension and Compression Tests" In ASM Handbook 8 (2000) 942 – 955.

[10]. M. Romios, R. Tiraschi, C. Parrish, H.W. Babel, J.R. Ogren, and O.S. Es-Said, "Design of Multistep Aging Treatments of 2099 (C458) Al-Li alloy", *Journal of Materials Engineering and Performance* 14 (2005) 641 – 646.

[11]. R.J. Rioja, E.L. Colvin, A.K Vasudevan and B.A. Cheney, "Aluminum alloy two-step aging method and article", United State Patent Number 4861391 (1989) 12 pages.

[12]. D. Rittel, S. Osovski, "Dynamic failure by adiabatic shear banding", I*nternational Journal of Fracture* 162 (2010) 177 – 185.

[13]. B. Zhang, W. Shen, Y. Liu and R. Zhang, "Adiabatic shear bands in impact wear", *Journal of Materials Science Letters* 17 (1998) 765 – 767.

[14] T. Bjerke and J. Lambros, "Heating during shearing and opening dominated dynamic fracture of polymers", *Experimental Mechanics* 42 (2002) 107 – 114.

[15]. C.G. Lee, Y. Lee and S. Lee, "Observation of adiabatic shear bands formed by ballistic impact in Aluminum-Lithium alloys", *Scripta Metallurgica et Materialia* 32 (6) (1995) 821 – 826.

[16]. F. Yadzani, M.N. Bassima and A.G. Odeshi, "The formation of adiabatic shear bands in copper during torsion at high strain-rates", *Procedia Engineering* 1 (2009) 225 – 228.

[17]. K.M. Roessig and J.J. Mason, "Adiabatic shear localization in the dynamic punch test, part I: experimental investigation", *International Journal of Plasticity* 15 (1999) 241 – 262.

[18]. D.R. Lesuer, C.K. Syn and O.D. Sherby, “Severe plastic deformation through adiabatic shear banding in Fe-C Steels”, *Materials Science and Engineering A* 410 – 411 (2005) 222 – 225.

[19]. A.G. Odeshi, M.N. Bassim and S. Al-Ameeri, “Effect of heat treatment on adiabatic shear bands in a high-strength low alloy steel”, *Materials Science and Engineering A* 419 (2006) 69 – 75.

[20]. B. Hwang, S. Lee, Y.C. Kim, N.J. Kim and D.H. Shin, “Microstructural development of adiabatic shear bands in ultrafine grained low carbon steels fabricated by equal channel angular pressing”, *Materials Science and Engineering A* 441 (2006) 308 – 320.

[21]. A. Marchand and J. Duffy, “An experimental study of the formation process of adiabatic shear bands in a structural steel”, *Journal of the Mechanics and Physics of Solids* 36 (3) (1988) 251 – 283.

[22]. C.G. Lee, W.J. Park, S. Lee and K.S. Shin, “Microstructural Development of adiabatic shear bands formed by ballistic impact in a Weldalite 049 alloy”, *Metallurgical and Materials Transaction A* 29 (1998) 447 – 483.

[23]. D.H. Li, Y. Yang, T. Xu, H.G. Zheng, Q.S. Zhu and Q.M. Zhang, “Observation of the microstructure in the adiabatic shear band of 7075 aluminum alloy”, *Materials Science and Engineering A* 527 (2010) 3529 – 3535.

[24]. Y.B. Xu, W.L. Zhong, Y.J. Chen, L.T. Shen, Q. Liu, Y.L. Bai and M.A. Meyers, “Shear localization and recrystallization in dynamic deformation of 8090 Al-Li alloy”, *Materials Science and Engineering A* 299 (2001) 287 – 295.

[25]. D. Rittel, “Adiabatic shear failure of a syntactic polymeric foam”, *Materials Letters* 59 (2005) 1845 – 1848.

[26]. M.A. Meyers, V. Nesterenko, J.C. LaSalvia and Q. Xue, "Shear localization in dynamic deformation of materials: microstructural evolution and self – organisation", *Materials Science and Engineering A* 317 (2001) 204 – 225.

[27]. G.M. Owolabi, A.G. Odeshi, M.N.K. Singh and M.N. Bassim, "Dynamic shear band formation in Aluminum 6061-T6 and Aluminum 6061 – T6/Al_2O_3 composites", *Materials Science and Engineering A* 457 (2007) 114 – 119.

[28]. G.H. Wu, D.Z. Zhu, G.Q Chen, L.T Jiang and Q. Zhang, "Adiabatic shear failure of high reinforcement content Aluminum matrix composites", *Journal of Materials Science* 43 (2008) 4483 – 4486.

[29]. L.H. Dai, L.F. Liu and Y.L. Bai, "Formation of adiabatic shear band in metal matrix composites", *International Journal of Solids and Structures* 41 (2004) 5979 – 5993.

[30]. J.A. Hines, K.S. Vecchio and S. Ahzi, "A Model for Microstructure Evolution in Adiabatic Shear Bands", *Metallurgical and Materials Transaction A* 29 (1998) 191 – 203.

[31]. Y. Xu, J. Zhang, Y. Bai and M.A. Meyers, "Shear localization in Dynamic deformation: Microstructural Evolution", *Metallurgical and Materials Transaction A* 39 (2008) 811 – 843.

[32]. M.N. Bassim and A.G. Odeshi, "Shear strain localisation and fracture in high strength structural materials", *Archives of Materials Science and Engineering* 31 (2) (2008) 69 – 74.

[33]. D. Rittel, P. Landau and A. Venkert, "Dynamic recrystallization as a potential cause for adiabatic shear failure", *Physical Review Letters* 101 (16) (2008) 165501 (1 – 4).

[34]. Z.H. Chen, L.C. Chan, T.C. Lee and C.Y. Tang, "An investigation on the formation and propagation of shear band in fine-blanking process", *Journal of Materials Processing Technology* 138 (2003) 610 – 614.

[35]. T. Kamijo, A. Fujiwara and H. Ingaki, "Shear band in high purity Al", *Scripta Metallurgica et Materialia* 25 (4) (1991) 949 – 954.

[36]. T.D. Rostova and V.V. Zakharov, "Nonferrous metals and alloys", *Metal Science and Heat treatment* 38 (5) (1997) 236 – 239.

[37]. C.G. Lee and S. Lee, "Correlation of dynamic torsional properties with adiabatic shear banding behaviour in ballistically impacted aluminum-lithium alloys", *Metallurgical and Materials Transaction A* 29 (1998) 227 – 235.

[38]. W.B. Lee and K.C. Chan, "A microplasticity analysis of shear band cracks in rolled 2024 aluminum alloy", *International Journal of Fracture* 52 (1991) 207 – 221.

[39]. M. Gasperini, C. Pinna and W. Swiatnicki, "Microstructure evolution and strain localization during shear deformation of aluminum alloy", *Acta Materialia* 44 (10) (1996) 4195 – 4208.

[40]. H. Inagaki and S. Kohara, "Shear bands in cold rolled Al-Mg alloy polycrystals", *Carl Hanser, Munchen Z. Metallkd* 88 (10) (1997) 570 – 575.

[41]. M.J. Hadiafard, R. Smerd, S. Winkler and M. Worswick, "Effect of strain rate on mechanical properties and failure mechanism of structural Al-Mg alloys", *Materials Science and Engineering A* 492 (2008) 283 – 292.

[42]. J. Kang, D.S. Wilkinson, M. Bruhis, M. Jain, P.D. Wu, J.D. Embury, R.K. Mishra and A.K. Sachdev, "Shear localization and damage in AA5754 aluminum alloy sheet", *Journal of Materials Science and Performance* 17 (3) (2008) 395 – 401.

[43]. J.M. Carlson and J.E. Bird, "Thermal and strain rate softening in Al-Mg sheet during necking and shear band formation", *Metallurgical and Materials Transaction A* 18 (1987) 1154 – 1156.

[44]. M.J. Hadianfard and M.J. Worswick, "Influence of strain rate on shear localization during deformation and fracture of 5754 and 5182 aluminum alloy", *Materials Science Forum* 519 – 521 (2006) 1047 – 1052.

[45]. A.O Adesola and A.G. Odeshi, "A comparative study of the compressive behaviour of 2099-T6 and 6061-T6 aluminum alloys under quasi-static and dynamic shock loading", In conference proceedings, Materials Science and Technology (MS&T) 2010, October 17-21, 2010, Houston, Texas, 2075 – 2084.

[46]. P.W. Leech, "Observation of adiabatic shear band formation in 7039 aluminum alloy", *Metallurgical Transactions A* 16 (1985) 1900 – 1903.

[47]. Y. Yang, Y. Zeng and Z.W. Gao, "Numerical and experimental studies of self-organization of shear bands in 7075 aluminum alloy", *Materials Science and Engineering A* 496 (2008) 291 – 302.

[48]. K. Cho, S. Lee, W.B. Choi and I. Park, "Formation of adiabatic shear band in Al-SiC_w metal matrix composite", *Advanced Materials* (1993) 1265 – 1269.

[49]. B.M. Love and R.C. Batra, "Effect of particulate/matrix debonding on the formation of adiabatic shear bands", *International Journal of Mechanics* 52 (2010) 386 – 397.

[50]. B.F. Wang, "Adiabatic shear band in a Ti-3Al-5Mo-4.5V Titanium alloy", *Journal of Materials Science* 43 (2008) 1576 – 1582.

[51]. M.T. Perez-Prado, J.A. Hines and K.S. Vecchio, "Microstructural evolution in adiabatic shear bands in Ta and Ta-W alloys", *Acta Materialia* 49 (2001) 2905 – 2917.

[52]. M.A. Meyers and C.L Wittman, "The effect of metallurgical parameters on shear band formation in low-carbon (~0.20 Pct) steels", *Metallurgical and Materials Transaction A* 21 (1990) 3153- 3164.

[53]. Z.H Chen, L.C. Chan, T.C. Lee and C.Y. Tang, "An investigation on the formation and propagation of shear band in fine-blanking process", *Journal of materials Processing Technology* 138 (2003) 610 – 614.

[54]. J.L. Derep, "Microstructure transformation induced by adiabatic shearing in armour steel", *Acta Metallurgica* 35 (6) (1987) 1245 – 1249.

[55]. A.J. Sunwoo, R. Becker, D.M. Goto, T.J. Orzechowski, H.K. Springer, C.K. Syn and J. Zhou, "adiabatic shear band formation in explosively driven AerMet-100 alloy cylinders", *UCRL-JRNL*-218875.

[56]. K. Cho, Y.C. Chi and J. Duffy, "Microscopic observations of adiabatic shear bands in three different steels", *Metallurgical and Materials Transaction A* 21 (5) (1990) 1161 – 1175.

[57]. J.H. Giovanola, "Adiabatic shear banding under pure shear loading part I: Direct observation of strain localization and energy dissipation measurements", *Mechanics of Materials* 7 (1988) 59 – 71.

[58]. A. Marchand and J. Duffy, "An experimental study of the formation process of adiabatic shear bands in a structural steel", *Journal of the Mechanics and Physics of Solids* 36 (1988) 251 – 283.

[59]. D. Rittel, "Dynamic shear failure of materials", In: *Dynamic Failure of Materials and Structures*, Arun Shukla, Guruswami Ravichandran, Yapa D.S. Rajapakse (Eds.), *Springer*, Boston, MA, 2010, pp. 29 – 61.

[60]. K.M. Roessig and J.J. Mason, "Adiabatic shear localization in the impact of Edge-notched specimens", *Experimental Mechanics* 38 (5) (1998) 196 – 202.

[61]. M. Zhou, A.J. Rosakis and G. Ravichandran, "Dynamically propagating shear bands in impact-loaded prenotched plates-I. Experimental investigations of temperature signatures and propagation speed", *Journal of Mechanics and Physics of Solids* 44 (6) (1996) 981 – 1006.

[62]. Y. Yang, X.M. Li, S.W. Chen, Q.M. Zhang, F. Jiang and H.G. Zheng, "Effects of pre-notches on the self-organization behaviours of shear bands in aluminum alloy", *Materials Science and Engineering A* 527 (2010) 5084 – 5091.

[63]. J.R. Li, J.L. Yu and Z.G. Wei, "Influence of specimen geometry on adiabatic shear instability of tungsten heavy alloys", *International Journal of Impact Engineering* 28 (2003) 303 – 314.

[64]. V.F. Nesterenko, M.A. Meyers and T.W. Wright, "Self-organization in the initiation of adiabatic shear bands", *Acta Materialia* 46 (1) (1998) 327 – 340.

[65]. D. Peirce, R.J. Asaro and A. Needleman, "Material rate dependent and localized deformation in crystalline solids", *Acta Metallurgica* 31 (12) (1983) 1951 – 1976.

[66]. L. Anand and S.R. Kalidindi, "The process of shear band formation in plain strain compression of FCC Metals: Effects of crystallographic texture", *Mechanics of Materials* 17 (1994) 223 – 243.

[67]. R.W. Armstrong and F.J. Zerilli, "Dislocation Mechanics Aspects of plastic instability and shear banding", *Mechanics of Materials* 17 (1994) 319 – 327.

[68]. B. Dodd and Yilong Bai, "Width of adiabatic shear bands formed under combined stresses", *Materials Science and Technology* 5 (6) (1989) 557 – 559.

[69]. R.C. Glenn and W.C. Leslie, "The nature of "white streaks" in impacted steel armor plate", *Metallurgical and Materials Transactions B* 2 (10) (1971) 2945 – 2947.

[70]. A.G. Odeshi, M.N. Bassim, S. Al-Ameeri and Q. Li, "Dynamic shear band propagation and failure in AISI 4340 steel", *Journal of Materials Processing Technology* 169 (2005) 150–155.

[71]. K.M. Cho, S. Lee, S.R. Nutt and J. Duffy, "Adiabatic shear band formations during dynamic torsional deformations of an HY-100 steel", *Acta Metallurgica et Materialia* 41 (1993) 923 – 932.

[72]. J. Duffy and Y.C. Chi, "The measurement of local strain and temperature during the formation of adiabatic shear bands", *Material Science and Engineering A* 257 (1992) 195 – 210.

[73]. Y.K. Chou and C.J. Evans, "White layers and thermal modeling of hard turned surfaces", *International Journal of Machine Tools and Manufacture* 39 (1999) 1863 – 1881.

[74]. H.J. McQueen, "Deficiencies in Continuous DRX Hypothesis as a Substitute for DRV Theory", *Materials Science Forum* 28 (2004) 351 – 356.

[75]. H.J. McQueen, E. Evangelista and N.D. Ryan, "Dynamic Recrystallization and Recovery: Mechanical and kinetic behavior; nucleation and growth mechanisms", In conference proceedings, International Conference on Recrystallization in Metallic Materials, T. Chandra, ed., TMS-AIME, Warrendale, PA, (1990) 89 – 100.

[76]. H.J. McQueen and E. Evangelista, "Mechanisms in creep and hot working to high strain, microstructural evidence, inconsistencies. Part I: substructure evolution; grain interactions", *Metallurgical Science and Technology* 28 (1) (2010) 12 – 21.

[77]. E. Nes, K. Marthinsen and Y. Brechet, "On the mechanisms of dynamic recovery", *Scripta Materialia* 47 (2002) 607 – 611.

[78]. L. Kubin, T. Hoc and B. Devincre, “Dynamic recovery and its orientation dependence in face-centered cubic crystals”, *Acta Materialia* 57 (2009) 2567 – 2575.

[79]. H.J. McQueen and W. Blum, “Dynamic recovery: sufficient mechanism in the hot deformation of Al (<99.99)”, *Materials Science and Engineering A* 290 (2000) 95 – 107.

[80]. B. Tian, C. Lind, E. Schafler and O. Paris, “Evolution of microstructures during dynamic recrystallization and dynamic recovery in hot deformed Nimonic 80a”, *Materials Science and Engineering A* 367 (2004) 198 – 204.

[81]. B. Derby, “The dependence of grain size on stress during dynamic recrystallization”, *Acta Metallurgica* 39 (5) (1991) 955 – 962.

[82]. J.E. Bailey and P.B. Hirsch, “The Recrystallization Process in Some Polycrystalline Metals”, “Proceedings of the Royal Society of London. Series A, Mathematical and Physical Sciences” 267 (1328) (1962) 11 – 30.

[83]. J.C.M. Li, “Possibility of subgrain rotation during recrystallization”, *Journal of Applied Physics* 33 (10) (1962) 2958 – 2965.

[84]. H. Hu, “In: Recovery and recrystallization of metals”, Vol. ed.: L. Himmel, John Wiley Interscience Publishing, New York (1963) 311 – 362.

[85]. R.D. Doherty, “The deformed state and nucleation of recrystallization”, *Metal Science* 8 (5) (1974) 132 – 142.

[86]. V.F. Nesterenko, M.A. Meyers, J.C. LaSalvia, M.P. Bondar, Y.J. Chen and Y.L. lukyanov, “Shear localization and recrystallization in high strain, high strain-rate deformation of tantalum”, *Materials Science and Engineering A* 229 (1997) 23 – 41.

[87]. M.A. Meyers and H. Pak, “Observation of an adiabatic shear band in titanium by high-voltage transmission electron microscopy”, *Acta Metallurgica* 34 (12) (1986) 2493 – 2499.

[88]. J.A. Hines and K.S. Vecchio, “Recrystallization kinetics within adiabatic shear bands”, *Acta materialia* 45 (2) (1997) 635 – 649.

[89]. D. Kuhlmann-Wilsdorf and J.H. Van Der Merwe, “Theory of dislocation cell sizes in deformed metals”, *Materials Science and Engineering* 55 (1) (1982) 79 – 83.

[90]. D. Kuhlmann-Wilsdorf and N.R. Comins, “Dislocation cell formation and work hardening in the unidirectional glide of f.c.c. metals I: Basic theoretical analysis of cell walls parallel to the primary glide plane in early stage II”, *Materials Science and Engineering* 60 (1) (1983) 7 – 24.

[91]. P.J. Jackson and D. Kuhlmann-Wilsdorf, “Low-energy dislocation cell structures produced by cross-slip”, *Scripta Metallurgica* 16 (1) (1982) 105 – 107.

[92]. C.L. Wittman, M.A. Meyers and H.R. Pak, “Observation of an adiabatic shear band in AISI 4340 steel by high voltage transmission electron microscopy”, *Metallurgical and Materials Transaction A* 21 (2) (1990) 707 – 716.

[93]. M.A. Meyers, “Dynamic failure: mechanical and microstructural aspects”, *Journal de Physique III* 6 (1994) C8-597-621.

[94]. S.P. Timothy and I.M. Hutchings, “Initiation and growth of microfractures along adiabatic shear bands in Ti-6Al-4V”, *Materials Science and Technology* 1 (1985) 526 – 530.

[95]. A.K. Zurek, “The study of adiabatic shear bands Instability in a pearlitic 4340 steel using a dynamic punch test”, *Metallurgical and Materials Transactions A* 25 (11) (1994) 2483 – 2489.

[96]. C.R. Brooks, “Heat treating of aluminum alloys, Principles of Heat Treating of Nonferrous Alloys” in ASM Metals Handbook 4 (1991) 1861 – 1960.

[97]. S. Matsuo, “Two-Step Ageing Behaviour in Al-Cu Base alloys”, *Transactions of National research institute for Metals* 17 (5) (1975) 34 – 46.

[98]. E.L. Tobolski and A. Fee, “Macroindentation Hardness Testing: Vickers Hardness Testing” In ASM Metal Handbook 08 (2000) 459 – 468.

[99]. R. Nakkalil, J.R. Hornaday Jr and M. Nabil Bassim, “Characterization of the compression properties of rail steels at high temperatures and strain-rates”, *Materials Science and Engineering A* 141 (1991) 247 – 260.

[100]. A. Gilat, “Torsional Kolsky Bar Testing” In ASM Metal Handbook 8 (2000) 1134 – 1162.

[101]. R. Ferragut, A Somoza and A Dupasquier, “On the two-step ageing of a commercial Al-Zn-Mg alloy; a study by positron spectroscopy”, *Journal of Physics: Condensed Matter* 8 (1996) 8945 – 8952.

[102]. R.S. James, “Aluminum-Lithium Alloys, Properties and Selection: Nonferrous Alloys and Special-Purpose Materials” In ASM Handbook 2 (1991) 667 – 672.

[103]. P. Sainfort and P. Guyot, “Fundamental aspects of hardening in Al-Li and Al-Li-Cu Alloys, Aluminum-Lithium Alloys III”, edited by C. Baker, P.J. Gregson, S.J. Harrison, and C.J. Peel, The Institute of Metals, London (1986) 420 – 426.

[104]. P. Sainfort, B. Dubost and P. Meyer, “Basic Hardening Mechanisms in Aluminum-Lithium Alloys”, MRS – Europe, November (1985) 45 – 54.

[105]. D. Venables, L. Christodoulou, and J.R. Pickens, “On the δ' --> δ transformation in Al-Li alloys”, *Scripta Metallurgica* 17 (10) (1983) 1263 – 1268.

[106]. R. McDonald, "Characterization of delamination in 2099-T861 Aluminum-Lithium", *PhD Thesis* (2009) pg 5.

[107]. A. Fendoni, "The effect of post weld heat treatment on the corrosion behaviour of AA2050T34-FSW", The University of Birmingham, School of Metallurgy and Materials, *MRes in Science and Engineering of Materials* October (2009) 1 – 119.

[108]. T.L. Giles, "The effect of friction stir processing on the microstructure and mechanical properties of AF/C458 Aluminum Lithium Alloy", Naval Postgraduate School, Monterey, California, USA *MSc Thesis* September (2005) 1 – 87.

[109]. N.I. Kolobnev, L.B. Khokhlatova and I.N. Fridlyander, "Aging of Al-Li Alloys Having Composite Particles of Hardening Phases", *Materials Forum* 28 (2004) 208 – 211.

[110]. J. Li, "Effect of microstructure and texture on high cycle fatigue properties of Al alloy", University of Kentucky, Lexington, Kentucky USA *PhD Thesis* (2007) 1 – 223.

[111]. L. Kovarik, S.A. Court, H.L. Fraser and M.J. Mills, "GPB zones and composite GPB/GPBII zones in Al-Cu-Mg alloys", *Acta Materialia* 56 (2008) 4808 – 4815.

[112]. C.D. Marioara, H. Nordmark, S.J. Andersen and R. Holmestad, "Post-β″ phases and their influence on microstructure and hardness in 6xxx Al-Mg-Si alloys", *Journal of Materials Science* 41 (2006) 471 – 478.

[113]. D.J. Chakrabarti and D.E. Laughlin, "Phase relations and precipitation in Al–Mg–Si alloys with Cu additions", *Progress in Materials Science* 49 (2004) 389 – 410.

[114]. J.J. Gracio, F. Barlat, E.F. Rauch, P.T. Jones, V.F. Neto and A.B. Lopes, "Artificial aging and shear deformation behaviour of 6022 aluminium alloy", *International Journal of Plasticity* 20 (2004) 427 – 445.

[115]. F. Ozturk, E. Esener, S. Toros and C.R. Picu, "Effects of aging parameters on formability of 6061-O alloy", *Materials and Design* 31 (2010) 4847 – 4852.

[116]. M.R. Rezaei, M.R. Toroghinejad and F. Ashrafizadeh, "Effects of ARB and ageing processes on mechanical properties and microstructure of 6061 aluminum alloy", *Journal of Materials Processing Technology* 211 (2011) 1184 – 1190.

[117]. F. Ozturk, A. Sisman, S. Toros, S. Kilic and R.C. Picu, "Influence of aging treatment on mechanical properties of 6061 aluminum alloy", *Materials and Design* 31 (2010) 972 – 975.

[118]. G.A. Edwards, K. Stiller, G.L. Dunlop and M.J. Coupers, "The Precipitation Sequence in Al-Mg-Si Alloys", *Acta materialia* 46 (11) (1998) 3893 – 3904.

[119]. C. Cayron and P.A. Buffat, "Transmission electron microscopy study of the β′ phase (Al–Mg–Si alloys) and QC phase (Al–Cu–Mg–Si alloys): ordering mechanism and crystallographic structure", *Acta Materialia* 48 (2000) 2639 – 2653.

[120]. M.A. Muñoz-Morris and D.G. Morris, "Severe plastic deformation processing of Al-Cu-Li alloys for enhancing strength while maintaining ductility", *Scripta Materialia* 63 (2010) 304 – 307.

[121] Y. Yang, Y. Zeng, D.H. Li and M. Li, "Damage and fracture mechanism of aluminum alloy Thick-walled cylinder under external explosive loading", *Materials Science and Engineering A* 490 (2008) 378 – 384.

[122] B.F. Wang, Y. Yang, Z.P. Chen and Y. Zeng, "Adiabatic shear bands in a-titanium tube under external explosive loading", *Journal of Materials Science* 42 (2007) 8101 – 8105.

[123]. C.S. Doyle, S.J. Traina, H. Ruppert, T. Kendelewicz, J.J. Rehr and G.E. Brown Jr., "XANES studies at the Al K-edge of aluminum-rich surface phases in the soil environment", *Journal of Synchrotron Radiation* 6 (1999) 621 – 623.

[124]. D. Li, M. Bancroft, M.E. Fleet, X.H. Feng and Y. Pan, "Al K –edge XANES spectra of aluminosilicate minerals", *American Mineralogist* 80 (1995) 432 – 440.

[125]. Y.F. Hu, R.K. Xu, J.J. Dynes, R.I.R. Blyth, G. Yu, L.M. Kozak and P.M. Huang, "Coordination nature of aluminum (oxy) hydroxides formed under the influence of tannic acid studied by X-ray absorption spectroscopy", *Geochimica et Cosmochimica Acta* 72 (2008) 1959 – 1969.

[126]. Ph. Ildefonse, D. Cabaret, Ph. Sainctavit. G. Calas, A.M. Flank and P. Lagarde, "Aluminum x-ray absorption Near Edge Structure in model compounds and Earth's surface minerals", *Physics and Chemistry of Minerals* 25 (1998) 112 – 121.

[127]. R.K. Xu, Y.F. Hu, J.J. Dynes, A.Z. Zhao, R.I.R. Blyth, L.M. Kozak and P.M. Huang, "Coordination nature of aluminum (oxy) hydroxides formed under the influence of low molecular weight organic acids and a soil humic acid studied by X-ray absorption spectroscopy", *Geochimica et Cosmochimica Acta* 74 (2010) 6422 – 6435.

[128]. D. Li, G.M. Bancroft, M. Kasrai, M.E. Fleet, R.A. Secco, X.H. Feng, K.H. Tan and B.X. Yang, "X-ray absorption spectroscopy of silicon dioxide (SiO_2) polymorphs: The structural characterization of opal", *American Mineralogist* 79 (1994) 622 – 632.

[129]. D.G.J. Sutherland, M. Kasrai, G.M. Bancroft, Z.F. Liu, and K.H. Tan, "Si L- and K-edge x-ray-absorption near-edge spectroscopy of gas-phase $Si(CH_3)_x(OCH_3)_{4-x}$: Models for solid-state analogs", *Physical Review B* 48 (20) (1993) 14989 – 15001.

VITA

Aderopo O. Adesola was born to Late Mr Ayinde Abiodun Adesola and Mrs Olujoke Takebo Adesola in Lagos State, Nigeria. He completed his elementary education at New State Pry School, Oshodi in 1993 and then proceeded to Oshodi High School, Oshodi in 1994 for his high school education. He completed his high school education in the year 2000. Between 2000 and 2002, he taught Mathematics and Chemistry at various tutorial centres in Lagos, imparting knowledge into youngsters. In year 2002, he started his undergraduate studies in the department of Metallurgical and Materials Engineering, University of Lagos. He completed his bachelor's degree with honours in 2007 and he was rated the best graduating student in the department. In 2008, he got a job as an aircraft maintenance engineer-in-training with KLM Engineering and Maintenance, a subsidiary of KLM Royal Dutch Airlines. During this period, he worked on aircraft, performing repairs and maintenance prior to take off and after landing. Aderopo has always had interest in studying failures of aerospace materials as well as the development of rockets and satellites. It was during his stay at KLM Engineering and Maintenance that he observed bird strikes on aircrafts. This initiated the foundation and zeal to study deformation and failure of aerospace materials. In 2009, he came to Canada and started his Master's degree programme in Mechanical Engineering at the University of Saskatchewan under the supervision of Dr Akindele Odeshi. He was awarded a new faculty graduate student support grant during his programme. He presented his research work at The Department of Mechanical Engineering graduate seminar presentations, University of Saskatchewan, Saskatoon, Canada on October 4, 2010, Materials Science and Technology 2010 Conference and Exhibition (MS&T'10) in Houston, USA on October 19, 2010 and also at the 23rd Canadian Materials Science Conference (CMSC 2011) in Kelowna, Canada on June 23rd 2011. He is the lead author of a conference paper and a co-author of another. He has a journal article currently under review for publication and he is also currently writing two journal articles to be sent for publication. In addition, Aderopo in 2010 gave his Life to Jesus Christ who is the author and finisher of his faith.